Title
Design Rules Governing Architecture–Transport Relationships in Microporous Materials

Author
Meckler, Stephen Matthew

Publication Date
2018

Peer reviewed|Thesis/dissertation

Design Rules Governing Architecture–Transport Relationships in Microporous Materials

By

Stephen Matthew Meckler

A dissertation submitted in partial satisfaction of the

requirements for the degree of

Doctor of Philosophy

in

Chemistry

in the

Graduate Division

of the

University of California, Berkeley

Committee in charge:

Doctor Brett A. Helms, co-chair
Professor Jeffrey R. Long, co-chair
Professor Ting Xu
Professor Jeffrey A. Reimer

Summer 2018

Design Rules Governing Architecture–Transport Relationships in Microporous Materials

Abstract

Design Rules Governing Architecture–Transport Relationships in Microporous Materials

by

Stephen Matthew Meckler

Doctor of Philosophy in Chemistry

University of California, Berkeley

Doctor Brett A. Helms, Co-Chair

Professor Jeffrey R. Long, Co-Chair

The rational design of microporous membrane materials enables exceptional control over the pore-network architecture, pore-wall chemistry, and structural rigidity that together dictate selective mass transport. These materials, which vary in structure from randomly packed microporous polymers to highly ordered porous crystals, discriminate between permeating species based on their size as well as their chemical and physical properties. Microporous membranes are not only a promising answer to the economic and environmental costs associated with industrial chemical separations but also a means to enhance the feasibility of incipient clean-energy technologies from carbon capture to electrochemical energy storage. In this dissertation, I discuss the chemical synthesis, membrane fabrication, and performance of state-of-the-art membrane materials to investigate the underlying structure-property relationships tying chemical design to selective mass transport.

In the first part of this dissertation, I describe my work advancing pure polymer membranes through the production of exceptionally rigid backbone chemistries. I present novel thermally rearranged polymer membranes that feature Tröger's base units as highly rigid sites of contortion along the polymer backbone. This rigidity enhances diffusive selectivity without sacrificing flux, challenging the permeability-selectivity tradeoffs inherent to polymer membranes. The Tröger's base thermally rearranged polymer membranes exhibit state-of-the-art performance for air separations.

In the second part of the dissertation, I discuss metal-organic framework (MOF)/polymer composites towards overcoming the permeability/selectivity tradeoffs inherent to pure polymers. First, I demonstrate an alternative synthesis of M_2(dobpdc), a family of phase-change adsorbent MOFs, that allows for control over the crystal size down to the nanoscale. Then I demonstrate that incorporating the amine-appended nano mmen-M_2(dobpdc) into a polymer membrane selectively increases the CO_2 permeability. Subsequently, I describe the growth of sub-micron MOF films at a porous polymer surface through the chemical conversion of sacrificial metal-oxide nanocrystals. Layered membranes can access the full potential of the molecular-sieving crystalline components without sacrificing the processability of the underlying polymer layer.

In the final part of this dissertation, I discuss my work characterizing polyelectrolyte binders for controlled ion transport in sulfur cathodes. In this system, unwanted mass transport of polysulfide components is hindered through strong attractive interactions with an ionically charged polymer binder. I ascertain the nature of those interactions through the use of synchrotron X-ray absorption spectroscopy which, when coupled with predictive molecular dynamics simulations, reveals that the polysulfides ring open to crosslink the binder chains.

To my parents, whose love and support opened the world for me

Table of Contents

Chapter 1: Introduction 1
1.1 Microporous Membranes 2
1.2 Microporous Materials with Controlled Pore Architectures and Pore Chemistries 3
1.2.1 Zeolites and Related Inorganic Molecular Sieves 3
1.2.2 Metal-Organic Frameworks 4
1.2.3 Carbon Nanotubes 4
1.2.4 Organic Nanotubes 5
1.2.5 Microporous Polymers 5
1.3 Design Principles for Microporous Materials 7
1.4 Size Selectivity and Chemical Selectivity 7
1.5 Transport Fundamentals 8
1.6 Modeling Transport through Microporous Materials 11
1.7 Polymeric Membranes for Gas Separations 15
1.7.1 Single-Component Membranes 15
1.7.2 Composite Membranes 16
1.8 Acknowledgements 20
1.9 References 20

Chapter 2: Thermally Rearranged Polymer Membranes Containing Tröger's Base Units Have Exceptional Performance for Air Separations 28
2.1 Introduction 29
2.2 Synthesis of Ortho-Acetate TB Polyimides 30
2.3 Controlling the Physical Properties of Ortho-Acetate Polyimides Through Backbone Chemistry 31
2.4 Characterizing the Thermal Rearrangement to TR-TB Polymer Membranes 32
2.5 The Effects of Thermal Rearrangement on Selective Gas Transport 33
2.6 Characterization of TR-TB Pore Architecture 34
2.7 Conclusions 36
2.8 Experimental Details 36
2.8.1 Materials 36
2.8.2 Characterization Methods 37
2.8.3 Synthetic Procedures 38
2.9 Acknowledgements 42
2.10 References 43

Chapter 3: Applying Diamine-Appended M_2(dobpdc) as a Next-Generation Gas Separation Membrane Material: Ultrafast Synthesis and Mixed-Matrix Membrane Fabrication 45
3.1 Introduction 46
3.2 Metal Oxides as Reactants in M_2(dobpdc) Synthesis 47
3.3 Crystallinity and Porosimetry as Quality Metrics 48
3.4 Assessment of the Reaction Trajectory from MO Dissolution to M_2(dobpdc) Crystallization 50
3.5 MO Etching Kinetics 54

3.6 Ultrafast Synthesis of M_2(dobpdc) from MO Colloidal Nanocrystal Precursors 56
3.7 Mg_2(dobpdc) Nanocrystal Synthesis from MO Precursors 58
3.8 Accessing Phase-Change Sorption Behavior in Mg_2(dobpdc) Nanocrystals 60
3.9 MMMs Incorporating Phase-Change Fillers 61
3.10 Analysis of Gas Transport Properties 62
3.11 Conclusion 63
3.12 Methods 64
3.12.1 Materials 64
3.12.2 Methods 64
3.12.3 Synthesis 65
3.12.4 Supplemental Figures 68
3.13 Acknowledgements 70
3.14 References 70

Chapter 4: Sub-Micron Polymer-Zeolitic Imidazolate Framework Layered Hybrids via Controlled Chemical Transformation of Naked ZnO Nanocrystal Films **72**
4.1 Introduction 73
4.2 ZIF-PIM Composite Formation 74
4.3 Structural Characterization of Composites 75
4.4 Quantification of Residual ZnO Through X-Ray Absorption Spectroscopy 78
4.5 Insights into the Metal Oxide-to-MOF Chemical Transformation Mechanism 79
4.6 Conclusions 81
4.7 Experimental Details 82
4.7.1 Materials 82
4.7.2 Synthesis and Sample Preparation 82
4.7.3 Characterization Methods 83
4.8 Acknowledgements 84
4.9 References 84

Chapter 5: Molecular Understanding of Polyelectrolyte Binders that Actively Regulate Ion Transport in Sulfur Cathodes **87**
5.1 Introduction 88
5.2 Designing Polyelectrolyte Binders to Regulate Polysulfide Transport 90
5.3 Understanding Anion Metathesis in Polyelectrolyte Binders 90
5.4 Modeling and Characterizing PEB-1/Polysulfide Binding Modes 91
5.5 Li–S Cell Performance Gains When Active PEB-1 Binders are in Place 94
5.6 Conclusion 95
5.7 Experimental Details 96
5.7.1 Materials 96
5.7.2 Synthesis and Sample Preparation 96
5.7.3 Characterization 99
5.8 Acknowledgements 100
5.9 References 100

Chapter 6: Conclusion..... 103

Acknowledgments

I would like to thank my research advisor, Dr. Brett Helms, for his mentorship over the years and for showing me how to think critically as a scientist. I would also like to thank Prof. Jeff Long for serving as my academic advisor and providing guidance during key moments of my Ph.D. The Center for Gas Separations Relevant to Clean-Energy Technologies (CGS) Energy Frontier Research Center, which provided me funding throughout my graduate degree, also connected me to a valuable network of brilliant and inspiring scientists, and for that I am grateful. I also thank all the members of my dissertation and qualifying exam committees, including Dr. Brett Helms, Prof. Jeffrey Long, Prof. Jeffrey Reimer, Prof. Ting Xu, Prof. Charles Harris, and Prof. Berend Smit.

The many members of the Helms Group with whom I have had the pleasure of working were a critical part of my time here at UC Berkeley and the Lawrence Berkeley National Laboratory, and I would like to thank them all here. I would like to especially thank Dr. Andrew Wills, Dr. Sean Doris, Dr. Lorenzo Maserati, Dr. Teresa Williams, Dr. Peter Christensen, Dr. Peter Frischmann, Dr. Swagat Sahu, Dr. Wenqian Feng, Dr. Chengyin Fu, Changfei He, Miranda Baran, Dr. Karol Miszta, Dr. Longjun Li, Dr. Ashleigh Ward, Dr. Laura Gerber, Dr. Changyi Li, Dr. Lin Ma, Benjamin Robertson, Lindsey Bear, Mark Carrington, and Dr. Miles Braten for their support, camaraderie, and guidance over the years. The Molecular Foundry community was another invaluable resource in the writing of my dissertation, and in addition to those listed above I would like to thank Teresa Chen, Liana Klivansky, Dr. David Britt, and Dr. Virginia Altoe for all their help.

I owe so much gratitude to my family and the many friends who have been there to support and encourage me during my time in Berkeley. First and foremost, my family: my mom, my dad, Lauren and Jessica have always been there for me, and can never thank them enough. Thank you to everyone who joined me on my many backcountry adventures these past few years, especially Dr. Dan Slotcavage for reminding me to take the time to go outside (and stay in shape). Thank you to the Sunday night game crew for all the great memories. And thank you to everyone else who has shared their love and support through this journey, especially Lauren Gleason. This dissertation would not have been possible without you.

Chapter 1

Introduction

1.1 Microporous Membranes

Improving the efficiency of membrane-based separations is critical to the advancement of many clean-energy technologies, including gas and chemical separations, carbon capture and sequestration (CCS), and electrochemical energy storage (EES). Schemes to engineer highly selective species transport across microporous membranes have progressed considerably in the past decade due to the advent of microporous membrane components with controlled pore architectures and pore chemistries (Figure 1.1). In contrast to conventional absorptive or adsorptive strategies requiring energy-intensive regeneration procedures, microporous membranes can achieve high fluxes of the desired permeant at markedly lower energetic costs, e.g., to improve gas and chemical separations;[1] they can often be implemented in a continuous process, consisting of a low-cost, integrated unit with a smaller footprint than the incumbent technology. In this chapter, I provide a critical assessment of how the pore architecture and pore chemistry of microporous materials dictate analyte selectivity or specificity.

Microporous membrane components considered here feature persistent free-volume elements (i.e., pores) less than 2 nm in diameter, which discriminate between analytes based on size and chemistry. Microporous membranes can either be single component or composites of several materials, of which at least one is microporous. The rigidity of their architectures influences, and sometimes enforces, size selectivity; thus, low framework mobility is often required. In these instances, the coupled motion of the microporous host material does not directly mediate the transport of guest analytes. As a result, transport selectivity and flux can be decoupled from the intra- and intermolecular mechanical flexibility of the microporous materials, thereby allowing for independent optimization of membrane performance attributes.

The primary classes of microporous materials are (1) inorganics (e.g., zeolites);[2] (2) hybrids (e.g., metal-organic frameworks, MOFs);[3] (3) carbons (e.g., carbon nanotubes[4] and carbon molecular sieves, CMSs);[5] and (4) organics (e.g., microporous polymers[6,7] and organic nanotubes).[8] While significant attention has been paid to the adsorptive[9] and catalytic[10-12] properties of high surface area microporous materials, here I discuss how their unique architectures impact transport selectivity for gases. Furthermore, I will address how transport outcomes are affected by both nanoconfinement within free-volume elements and pore–analyte interactions. The emerging perspective is that the unique shape-persistent architectures of these materials permit molecular diffusive permeabilities that are orders of magnitude faster than molecular diffusion in liquids or dense materials, and in rare cases, even faster than bulk kinetics while restricting the passage of other components of the analyte mixture.

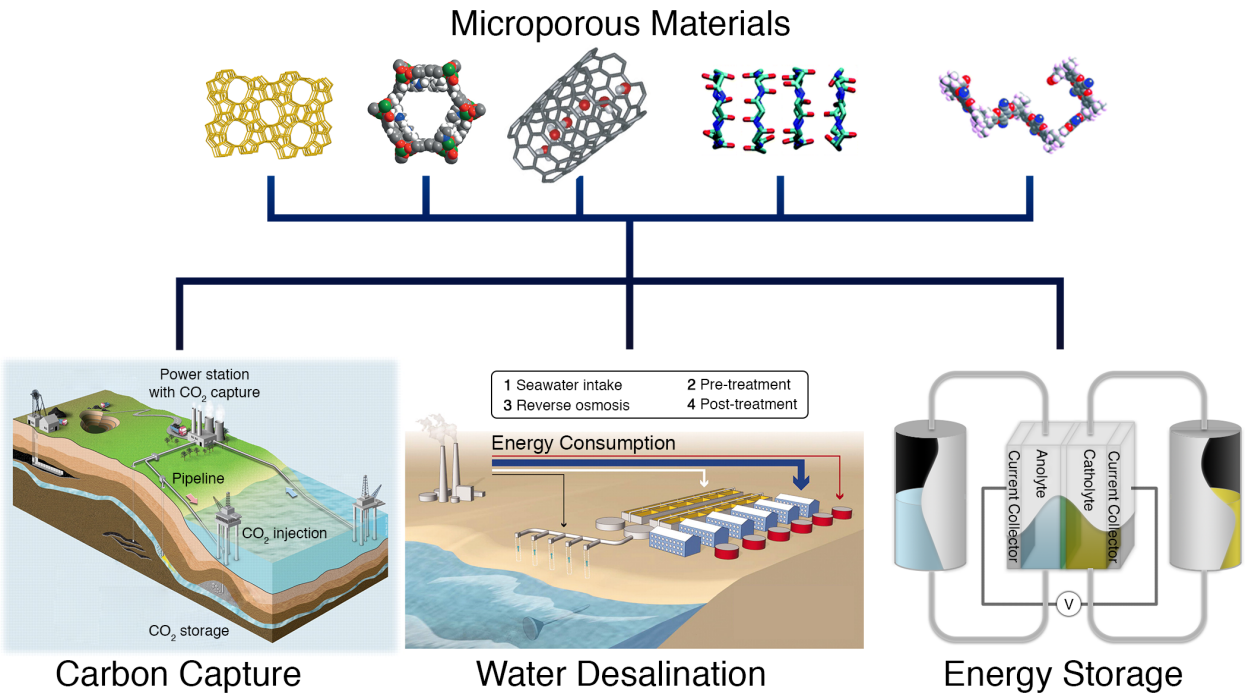

Figure 1.1 Microporous materials are leading a step change in clean-energy technologies ranging from carbon capture and water desalination to electrochemical energy storage. Microporous membrane components span zeolites, MOFs, carbon nanotubes, organic nanotubes, and intrinsically microporous polymers. The carbon capture image: Reproduced with permission.[13] Copyright 2009, AAAS. Water desalination image: Reproduced with permission.[14] Copyright 2011, AAAS. MOF image: Reproduced with permission.[15] Copyright 2015, Nature Publishing Group. Carbon nanotube image: Reproduced with permission.[16] Copyright 2001, Nature Publishing Group. Organic nanotube image: Reproduced with permission.[17] Copyright 2014, The Royal Society of Chemistry. Microporous polymer image: Reproduced with permission.[18] Copyright 2010, The Royal Society of Chemistry.

1.2 Microporous Materials with Controlled Pore Architectures and Pore Chemistries

1.2.1 Zeolites and Related Inorganic Molecular Sieves

Zeolites are microporous aluminosilicate framework solids[19] that exhibit well-ordered and periodic arrangements of matter and empty space (Figure 1.2). Related inorganic molecular sieves include silicalites,[20] metallosilicates,[21] and metallophosphates.[22] Though discovered in the 1700s,[23] zeolites did not find widespread industrial use for nearly two centuries.[24,25] Indeed, the molecular-sieving effect was not recognized in zeolites until 1925.[26] Today, hundreds of zeolites are available with uniform pore sizes ranging from 3 Å to more than 1 nm. Strict size and shape selectivity[27] have not only made them attractive molecular sieves for selective transport but also led to their broad adoption as adsorbates[28] and heterogeneous catalysts, particularly the so-called "Big Five" (FAU, MFI, MOR, BEA, and FER types).[12,29] Typical zeolite syntheses are carried out under hydrothermal conditions using silicates and aluminates. Variations of temperature, cations, reaction time, and pH, among other parameters, dictate framework outcomes.[25] Typically, the chemical makeup determines the structure of the zeolites. Occasionally, minor pore size adjustments are possible. For instance, zeolites 3A, 4A and 5A are all derived from zeolite A and incorporate different guest counterions: K^+, Na^+, and Ca^+, respectively.[30] Their incorporation into a membrane could take the form of a solid dispersion or

in situ synthesis on a membrane by way of seeded growth.[31] Recently, membrane design using zeolite nanosheets (ns) and inorganic nanotubes has also been investigated.[32]

1.2.2 Metal-Organic Frameworks

MOFs[33] are hybrid microporous materials composed of organic linkers joined together at inorganic nodes to form an extended 3D network (Figure 1.2). These crystalline materials are made up of two types of building blocks or secondary building units (SBUs)—metal-containing SBUs and organic SBUs. The metal-containing SBUs, which could be a metal ion or a cluster, act as nodes that are connected by polytopic organic linkers. In addition to forming architectural topologies that can be isomorphic to zeolites at an expanded scale (as is the case with zeolitic imidazolate frameworks or ZIFs),[34] organic linkers can be designed to yield MOFs of more exotic topologies or nets.[35]

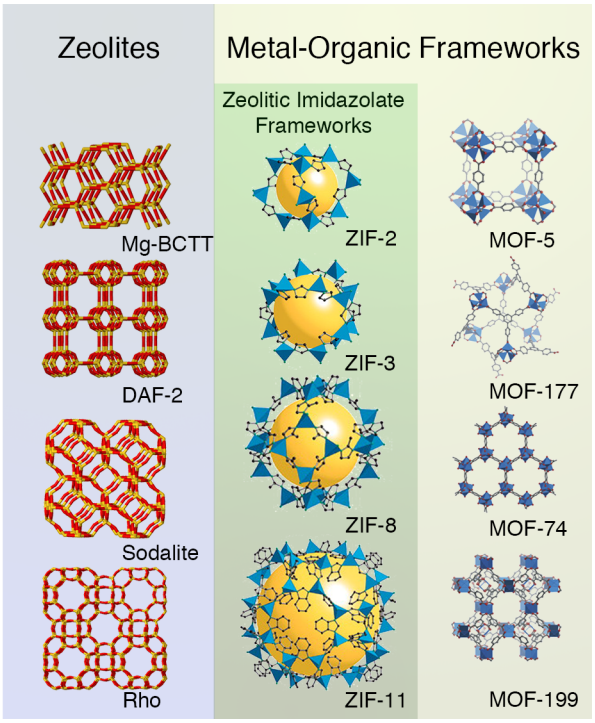

Figure 1.2 Structural diversity is a hallmark of both zeolites and MOFs, as demonstrated by the various structures and topologies presented here. ZIFs and their isomorphic counterpart zeolites are listed together for comparison. Zeolite structures: Generated using the Database of Zeolite Structures.[19c] MOF structures: Reproduced with permission.[45] Copyright 2008, Elsevier. ZIF structures: Reproduced with permission.[34] Copyright 2006, National Academy of Sciences.

Like zeolites, MOFs feature periodic arrangements of micropores, or in some instances mesopores, depending on the organic linker. They are also amenable to postsynthetic modifications to fine-tune interactions with analytes.[36] The diversity of architectures in this class of microporous materials is remarkable, with examples pushing the bounds of specific surface area (up to 7000 $m^2 g^{-1}$)[37] and porosity (up to 90%).[38] MOFs can adsorb and facilitate reactions for molecules that are too bulky for zeolites and other inorganic molecular sieves, and SBUs can be engineered synergistically to mediate analyte–pore-wall interactions.[39,40] These properties have been exploited for gas storage/adsorption,[41] catalysis,[10] sensing,[42] and other types of selective transport.[43,44]

Replacing the metal centers in MOFs with polytopic organic moieties yields covalent organic frameworks (COFs), e.g., as pioneered by Yaghi and co-workers.[46] COFs have attracted much attention but, although a small number of COF membranes have been reported,[47] they have yet to be used extensively in selective transport. Nonetheless, COFs have found early successes in gas storage[48] and electronic charge storage.[49] Interested readers are directed to a relevant review on these topics.[50]

1.2.3 Carbon Nanotubes

Carbon nanotubes are a mainstay of nanoscience and nanotechnology.[51] They exhibit unique electrical,[52] thermal, and mechanical[53] properties, and are also molecular-sieving materials in their own right. Catalysts, precursors, and process conditions can be tuned to control

nanotube diameters, either as single-walled or multiwalled nanostructures.[54] While a variety of routes have been reported to modify carbon nanotubes on the exterior or the openings,[55] there are as yet no strategies to functionalize their interior space. Instead, they remain a continuous and atomically smooth hydrophobic surface that is capable of promoting faster-than-bulk, frictionless kinetics via specular reflection of analyte molecules.[56] In addition to having a confined geometry for molecular sieving, carbon nanotubes also have shown promise in chemically distinguishing between analytes, ranging from ions[57] to macromolecules.[58] Microporous graphene is a promising 2D membrane material with greater opportunities for pore-wall functionalization.[59]

Whereas carbon nanotubes and porous graphene are exemplars of 1D and 2D microporous carbon nanostructures, respectively, CMSs are 3D. By pyrolizing a polymer precursor, microporous carbonaceous architectures emerge with high surface area, small pores (<1 nm), and narrow pore-size distributions.[60,61] Most CMSs are derived from polyimides,[62] such as Matrimid[63,64] or Kapton.[60,63,65] Other polymer precursors have included poly(furfuryl alcohol),[66] phenol-based resins,[67] and poly(vinyl chloride) copolymers.[68] Both precursor chain packing and pyrolizing procedure influence the final micropore architecture.[69] Unlike zeolites or MOFs, however, these shape-persistent microporous materials are random arrangements of matter and empty space. Through the stochastic stacking, the microvoids enable molecular sieving in membranes tailored for gas separations.[5,70,71]

1.2.4 Organic Nanotubes

Organic nanotubes are, like carbon nanotubes, prototypical microporous 1D nanostructures. Unlike carbon nanotubes, however, they are assembled from molecular components—either from wedge-like molecules (e.g., dendrimers,[72] guanosine quartets, or their related analogues,[73] etc.) or from discrete macrocycles (e.g., carbon nanohoops,[74] arylene ethynylenes,[75] or cyclic peptides)[76]—via noncovalent interactions, such as π–π stacking or hydrogen bonding. The structural diversity of organic nanotubes is vast. The size of their aperture can range from ~Å to ~nm, which is subject to precise synthetic control; the length of organic nanotubes, on the other hand, strongly depends on the strength of the noncovalent interactions and the assembly strategy. Uniquely, both their exteriors and interiors[77,78] can be modified with chemical functionality to enhance transport selectivity. Not surprisingly then, advances in synthetic methods have thus far focused on understanding these molecular structure–transport–selectivity relationships, rather than on practical aspects associated with scale-up, as might be required for membrane-based separations. In some instances, organic nanotubes benefit from exterior functionalization to align the nanotubes within a matrix (e.g., a mesostructured block copolymer film), allowing for facile membrane casting from solution.[79] Given their ability to regulate transport, organic nanotubes have been explored as transmembrane protein analogs.[80] Aside from bioinspired membrane applications, they have also been used as sensors.[81]

1.2.5 Microporous Polymers

In organic polymers, micropores naturally arise from imperfect packing of highly rigid and amorphous macromolecular structures. Whereas conventional polymers have dynamic microporosity due to thermally activated segmental chain motion (a physical characteristic more aptly defined as free volume), in recent years, researchers have engineered void-forming elements at the molecular level. In these cases, segmental chain dynamics have been significantly reduced, thereby resulting in materials that would be defined more classically as

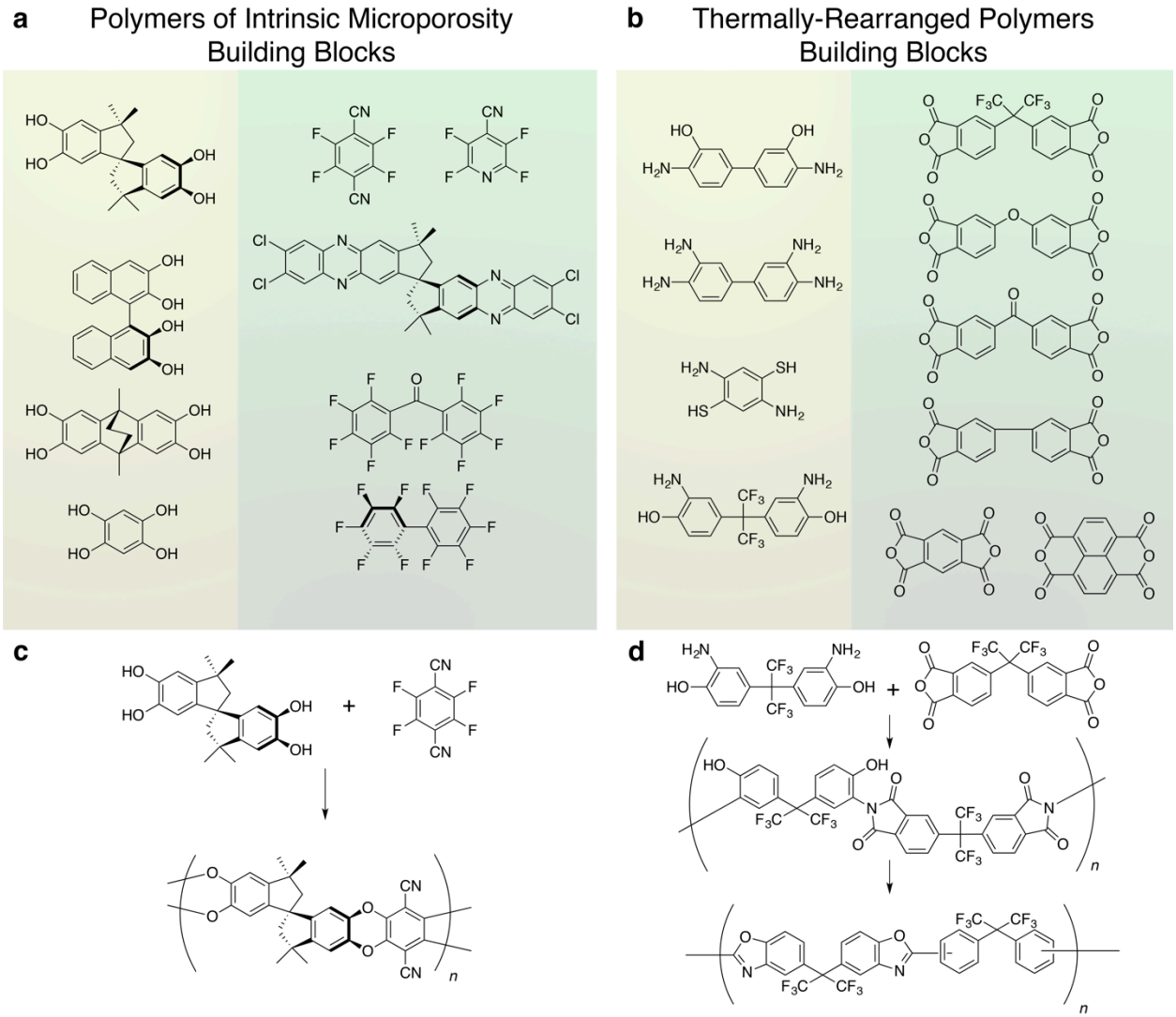

Figure 1.3 a) Monomer selection for PIMs. b) Monomer selection for TR polymers. c) PIM synthesis via step-growth polymerization. d) TR polymer synthesis via step-growth polymerization and subsequent thermal rearrangement.

microporous (Figure 1.3). For microporous organic polymers such as poly(1-trimethylsilyl-1-propyne) (PTMSP), 34% fractional free volume (FFV)[82] has been reported. PTMSP features a bulky trimethylsilane group on the backbone while maintaining a rigid sp^2-hybridized carbon main chain. Likewise, polymers of intrinsic microporosity (PIMs) achieve high FFV by introducing kinks into an otherwise rigid polymer backbone, which results in frustrated chain packing in the solid state.[83] For PIM-1, FFV approaches 20% and consists primarily of micropores.[84] Conjugated microporous polymers generate porosity via a similar principle of maintaining rigidity to disrupt packing. For polymers that are considered dense, there are generally two ways to introduce porosity chemically—reductive or additive. The reductive strategy is more prevalent and yields pores through triggered condensation of chemical moieties appended to the polymer. Thermally rearranged (TR) polymers[85] derive their microporosity in this manner, often times in a two-step process: first, monomers are polymerized into a processable precursor material; second, a thermal treatment is applied, which activates contracting rearrangement or partial decomposition of the precursor, revealing the micropores.

CMSs can be considered as an extreme of this case; one key difference, however, is that TR polymers can be formed without undergoing pyrolysis. The additive path, on the other hand, creates voids by chemically wedging spacers between polymer chains, often accomplished by crosslinking[86] (e.g., hyper-crosslinked polymers). In general, these polymers are processable in their non-crosslinked forms as large-area, flexible films. They often serve as a highly permeable matrix for composites incorporating other molecular-sieving components. The ease of processing and low cost of these microporous polymers have led to their adoption across many technology areas, including gas separation,[83,85,87] desalination,[88] and energy storage.[84]

1.3 Design Principles for Microporous Materials

Some general descriptions are useful in understanding transport across microporous membranes used in various applications. First, analyte molecules in the feed contact the membrane. The analyte then enters the membrane, either dissolving into the membrane bulk or occupying pore free volume. Then, the analyte diffuses across the membrane driven by a chemical potential gradient. Flux is determined by the ability of the analyte to fit within the confines of the pore (size exclusion) and its interactions with the pore walls (chemical selectivity). Finally, the analyte desorbs at the downstream side of the membrane, establishing a steady-state chemical potential gradient. In this chapter, I provide a brief overview of the models used to understand mass transport through dense and microporous materials, the chemical and physical forces influencing that transport, and the design principles used to apply them to next-generation separations.

1.4 Size Selectivity and Chemical Selectivity

In the design of new membrane materials, two primary design parameters are available: (1) in the Angstrom size regime, chemical control over the pore-wall functionality determines the energetics of pore–analyte interactions, and (2) at the nanoscale, pore size and shape determine the barriers to analytes entering and moving between pores. Often, these axes of control are orthogonal. Consider the case of isoreticular MOFs. Pore size can be tuned by changing the length of the organic ligands.[40] Conversely, through careful choice of ligand, postsynthetic modification, or cation exchange, frameworks with very similar pore architectures but vastly different pore-wall chemistries are accessible.[89] As I discuss in the following section, the size and chemistry of the pores are often considered together when modeling transport, which is most easily understood as a function of the speed and frequency with which analytes traverse the membrane. Nonetheless, these concepts are useful for establishing design principles for the advancement of membrane technology. Ultimately, as all separations necessarily operate on chemical and physical differences between the analytes being separated, those analyte properties determine the respective relevance of pore size and chemistry on membrane performance.

Chemical selectivity in membrane applications is most applicable when the analytes differ substantially in polarizability, electrostatic charge, Lewis acidic/basic character, etc. Increasing the favorability of interactions between membrane materials and a given analyte will typically increase the flux of that analyte. On one extreme, membranes can form reversible bonds with the higher-flux analyte. If the rate of analyte exchange on the reactive sites is sufficiently fast, the effective concentration of that particular analyte is markedly increased, increasing both selectivity and productivity in a process called facilitated transport.[90] However, if the analyte

interacts too strongly with particular moieties in the matrix, movement across the potential well of the bound state is disfavored, slowing transport. Another strategy is to block the transport of certain analytes by designing repulsive pore–analyte interactions.[91] This process is seen in the use of electrostatically charged membrane matrices for ion exclusion.

Pore-size control for size-exclusion separations can be quite effective with even small differences in analyte size when the matrix exhibits appropriate in situ pore dimensions. For example, gaseous propane and propylene can be separated through molecular sieving in the MOF ZIF-8 despite having very similar van der Waals diameters (4.16 and 4.03 Å, respectively).[92,93] This example is also illustrative of the importance of pore dynamics in molecular-sieving applications. The crystal structure of ZIF-8 suggests a selective pore aperture of only 3.6 Å, but Zhang et al. demonstrated that natural fluctuations in the crystal structure permit fast diffusion of analytes up to ~4.1 Å in diameter.[92] As such, size exclusion as a design principle must be considered within the relevant operating conditions of the separation. Common methods for pore-size characterization, such as crystallography and adsorption isotherms, do not necessarily account for pore-dimension fluctuations with changes to solvent environment, temperature, flexibility, etc.[94,95] Understanding analyte size also requires careful treatment. In the simple case of dilute gaseous analytes, multiple measures of size exist that sometimes suggest conflicting results (building on the propane/propylene example, the kinetic diameter of propane is the smaller of the two while the opposite trend holds for the van der Waals diameters).[92] As system complexity increases, the permeating species sometimes includes noncovalent aggregates. In redox-flow battery membranes, analyte sizes are estimated as the radius of gyration of the analyte molecule/ion and its solvent shell, which are quantified using either scattering, electrochemical, or diffusion-ordered NMR spectroscopy (DOSY) methods, or alternatively, computationally using ab initio or semiclassical molecular dynamics (MD) simulations, which also allow desolvation energies to be calculated.[96] A complementary approach to engineering pore architectures is to alter the size of the analyte. In some applications, analyte size can be controlled through oligomerization, polymerization, or the introduction of bulky chemical functionalities without compromising analyte functionality, improving membrane performance with no change to the matrix itself.[97]

Throughout this dissertation, these design principles are carefully considered in turn with respect to the demands of use cases varying from the separation of non-condensable gases the transport of lithium ions through an active battery binder material.

1.5 Transport Fundamentals

The first consideration for transport in microporous materials is distinguishing solution diffusion from molecular sieving. Molecular sieving occurs when the pore size and persistent shape exclude a given species; transport is impossible for that analyte. For analytes that do enter the membrane, permeation in bulk materials, particularly those with low free volume, is commonly viewed from the standpoint of the solution-diffusion model[98]

$$P = \overline{D} \times \overline{S} \tag{1}$$

where P is permeability, and $\overline{D}$ and $\overline{S}$ are concentration-averaged effective diffusion and solubility/sorption coefficients, respectively. Within this model, transport is envisioned to occur via three discrete steps. First, the analyte dissolves into the matrix, diffuses across the film, and

then desorbs at the downstream interface. Therefore, for a binary system of species *i* and *j*, selectivity, α, can be achieved for materials that exhibit differences in molecular diffusion rates or thermodynamic partitioning

$$\alpha_{i/j} = \frac{\overline{D}_i}{\overline{D}_j} \times \frac{\overline{S}_i}{\overline{S}_j} \tag{2}$$

Basic permeation characteristics of microporous materials can be understood in the context of a simple model. Consider gases traveling in the *yz* plane through a microporous material that has within a given unit cell (dimensions $L_y \times L_z$) a pore ($L_{py} \times L_{pz}$) separated from other pores in a 1D channel by narrow windows with width L_{wy} and length L_{wz}.[99] At low pressures, the system enthalpy is described by the chemical potential of the analyte in the free volume, which is dominated by adsorption in the pores. The Henry constant, used here to quantify solubility, is thus

$$H = \frac{\beta V_p}{V} e^{-\beta U_p} \simeq \frac{\beta L_{pz}^2}{L_y L_z} e^{-\beta U_p} \tag{3}$$

where V_p is the pore volume, V is the unit cell volume, β is the inverse product of absolute temperature and the Boltzmann constant, and U_p is the chemical potential of an analyte molecule in the pore. As the chemical potential of analyte molecules in the widows is high, its effect on the system can be neglected. The diffusion constant as determined using the steady-state approximation is

$$D = \frac{1}{4} |v_a| \frac{L_{wy} L_z^2 e^{-\beta U_w}}{L_{pz}^2 e^{-\beta U_p}} \tag{4}$$

where v_a is the average particle velocity at a given temperature and U_w is the chemical potential in the windows. Permeability, the product of solubility and diffusivity, is then

$$P = D \cdot H = \frac{\beta |v_a| L_{wz} L_z}{4 L_y} e^{-\beta U_w} \tag{5}$$

While not all of the assumptions used in constructing this model hold for many real systems, especially when interactions between analytes are strong, it nonetheless demonstrates some interesting relations useful in membrane design. If the volume fraction of the pores increases, the Henry coefficient increases while the diffusion coefficient decreases (and vice versa), affecting no change on the permeability, while increases to the window diameter improve permeability by increasing the diffusion coefficient. Changes to the pore chemistry resulting in more favorable pore–analyte interactions improve solubility but impede diffusion. Similar changes to the window chemistry, however, have little impact on adsorption and can be used to tune diffusion. In practice, most changes to the matrix structure will change the pore–analyte and window–analyte interactions to a similar degree, meaning more favorable matrix–analyte interactions will improve permeability through solubility while having little impact on diffusion.

The solution-diffusion model is generally successful in describing permeability and selectivity trade-offs in materials such as polymers, but microporous materials with persistent free volume consistently show transport properties exceeding those defined by this model.[87] In general, transport through some of these materials can still be described within the framework of the solution-diffusion model, but in significantly rigid and contorted structures, such as glassy porous polymers, amorphous carbons, and zeolites, transport can depend on a combination of transport mechanisms including solution-diffusion transport, molecular sieving, surface diffusion, and Knudsen diffusion (Figure 1.4).[98,100,101]

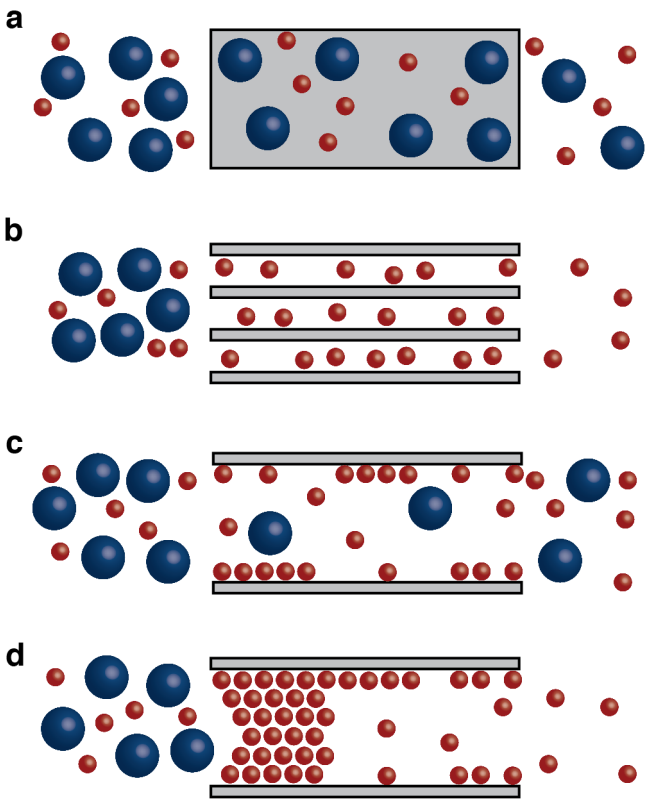

Figure 1.4 Comparison of diffusion mechanisms in polymers and microporous materials. a) Solution-diffusion transport, b) molecular sieving, c) surface diffusion and Knudsen diffusion, and d) capillary condensation.

Analyte diffusion in these cases is mediated by local collisions. When those collisions are most frequently with rigid pore walls, e.g., with low-pressure gases in mesoporous materials, Knudsen diffusion is the dominant transport mechanism.[99] As solubility in this case is roughly the same for all analytes, differences in flux are considered to originate from diffusivity differences, which in turn result from the velocity with which molecules bounce off the pore walls. As these velocities are well described using a Maxwell distribution, the diffusion coefficient is a function of pore diameter, membrane temperature, and analyte mass

$$D_i^k = \frac{2r}{3}\sqrt{\frac{8RT}{\pi M_i}} \tag{6}$$

where D_i^k is the Knudsen diffusion of species i, r is the radius of the capillary, R is the gas constant, T is the temperature of the membrane, and M_i is the molar mass of species i.[102] In amorphous carbons, where sorption into microporous sites is particularly strong, Ash et al. first observed that the preferred diffusion mechanism was a hopping-type mechanism known as surface diffusion (cf. Figure 1.4c).[103] Strong sorption interactions can further influence diffusion through processes such as capillary condensation for gas mixtures, which describes the blocking of adsorption sites by condensable gases (cf. Figure 1.4d). For strongly adsorbing gases, capillary condensation can result in inverted or enhanced gas-phase selectivities when testing gas mixtures instead of pure gases.[104] These types of observations are rare for polymer systems but have been observed in PTMSP and TR polymers.[101,105]

As pore shapes become well ordered, such as those found in crystalline coordination solids, a process known as single-file diffusion can also be observed. This process is similar to capillary condensation and surface diffusion in amorphous carbons and microporous polymers but is significantly more selective due to the uniformity of precisely well-defined 1D channels.[106] In nature, these types of restricted transport mechanisms are found for water transport in aquaporins;[107] analogous transport behavior is predicted and, in some cases, experimentally observed for thin-walled carbon nanotubes[108] and zeolites.[109]

When analyte collisions are most frequent with solvent molecules or other analytes, the effective diffusion coefficient is described using a series of dimensionless factors accounting for pore geometry

$$D_e = \frac{D\varepsilon\delta}{\tau} \tag{7}$$

where D_e is the effective diffusion coefficient through the membrane, D is the diffusion coefficient in the medium filling the pores, ε is the porosity (<1), δ is the constrictivity (≤1), and τ is the tortuosity (>1).[110] The parameter δ describes resistance to flow from increased viscosity through narrow pore apertures, and the parameter τ describes resistance to flow resulting from the winding paths analytes take through the membrane. While porosity can be measured directly using a number of common techniques, including gas adsorption[111] and ellipsometric porosimetry,[112] tortuosity and constrictivity are typically empirical, although advanced X-ray tomography for the direct measurement of tortuosity has been demonstrated.[113]

1.6 Modeling Transport through Microporous Materials

As predictive and mechanistically informative models of specific membrane systems are desirable to direct membrane design, many such descriptions of individual transport systems have been developed. Such theoretical formalisms governing the transport of gases through microporous materials are well developed and illustrative of the types of considerations one must address carefully with analytes generally. We begin our discussion of gas transport in microporous polymers by first considering models used to describe gas dissolution into glassy polymers. The simplest of these is the dual-mode model[114]

$$C = k_{\mathrm{D}}p + C'_{\mathrm{H}}\frac{bp}{1+bp} \tag{8}$$

where C is the concentration of a penetrant in the polymer, k_D is the Henry's law partition coefficient, C_H' is the Langmuir capacity constant, b is the Langmuir affinity constant, and p is pressure. Sorption coefficients are defined as the secant slope of sorption isotherms

$$\overline{S} = \frac{C}{p} = k_D + C_H' \frac{b}{1 + bp} \tag{9}$$

For rubbery elastomers, sorption of nonswelling penetrants can be described using only the parameter k_D.[115] However, for glassy polymers, an additional, Langmuir-type contribution to sorption becomes manifest in experimental isotherms. The dual-mode model captures this behavior by envisaging two distinct "sites" for sorption in amorphous glasses: (1) sorption into Henry's law sites and (2) sorption into Langmuir sites. From a molecular perspective, the dual-mode model does not possess true physical meaning, as there is no proven experimental evidence that supports the presence of discrete sorption sites in glassy polymers.[116] From the perspective of statistical thermodynamics, far more meaningful and truly predictive models for describing gas dissolution into rubbery polymers (Sanchez–Lacombe)[117] and glassy polymers (nonequilibrium lattice fluid, NELF)[118] have been developed. Nevertheless, parameters evaluated from the dual-mode model provide some insight into the potential advantages of using microporous polymers for membrane-based separations. Most importantly, higher total sorption in polymers can be achieved when operating in the glassy state, and higher sorption corresponds to higher permeation rates as predicted by the solution-diffusion model.

The nonequilibrium morphology of high free volume and microporous polymers permits significantly more sorption into glassy polymers than their corresponding elastomers. The terms "free volume" and "microporous" both relate to open spacing within the polymer matrix devoid of electron density. However, "free volume" is a term used to indicate stochastically fluctuating gaps in the free space of the polymer, whereas "microporous" is used to indicate long-lasting, persistent gaps that are significantly immobilized and considered relatively intransient.[119] From the framework of the dual-mode model, the ratio of nonequilibrium to equilibrium sorption can be described at infinite dilution as a ratio of the dual-mode fitting parameters, $C_H'b/k_D$. Figure 1.5 demonstrates that cooling poly(ethylene terephthalate) (PET) below its glass transition temperature (T_g) produces significant nonequilibrium free volume that is responsible for increased CO_2 sorption.[120] For polymers often classified as microporous, such as PTMSP, TR polymers, and PIM-1, the ratio of nonequilibrium to equilibrium sorption for CO_2 at 35 °C often falls within the range of 5–20, indicating that the dominant mechanism of sorption in these polymers is derived from their microporous nature.[121–123]

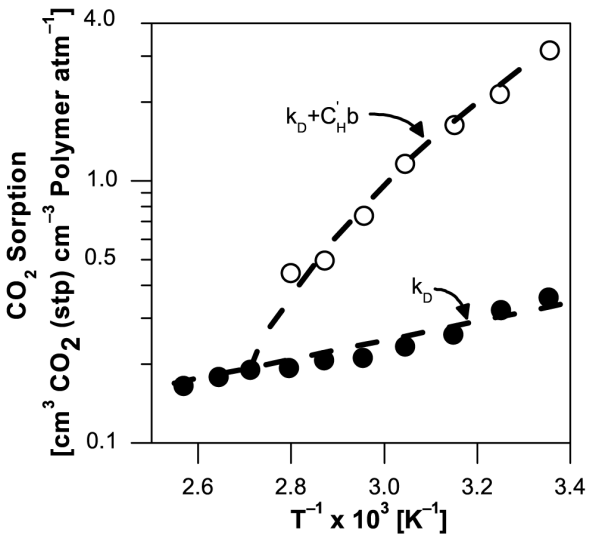

Figure 1.5 Contributions to CO_2 sorption from equilibrium sorption (k_D) and from excess free volume (C'_Hb) above and below the glass transition temperature for PET. Reproduced with permission.[120] 1978, John Wiley & Sons, Inc.

While excess free volume often correlates with increased sorption, the same is not true for sorption selectivity. In general, polymers often characterized as microporous follow the same trends for solubility selectivity as their low free-volume counterparts, including PTMSP,[121] TR polymers,[123,124] and PIMs.[125] These correlations are upheld for a range of FFVs, including 20–24% for PIM-1,[126] 26.3% for TR-1-450,[85,127] and 32–34% for PTMSP.[126] From the standpoint of the dual-mode model, the origins of this invariance in sorption selectivity in the face of significant differences in total sorption correspond to the energetics of gas sorption in the glassy state. The parameter C'_H only begins to manifest itself as the polymer is cooled below its glass transition temperature. When plotted against inverse temperature on a semilog Van't Hoff plot, C'_H exhibits a strong nonlinear dependence. In contrast, an analogous plot of the affinity constant, b, versus inverse temperature reveals linear Van't Hoff type behavior.[120,128] Thus, relative sorption affinities, which are characteristic of b, are invariant to free volume and microporosity.

In contrast to sorption selectivities, diffusion rates and diffusion selectivities are strongly influenced by polymer structure and fractional free volume or microporosity. For illustrative purposes, consider the separation of H_2 from CH_4. H_2 has a kinetic diameter of 2.89 Å compared to 3.8 Å for CH_4, a difference of less than 1 Å.[129] For poly(dimethyl siloxane) (PDMS; $T_g = -123$ °C), an elastomer, H_2/CH_4 diffusion selectivity is only 6,[130,131] whereas H_2/CH_4 diffusion selectivity for a glassy polyimide (benzophenone-3,3′,4,4′-tetracarboxylic dianhydride-*para*-4,4′-oxydianiline, or BTDA-*para*-ODA; T_g = 266 °C) is 280.[132] However, PDMS, the most permeable rubbery polymer known,[130] has an H_2 diffusivity of 1.4×10^{-4} cm^2 s^{-1} compared to only 3.6×10^{-7} cm^2 s^{-1} for that of BTDA-*para*-ODA. This comparison highlights a general trend. Gas diffusion in low free-volume glassy polymers, such as BTDA-*para*-ODA, is significantly reduced due to immobilization of polymer chain segments. However, for high free-volume, microporous glassy polymers, significant nonequilibrium free volume allows for lower activation energies of diffusion, thereby permitting high diffusion rates. For example, PTMSP has an H_2 diffusion coefficient of 2.6×10^{-4} cm^2 s^{-1} and an

H_2/CH_4 diffusion selectivity of 7.6,[121] properties that surpass both the diffusion rate and diffusion selectivity of PDMS (i.e., D = 140 cm^2 s^{-1}, and D_{H_2}/D_{CH_4} = 6).[130]

In polymer systems, the mechanism of gas diffusion has classically been described in analogy to molecular diffusion of liquids using Eyring's transition-state theory.[133] Eyring describes diffusion as a process that occurs through "holes" or gaps in the lattice framework that occasionally open into voids large enough to permit diffusive displacement between lattice sites. Diffusion of these holes, D, can therefore be statistically described by a relationship proposed by Cohen and Turnball[134]

$$D = Ae^{\frac{-\gamma\nu^*}{\nu_f}} \tag{10}$$

where A is a temperature-independent preexponential factor, ν_f is the volume of the transient holes, or free-volume elements, γ is a numerical factor to account for overlapping free-volume elements, and υ^* is the molecular volume of the diffusing diluent (or analyte). The basic form of this relationship, which was further expanded to describe polymer–diluent systems by Fujita,[135] predicts a few basic correlations for molecular diffusion in polymers. Specifically, faster diffusion occurs for smaller molecules and for larger or interconnected free-volume elements. Free volume is often determined through group contribution methods[136] or through spectroscopic characterization such as positron annihilation lifetime spectroscopy.[137]

Diffusion can similarly be described as an energetically activated process using an Arrhenius relationship of similar form to the equation proposed by Cohen and Turnball[138]

$$D = D_0 e^{\frac{-E_D}{RT}} \tag{11}$$

where D_0 corresponds to entropic contributions to activation, E_D is the activation energy of diffusion, R is the ideal gas constant, and T is the absolute temperature. From this relationship, Meares proposed that the energy required for a molecule to make a diffusive jump correlates with the energy required to separate the surrounding media with sufficient space to accommodate the cross section of the diffusant.[139] Regardless of whether free-volume considerations or activated diffusion considerations are used to describe the mechanism of diffusion in polymers, the slope of the upper bound relationships originally described empirically by Robeson can be fundamentally described within the framework of either of these models.[87,140,141] These upper bound relationships describe a consistent trade-off between permeability and selectivity observed for polymer membranes.

When the analytes to be separated are more strongly interacting than dilute gases, as is the case for liquids and solvated species, the nanoscale dimensions of micropores often lead to behaviors deviating from continuum fluid dynamics, and MD simulations are necessary to model these systems.[142,143] The distribution and diffusion of nanoconfined analytes strongly depend on analyte–analyte and analyte–matrix interactions, both of which change with time and position in the system. MD simulations can capture these complicated interactions, such as transient hydrogen-bond networks that influence the barriers to permeation, as well as other relevant properties of the system (e.g., solvent density or viscosity fluctuations).[143] Often, these studies highlight key aspects of the system relevant to membrane performance, and analytical models that qualitatively track with the simulated results are later developed to provide a greater description of the system.[59] Water and aqueous solutions are common subjects of these studies,

as they are interesting from both basic science and application-driven perspectives. Sometimes, the models and intuitions of traditional fluid dynamics hold true in microporous transport; however, simulation is usually needed to ascertain when this is the case.

1.7 Polymeric Membranes for Gas Separations

1.7.1 Single-Component Membranes

Polymer membranes with microporous character have shown promising separation efficiency for several industrially relevant gas pairs. PIMs are particularly noteworthy in this regard (i.e., as upper bound membrane materials). Since the mobility of the polymer backbone is not the limiting kinetic process in mediating gas transport, optimization of the membrane transport properties in turn calls for the rigidification of the backbone, to the point of minimizing the number of rotatable bonds. PIMs have evolved from ladder polymers, typically bearing either kinked bicyclic or spirocyclic aromatic monomers along their backbone,[83] to rigid polymers that are fully constrained and decorated with bulky groups.[144] PIMs have demonstrated superior performance in separating CO_2/CH_4 and other gas pairs:[145–147] methanol-treated PIM-1 membranes have demonstrated CO_2 permeabilities as high as 11,200 Barrer.[148] Moreover, tetrazolate derivatives of PIM-1 (e.g., TZPIM-1 or TZPIM-2) offer CO_2/N_2 selectivity approaching 30.[146] PIMs are likely to continue to push the bounds of the Robeson permeability-selectivity trade-off, provided monomer-level structural motifs directing pore network architectures advance significantly beyond present designs.[7,18,149,150]

Thermally rearranged polymers have also found success in improving efficiency and productivity for gas separation membranes. First reported by Park et al. in 2007,[85] TR polymers are formed from a solid-state reaction of poly(hydroxyimide)s, where the hydroxyl group is *ortho*-positioned to the diamine monomer. These polyimides, which can be cast as films, are heated, typically to temperatures between 350 and 450 °C, thereby inducing an intramolecular cyclization reaction between the hydroxyl group and the imide carbonyl to form polybenzoxazoles.[127,151] Once converted, these polymers become insoluble in their casting solvent, possibly due to intermolecular crosslinking reactions, which endows these materials with excellent plasticization resistance.[105] Because these reactions take place in the solid state, slight variations in the synthesis of the polyimide precursors significantly influence transport behavior for the resulting TR polymer.[152] For example, modifying the hydroxyl group on the polymer backbone to larger *ortho*-positioned functional groups can be used to effectively engineer free volume and free-volume distribution in these materials, resulting in significant improvements in permeability.[153,154]

TR polymers first showed promising transport properties and plasticization resistance for CO_2/CH_4 separation,[85] but additional studies suggest that TR polymers could find use in CO_2/N_2,[149] O_2/N_2,[149] and olefin/paraffin separations.[155] Of practical interest, TR polymers are derived from solution processable polyimide precursors, a class of polymers currently deployed by Air Liquide and Ube for industrial gas separation membranes, so TR polymers have a logical pathway to industrial deployment using currently available membrane formation methods.[162] Of note, TR polymers have already been formed into hollow-fiber geometries.[156]

Of particular interest is understanding and tuning the free-volume architecture of TR polymers. Initial reports indicated a sharpening of the free-volume distributions due to a coalescence of free-volume elements during thermal rearrangement,[85] but additional studies have reported other potential phenomena, such as the formation of bimodal free-volume

distributions,[152,157] or more traditional free-volume trade-off behavior such as unimodal free-volume distributions that follow upper bound type limitations.[155] The origins of these competing and complex morphologies of TR polymers likely relate to slight differences in polymer preparation methods. As described in the theoretical section of this paper, transport in these microporous-like materials occurs predominantly through their nonequilibrium packing morphology, so the method by which they are prepared has direct implications on their performance.

1.7.2 Composite Membranes

An attractive means of enhancing membrane properties beyond those of single component membranes is to employ composites, which are combinations of two or more components that interact synergistically to improve gas separation performance. Compositing has primarily been considered in the context of mixed-matrix membranes (MMMs) consisting of a permselective filler phase dispersed into a polymer matrix. The filler phase in an MMM is often a zeolite,[201–203] MOF,[158–163] silica,[164] CMS,[165,166] or carbon nanotube.[167] The MMM approach has major advantages, as well as challenges, when compared to pure component systems. In many instances, composites have improved separation performance over neat polymer membranes, as well as better processability compared with pure component systems such as CMS membranes or neat MOF membranes. Major challenges with the approach include developing composites that are defect free, mechanically robust, and have high permeance.

The primary advantage that composites have over neat polymers is their gas separation performance, as there are numerous examples of membranes with gas separation performance that exceed the Robeson upper bound for neat polymers. There are two primary mechanisms by which the filler phase of a mixed-matrix system imparts improved separation performance on the membrane, including diffusive enhancements (or size-sieving) and adsorptive enhancements. Although transport through the filler phase does not necessarily follow the solution-diffusion model, it can still contribute to the overall solubility or diffusivity of various components in the membrane. In this way, fillers can act primarily as diffusive-selective particles, or sieves, or as solubility-selective particles or adsorbents. To see how each of these approaches might be leveraged for a separation, it is first necessary to compare the physical properties of commonly targeted gas molecules. Table 1.1 lists the relevant physical properties of gas molecules commonly considered for gas separations.

The differences in the molecular properties for gas pairs can be leveraged to conduct a separation. In more traditional, thermal-based separations, the differences in condensability, or boiling point, are leveraged. In membrane-based separations, a molecule's ability to diffuse is related to its kinetic diameter and its adsorptive partitioning is related to properties such as dipole moment (μ), quadrupole moment (Θ), and polarizability (α). For example, C_2H_4/C_2H_6 mixtures are particularly challenging to separate because these two molecules have similar boiling points and kinetic diameters, while in contrast, H_2/C_3H_8 mixtures are relatively simple to separate using thermal, diffusive, or adsorptive mechanisms.

When targeting a specific gas pair and choosing materials for a composite membrane, it is important to keep in mind the mechanism that will enable the separation. While there are many examples of fillers employed in the literature, we can compare specific examples of how sieving fillers are used to improve olefin/paraffin or CO_2-based separations.

Table 1.1 Relevant physical properties of light gases.[44]

Gas	Kinetic diameter / Å	Boiling point / K	Dipole moment, μ / 10^{-18} esu m	Quadrupole moment, Θ / 10^{-26} esu m^2	Polarizability, α / 10^{-25} cm^3
CO_2	3.3	216.6	0	4.30	29.11
N_2	3.64–3.80	77.4	0	1.52	17.403
H_2	2.83–2.89	20.3	0	0.66	8.042
CH_4	3.76	111.7	0	0	25.93
C_2H_4	4.16	169.4	0	1.50	42.52
C_2H_6	4.44	184.6	0	0.65	44.3–44.7
C_3H_6	4.68	225.5	0.37	0	62.6
C_3H_8	4.3	231.0	0.084	0	62.9–63.7

Diffusivity-Based Enhancements: The most prevalent way to impart permselectivity in a composite is through the addition of diffusive-selective, or size-sieving, particles. This approach has been widely used to enhance the selectivity for CO_2/CH_4, CO_2/N_2, H_2/CO_2, and C_3H_6/C_3H_8 separations. Specifically, the sieve leverages differences in the kinetic diameter between the two permeating components to achieve selectivity. The sieve then has an intrinsic permeability and selectivity of its own, and that is imparted to the composite membrane proportionally to the volume fraction of sieve in the composite. The resulting permeability of a composite that contains sieving particles is given by the Maxwell relationship, which is widely used to predict the permeability of composites[168]

$$P_{MMM} = P_P * \left[\frac{P_S + 2P_P - 2\phi(P_P - P_S)}{P_S + 2P_P + \phi(P_P - P_S)} \right] \tag{12}$$

where P_{MMM} is the permeability of the composite, P_P and P_S are the permeabilities of the polymer phase and sieve phase, respectively, and ϕ is the volume fraction of the film that is occupied by the sieve phase. This relationship is useful for determining the intrinsic properties of the sieve phase and can allow for the determination of composite properties at various sieve loadings.

One of the main challenges with forming composites using sieving particles is in finding a filler phase that has a pore diameter that can discriminate effectively between the two permeating gas molecules while in the polymer matrix. Two prominent examples of this effect being successfully implemented for C_3H_6/C_3H_8 and CO_2/CH_4 separations are by Zhang et al.[169] and Rodenas et al.,[161] respectively. In the case of C_3H_6/C_3H_8 separations, it was found that a zeolitic imidazolate framework (ZIF-8) provides exceptional selectivity between these two molecules based on their kinetic diameters. ZIF-8 is comprised of Zn^{2+} ions linked through

methyl-imidazolate units into a sodalite-type MOF. This material was shown not to have any specific adsorptive affinity for propylene over propane, yet when used to form an MMM exhibits significantly enhanced permeation properties. Figure 1.6 shows the adsorption isotherms of ZIF-8 as well as the permeation properties of the composite membranes.

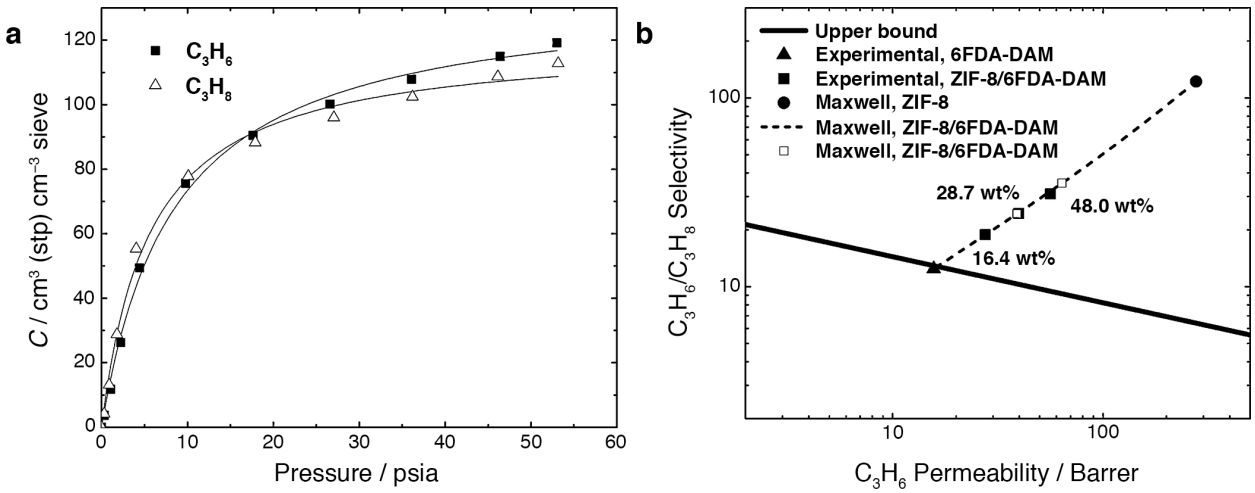

Figure 1.6 Adsorption and separation performance of ZIF-8 and composite membranes. a) Adsorption isotherms of C_3H_6 and C_3H_8 in ZIF-8 and b) membrane performance on the C_3H_6/C_3H_8 upper bound for various loadings of ZIF-8 as well as the corresponding Maxwell predictions. Reproduced with permission.[162] Copyright 2012, Elsevier.

As shown in Figure 1.6, the improved permeability and permselectivity for ZIF-8 MMMs do not originate from an adsorption mechanism. Similarly, the rate of adsorption data does not suggest significantly higher diffusivity for C_3H_6 over C_3H_8 in neat ZIF-8. While the permeability of olefins and paraffins in ZIF-8 elegantly matches the Maxwell model, the intrinsically high permselectivity found for ZIF-8 for C_3H_6/C_3H_8 separations could not have been predicted by measuring equilibrium adsorption isotherms and rates of adsorption alone; indeed, diffusion kinetics are key compared to the thermodynamic partitioning.[92]

Solubility-Based Enhancements: While sieving filler materials increase diffusive selectivity by leveraging differences in analyte kinetic diameters, MMM fillers can also tune the solubility component of permeability to improve permselectivity. This approach has been successfully employed to improve the selectivity for CO_2/N_2,[160] CO_2/CH_4,[163,170] and C_2H_4/C_2H_6[158,171] separations. There are numerous porous materials that have been developed that show very high adsorptive selectivities for CO_2-based and C_2H_4/C_2H_6 separations. Most notable are MOFs with coordinatively unsaturated metal centers[172] as well as various types of porous materials that have amine functionality.

To elaborate further, we will consider a system that was used to improve all three of these separations, namely M_2(dobdc) (M = Mg, Mn, Co, Ni, and Zn) MOF nanocrystals embedded within polyimides. Improving C_2H_4/C_2H_6 separations using M_2(dobdc) was demonstrated by Bachman et al.,[158] and this improvement was shown to occur through an adsorption-enhanced mechanism. Most neat polymers exhibit permselectivity for C_2H_4 over C_2H_6 based on a complex trade-off between diffusion and solubility selectivity. Diffusion selectivity favors the smaller C_2H_4 molecule, but sorption selectivity slightly favors the more condensable C_2H_6 molecule. Therefore, from the exclusive perspective of solubility selectivity, neat polymers operate at a

fundamental disadvantage for a C_2H_4/C_2H_6 separation. Interestingly, the limited sorption-based selectivity can be improved significantly through the incorporation of highly selective nanocrystals of M_2(dobdc), which preferentially interact with C_2H_4 over C_2H_6. This preferential olefinic binding leads to composite films that are selective for C_2H_4 in both solubility and diffusivity (Figure 1.7). Similarly, improving CO_2 permselectivity by incorporating M_2(dobdc) was achieved by Bae and Long,[160] where the coordinatively unsaturated metal sites in Mg_2(dobdc) allowed for improved solubility selectivity and thus permselectivity when combined with the polyimide, 6FDA-DAM (Figure 1.8). Similar phenomena were demonstrated for CO_2/CH_4 separations using Ni_2(dobdc) nanoparticle fillers in a number of polymer matrices.[163] For all three of these separations, the highly selective M_2(dobdc) MOFs have improved permselectivity in composite membranes via adsorption enhancement. Going forward, improvements to adsorption-enhanced membranes can be achieved through the development of more selective adsorbents.

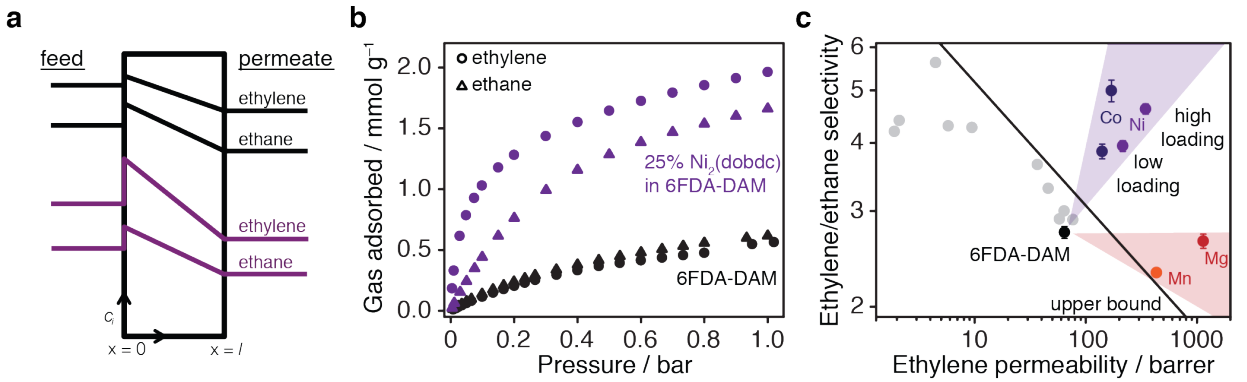

Figure 1.7 Adsorption-enhanced composite membranes for C_2H_4/C_2H_6 separation. a) By increasing the relative concentration gradient for ethylene across the membrane using the adsorptive selectivity in the MOF, there is a greater driving force for mass transport across the film. b) The ethylene and ethane isotherms in neat 6FDA-DAM, as well as the composite with 25 wt% Ni_2(dobdc), indicating the large increase of gas adsorbed into the film as well as an ethylene adsorptive selectivity due to incorporation of the adsorbent. c) The resulting permselectivities at 2 bar and 35 °C for variants of M_2(dobdc) (M = Mg, Mn, Co, and Ni). MOF content in each membrane by weight are 10% and 33% for Co_2(dobdc), 6% and 25% for Ni_2(dobdc), 23% for Mg_2(dobdc), and 13% for Mn_2(dobdc). Reproduced with permission.[158] Copyright 2016, Nature Publishing Group.

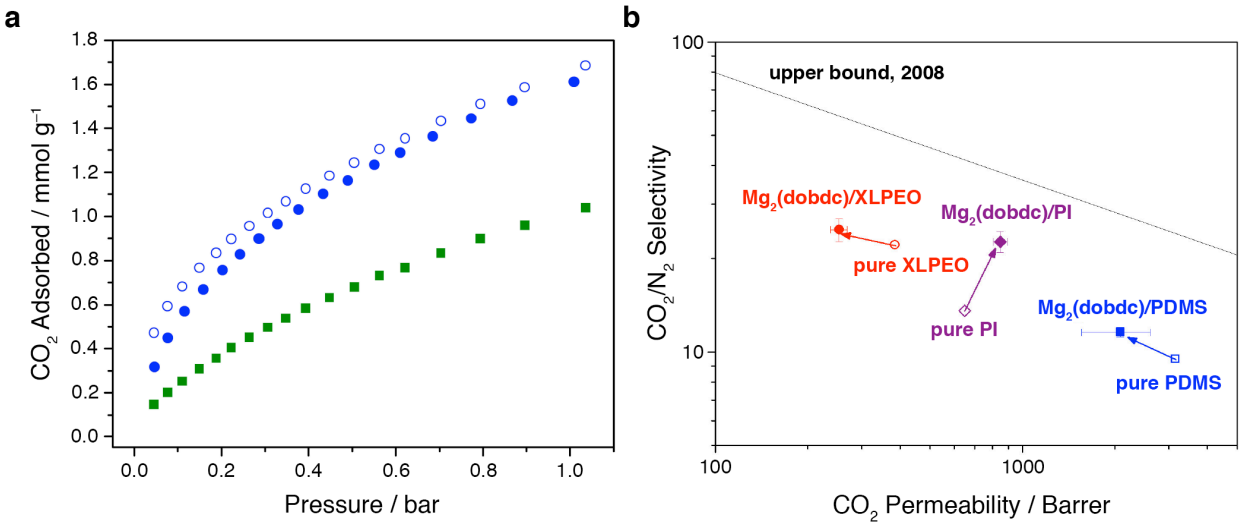

Figure 1.8 Adsorption-enhanced CO_2/N_2 separations using $Mg_2(dobdc)$. a) Equilibrium adsorption isotherms in neat 6FDA-DAM (green squares), 10% $Mg_2(dobdc)$ in 6FDA-DAM (blue circles, filled), and the predicted amount adsorbed based on the pure component isotherms (blue circles, open). b) Performance of various $Mg_2(dobdc)$ composites on the CO_2/N_2 upper bound. Reproduced with permission.[160] Copyright 2013, the Royal Society of Chemistry.

1.8 Acknowledgements

I would like to thank all of the coauthors responsible for making this work possible, including Changyi Li, Zachary Smith, Jonathan Bachman, Lorenzo Maserati, Jeffrey Long, and Brett Helms. Changyi Li and Brett Helms were supported by the Joint Center for Energy Storage Research, an Energy Innovation Hub funded by the U.S. Department of Energy, Office of Science, Office of Basic Energy Sciences. Zachary Smith, Jonathan Bachman, Lorenzo Maserati, Jeffrey Long and I were supported by the Center for Gas Separations Relevant to Clean Energy Technologies, an Energy Frontier Research Center funded by the U.S. Department of Energy, Office of Science, Basic Energy Sciences under Award No. DE-SC0001015. Brett Helms acknowledges additional support from The Molecular Foundry, which is supported by the Office of Science, Office of Basic Energy Sciences, of the U.S. Department of Energy under Contract No. DE-AC02-05CH11231.

1.9 References

1. D. S. Sholl, R. P. Lively, *Nature* **2016**, *532*, 435.
2. a) C. S. Cundy, P. A. Cox, *Microporous Mesoporous Mater.* **2005**, *82*, 1; b) C. S. Cundy, P. A. Cox, *Chem. Rev.* **2003**, *103*, 663.
3. a) N. Stock, S. Biswas, *Chem. Rev.* **2012**, *112*, 933; b) O. K. Farha, J. T. Hupp, *Acc. Chem. Res.* **2010**, *43*, 1166; c) H. Furukawa, K. E. Cordova, M. O'Keeffe, O. M. Yaghi, *Science* **2013**, *341*, 1230444.
4. H. Dai, *Acc. Chem. Res.* **2002**, *35*, 1035.
5. S. M. Saufi, A. F. Ismail, *Carbon* **2004**, *42*, 241.
6. R. Dawson, A. I. Cooper, D. J. Adams, *Prog. Polym. Sci.* **2012**, *37*, 530.
7. N. B. McKeown, P. M. Budd, *Chem. Soc. Rev.* **2006**, *35*, 675.
8. D. T. Bong, T. D. Clark, J. R. Granja, M. R. Ghadiri, *Angew. Chem. Int. Ed.* **2001**, *40*, 988.
9. N. L. Rosi, *Science* **2003**, *300*, 1127.

10. J. Lee, O. K. Farha, J. Roberts, K. A. Scheidt, S. T. Nguyen, J. T. Hupp, *Chem. Soc. Rev.* **2009**, *38*, 1450.
11. K. Tanabe, W. Hölderich, *Appl. Catal. A* **1999**, *181*, 399.
12. A. Corma, *J. Catal.* **2003**, *216*, 298.
13. R. S. Haszeldine, *Science* **2009**, *325*, 1647.
14. M. Elimelech, W. A. Phillip, *Science* **2011**, *333*, 712.
15. T. M. McDonald, W. R. Lee, J. A. Mason, B. M. Wiers, C. S. Hong, J. R. Long, *J. Am. Chem. Soc.* **2012**, *134*, 7056.
16. G. Hummer, J. C. Rasaiah, J. P. Noworyta, *Nature* **2001**, *414*, 188.
17. L. Ruiz, Y. Wu, S. Keten, *Nanoscale* **2015**, *7*, 121.
18. P. M. Budd, N. B. McKeown, *Polym. Chem.* **2010**, *1*, 63.
19. a) C. Baerlocher, L. B. McCusker, D. H. Olson, *Atlas of Zeolite Framework Types*, Elsevier Science B.V., Amsterdam, 2007; b) D. W. Breck, *Zeolite Molecular Sieves: Structure, Chemistry and Use*, John Wiley & Sons, New York, London, Sydney, Toronto, 1974.
20. E. M. Flanigen, J. M. Bennett, R. W. Grose, J. P. Cohen, R. L. Patton, R. M. Kirchner, J. V. Smith, *Nature* **1978**, *271*, 512.
21. a) D. M. Chapman, A. L. Roe, *Zeolites* **1990**, *10*, 730; b) P. T. Tanev, M. Chibwe, T. J. Pinnavaia, *Nature* **1994**, *368*, 321.
22. a) M. E. Davis, C. Saldarriaga, C. Montes, J. Garces, C. Crowdert, *Nature* **1988**, *331*, 698; b) S. T. Wilson, B. M. Lok, C. A. Messina, T. R. Cannan, E. M. Flanigen, *J. Am. Chem. Soc.* **1982**, *104*, 1146; c) M. Estermann, L. B. McCusker, C. Baerlocher, A. Merrouche, H. Kessler, *Nature* **1991**, *352*, 320; d) B. M. Lok, C. A. Messina, R. L. Patton, R. T. Gajek, T. R. Cannan, E. M. Flanigen, *J. Am. Chem. Soc.* **1984**, *106*, 6092.
23. A. F. Cronsted, *Akad. Handl.* **1756**, *17*, 20.
24. M. E. Davis, R. F. Lobo, *Chem. Mater.* **1992**, *4*, 756.
25. A. K. Cheetham, G. Férey, T. Loiseau, *Angew. Chem. Int. Ed.* **1999**, *38*, 3268.
26. E. M. Flanigen, *Zeolites and Molecular Sieves an Historical Perspective*, Vol. 58, 1991.
27. N. Y. Chen, T. F. Degnan, Jr., C. M. Smith, *Molecular Transport and Reaction in Zeolites: Design and Application of Shape Selective Catalysis*, Wiley-VCH, New York, 1995.
28. S. Babel, T. A. Kurniawan, *J. Hazard. Mater.* **2003**, *97*, 219.
29. a) W. Hölderich, M. Hesse, F. Näumann, *Angew. Chem. Int. Ed. Engl.* **1988**, *27*, 226; b) P. B. Venuto, *Microporous Mater.* **1994**, *2*, 297; c) V. V. Speybroeck, K. Hemelsoet, L. Joos, M. Waroquier, R. G. Bell, C. R. A. Catlow, *Chem. Soc. Rev.* **2015**, *44*, 7044; d) W. Vermeiren, J.-P. Gilson, *Top. Catal.* **2009**, *52*, 1131.
30. a) J. J. Pluth, J. V. Smith, *J. Am. Chem. Soc.* **1983**, *105*, 1192; b) J. J. Pluth, J. V. Smith, *J. Am. Chem. Soc.* **1980**, *102*, 4704; c) J. J. Pluth, J. V. Smith, *J. Phys. Chem.* **1979**, *83*, 741.
31. J. Gascon, F. Kapteijn, B. Zornoza, V. Sebastián, C. Casado, J. Coronas, *Chem. Mater.* **2012**, *24*, 2829.
32. a) M. Y. Jeon, D. Kim, P. Kumar, P. S. Lee, N. Rangnekar, P. Bai, M. Shete, B. Elyassi, H. S. Lee, K. Narasimharao, S. N. Basahel, S. Al-Thabaiti, W. Xu, H. J. Cho, E. O. Fetisov, R. Thyagarajan, R. F. DeJaco, W. Fan, K. A. Mkhoyan, J. I. Siepmann, M. Tsapatsis, *Nature* **2017**, *543*, 690; b) G.-E Wang, G. Xu, B.-W. Liu, M.-S. Wang, M.-S. Yao, G.-C. Guo, *Angew. Chem. Int. Ed.* **2015**, *55*, 514; c) S. V. Krivovichev, V. Kahlenberg, R. Kaindl, E. Mersdorf, I. G. Tananaev, B. F. Myasoedov, *Angew. Chem. Int. Ed.* **2005**, *44*,

1134; d) C. D. Malliakas, M. G. Kanatzidis, *J. Am. Chem. Soc.* **2006**, *128*, 6538; e) A. Choudhury, P. K. Dorhout, *J. Am. Chem. Soc.* **2007**, *129*, 9270; f) S. P. Albu, A. Ghicov, J. M. Macak, R. Hahn, P. Schmuki, *Nano Lett.* **2007**, *7*, 1286.
33. O. M. Yaghi, G. Li, H. Li, *Nature* **1995**, *378*, 703.
34. K. S. Park, Z. Ni, A. P. Côté, J. Y. Choi, R. Huang, F. J. Uribe-Romo, H. K. Chae, M. O'Keeffe, O. M. Yaghi, *Proc. Natl. Acad. Sci. U. S. A.* **2006**, *103*, 10186.
35. a) M. O'Keeffe, O. M. Yaghi, *Chem. Rev.* **2012**, *112*, 675; b) N. W. Ockwig, O. Delgado-Friedrichs, M. O'Keeffe, O. M. Yaghi, *Acc. Chem. Res.* **2005**, *38*, 176.
36. a) Z. Wang, S. M. Cohen, *Chem. Soc. Rev.* **2009**, *38*, 1315; b) S. M. Cohen, *Chem. Rev.* **2012**, *112*, 970.
37. O. K. Farha, I. Eryazici, N. C. Jeong, B. G. Hauser, C. E. Wilmer, A. A. Sarjeant, R. Q. Snurr, S. T. Nguyen, A. Ö. Yazaydın, J. T. Hupp, *J. Am. Chem. Soc.* **2012**, *134*, 15016.
38. H. Furukawa, N. Ko, Y. B. Go, N. Aratani, S. B. Choi, E. Choi, A. Ö. Yazaydin, R. Q. Snurr, M. O'Keeffe, J. Kim, O. M. Yaghi, *Science* **2010**, *329*, 424.
39. B. Chen, S. Xiang, G. Qian, *Acc. Chem. Res.* **2010**, *43*, 1115.
40. M. Eddaoudi, J. Kim, N. Rosi, D. Vodak, J. Wachter, M. O'Keeffe, O. M. Yaghi, *Science* **2002**, *295*, 469.
41. a) S. Ma, H.-C. Zhou, *Chem. Commun.* **2010**, *46*, 44; b) L. J. Murray, M. Dincă, J. R. Long, *Chem. Soc. Rev.* **2009**, *38*, 1294.
42. a) L. E. Kreno, K. Leong, O. K. Farha, M. Allendorf, R. P. Van Duyne, J. T. Hupp, *Chem. Rev.* **2012**, *112*, 1105; b) M.-S. Yao, W.-X. Tang, G.-E Wang, B. Nath, G. Xu, *Adv. Mater.* **2016**, *28*, 5229; c) W.-T. Koo, S.-J. Choi, S.-J. Kim, J.-S. Jang, H. L. Tuller, I.-D. Kim, *J. Am. Chem. Soc.* **2016**, *138*, 13431; d) M. G. Campbell, M. Dincă, *Sensors*, **2017**, *17*, 1108; e) M. G. Campbell, D. Sheberla, S. F. Liu, T. M. Swager, M. Dincă, *Angew. Chem. Int. Ed.*, **2015**, *54*, 4349.
43. J.-R. Li, J. Sculley, H.-C. Zhou, *Chem. Rev.* **2012**, *112*, 869.
44. J.-R. Li, R. J. Kuppler, H.-C. Zhou, *Chem. Soc. Rev.* **2009**, *38*, 1477.
45. D. J. Tranchemontagne, J. R. Hunt, O. M. Yaghi, *Tetrahedron* **2008**, *64*, 8553.
46. A. P. Côté, A. I. Benin, N. W. Ockwig, M. O'Keeffe, A. J. Matzger, O. M. Yaghi, *Science* **2005**, *310*, 1166.
47. J. Fu, S. Das, G. Xing, T. Ben, V. Valtchev, S. Qiu, *J. Am. Chem. Soc.* **2016**, *138*, 7673.
48. H. Furukawa, O. M. Yaghi, *J. Am. Chem. Soc.* **2009**, *131*, 8875.
49. a) C. R. DeBlase, K. Hernández-Burgos, K. E. Silberstein, G. G. Rodríguez-Calero, R. P. Bisbey, H. D. Abruña, W. R. Dichtel, *ACS Nano* **2015**, *9*, 3178; b) C. R. DeBlase, K. E. Silberstein, T.-T. Truong, H. D. Abruña, W. R. Dichtel, *J. Am. Chem. Soc.* **2013**, *135*, 16821; c) C. R. Mulzer, L. Shen, R. P. Bisbey, J. R. McKone, N. Zhang, H. D. Abruña, W. R. Dichtel, *ACS Cent. Sci.* **2016**, *2*, 667; d) J.-S. M. Lee, T.-H. Wu, B. M. Alston, M. E. Briggs, T. Hasell, C.-C. Hu, A. I. Cooper, *J. Mater. Chem. A* **2016**, *4*, 7665.
50. a) Z. Xiang, D. Cao, *J. Mater. Chem. A* **2013**, *1*, 2691; b) S.-Y. Ding, W. Wang, *Chem. Soc. Rev.* **2013**, *42*, 548.
51. a) S. Iijima, *Nature* **1991**, *354*, 56; b) J. Hone, M. Whitney, C. Piskoti, A. Zettl, *Phys. Rev. B* **1999**, *59*, R2514.
52. a) H. Dai, E. W. Wong, C. M. Lieber, *Science* **1996**, *272*, 523; b) T. W. Ebbesen, H. J. Lezec, H. Ghaemi, T. Thio, P. Wolff, *Nature* **1998**, *391*, 667.
53. M. M. J. Treacy, T. W. Ebbesen, J. M. Gibson, *Nature* **1996**, *381*, 678.

54. a) H. Kanzow, C. Lenski, A. Ding, *Phys. Rev. B* **2001**, *63*, 125402; b) H. Ago, T. Komatsu, S. Ohshima, Y. Kuriki, M. Yumura, *Appl. Phys. Lett.* **2000**, *77*, 79.
55. a) K. Balasubramanian, M. Burghard, *Small* **2005**, *1*, 180; b) D. Tasis, N. Tagmatarchis, A. Bianco, M. Prato, *Chem. Rev.* **2006**, *106*, 1105; c) S. S. Wong, E. Joselevich, A. T. Woolley, C. L. Cheung, C. M. Lieber, *Nature* **1998**, *394*, 52.
56. S. K. Bhatia, H. Chen, D. S. Sholl, *Mol. Simul.* **2005**, *31*, 643.
57. C. Y. Lee, W. Choi, J.-H. Han, M. S. Strano, *Science* **2010**, *329*, 1320.
58. H. Liu, J. He, J. Tang, H. Liu, P. Pang, D. Cao, P. Krstic, S. Joseph, S. Lindsay, C. Nuckolls, *Science* **2010**, *327*, 64.
59. D. Cohen-Tanugi, J. C. Grossman, *Nano Lett.* **2012**, *12*, 3602.
60. H. Suda, K. Haraya, *J. Phys. Chem. B* **1997**, *101*, 3988.
61. J. Koresh, A. Soffer, *J. Chem. Soc. Faraday Trans. 1* **1980**, *76*, 2457.
62. a) J.-i. Hayashi, M. Yamamoto, K. Kusakabe, S. Morooka, *Ind. Eng. Chem. Res.* **1995**, *34*, 4364; b) C. W. Jones, W. J. Koros, *Carbon* **1994**, *32*, 1419; c) M. G. Sedigh, L. Xu, T. T. Tsotsis, M. Sahimi, *Ind. Eng. Chem. Res.* **1999**, *38*, 3367.
63. A. B. Fuertes, D. M. Nevskaia, T. A. Centeno, *Microporous Mesoporous Mater.* **1999**, *33*, 115.
64. D. Q. Vu, W. J. Koros, S. J. Miller, *Ind. Eng. Chem. Res.* **2002**, *41*, 367.
65. H. Hatori, Y. Yamada, M. Shiraishi, H. Nakata, S. Yoshitomi, *Carbon* **1992**, *30*, 305.
66. a) A. J. Bird, D. L. Trimm, *Carbon* **1983**, *21*, 177; b) Y. D. Chen, R. T. Yang, *Ind. Eng. Chem. Res.* **1994**, *33*, 3146.
67. W. Shusen, Z. Meiyun, W. Zhizhong, *J. Membr. Sci.* **1996**, *109*, 267.
68. T. A. Centeno, A. B. Fuertes, *Carbon* **2000**, *38*, 1067.
69. a) W. N. W. Salleh, A. F. Ismail, *Sep. Purif. Technol.* **2012**, *88*, 174; b) A. B. Fuertes, *Carbon* **2001**, *39*, 697; c) W. N. W. Salleh, A. F. Ismail, T. Matsuura, M. S. Abdullah, *Sep. Purif. Rev.* **2011**, *40*, 261.
70. A. F. Ismail, L. I. B. David, *J. Membr. Sci.* **2001**, *193*, 1.
71. Y. Rong, D. He, A. Sanchez-Fernandez, C. Evans, K. J. Edler, R. Malpass-Evans, M. Carta, N. B. McKeown, T. J. Clarke, S. H. Taylor, A. J. Wain, J. M. Mitchels, F. Marken, *Langmuir* **2015**, *31*, 12300.
72. V. Percec, A. E. Dulcey, V. S. K. Balagurusamy, Y. Miura, J. Smidrkal, M. Peterca, S. Nummelin, U. Edlund, S. D. Hudson, P. A. Heiney, H. Duan, S. N. Magonov, S. A. Vinogradov, *Nature* **2004**, *430*, 764.
73. J. T. Davis, G. P. Spada, *Chem. Soc. Rev.* **2007**, *36*, 296.
74. a) D. A. Hines, E. R. Darzi, E. S. Hirst, R. Jasti, P. V. Kamat, *J. Phys. Chem. A* **2015**, *119*, 8083; b) M. R. Golder, R. Jasti, *Acc. Chem. Res.* **2015**, *48*, 557.
75. D. Zhao, J. S. Moore, *Chem. Commun.* **2003**, *0*, 807.
76. M. R. Ghadiri, J. R. Granja, R. A. Milligan, D. E. McRee, N. Khazanovich, *Nature* **1993**, *366*, 324.
77. R. Hourani, C. Zhang, R. van der Weegen, L. Ruiz, C. Li, S. Keten, B. A. Helms, T. Xu, *J. Am. Chem. Soc.* **2011**, *133*, 15296.
78. C. Reiriz, M. Amorín, R. García-Fandiño, L. Castedo, J. R. Granja, *Org. Biomol. Chem.* **2009**, *7*, 4358.
79. T. Xu, N. Zhao, F. Ren, R. Hourani, M. T. Lee, J. Y. Shu, S. Mao, B. A. Helms, *ACS Nano* **2011**, *5*, 1376.

80. a) J. Sánchez-Quesada, M. P. Isler, M. R. Ghadiri, *J. Am. Chem. Soc.* **2002**, *124*, 10004; b) S. Fernandez-Lopez, H.-S. Kim, E. C. Choi, M. Delgado, J. R. Granja, A. Khasanov, K. Kraehenbuehl, G. Long, D. A. Weinberger, K. M. Wilcoxen, M. R. Ghadiri, *Nature* **2001**, *412*, 452.
81. L. Zang, Y. Che, J. S. Moore, *Acc. Chem. Res.* **2008**, *41*, 1596.
82. V. P. Shantarovich, I. B. Kevdina, Y. P. Yampolskii, A. Y. Alentiev, *Macromolecules* **2000**, *33*, 7453.
83. P. M. Budd, E. S. Elabas, B. S. Ghanem, S. Makhseed, N. B. McKeown, K. J. Msayib, C. E. Tattershall, D. Wang, *Adv. Mater.* **2004**, *16*, 456.
84. W. S. Drisdell, R. Poloni, T. M. McDonald, T. A. Pascal, L. F. Wan, C. D. Pemmaraju, B. Vlaisavljevich, S. O. Odoh, J. B. Neaton, J. R. Long, D. Prendergast, J. B. Kortright, *Phys. Chem. Chem. Phys.* **2015**, *17*, 21448.
85. H. B. Park, C. H. Jung, Y. M. Lee, A. J. Hill, S. J. Pas, S. T. Mudie, E. Van Wagner, B. D. Freeman, D. J. Cookson, *Science* **2007**, *318*, 254.
86. Z.-A. Qiao, S.-H. Chai, K. Nelson, Z. Bi, J. Chen, S. M. Mahurin, X. Zhu, S. Dai, *Nat. Commun.* **2014**, *5*, 3705.
87. L. M. Robeson, *J. Membr. Sci.* **2008**, *320*, 390.
88. L. Setiawan, R. Wang, K. Li, A. G. Fane, *J. Membr. Sci.* **2011**, *369*, 196.
89. a) K. K. Tanabe, S. M. Cohen, *Chem. Soc. Rev.* **2011**, *40*, 498; b) M. Dincă, J. R. Long, *J. Am. Chem. Soc.* **2007**, *129*, 11172.
90. S. Wang, X. Li, H. Wu, Z. Tian, Q. Xin, G. He, D. Peng, S. Chen, Y. Yin, Z. Jiang, M. D. Guiver, *Energy Environ. Sci.* **2016**, *9*, 1863.
91. D. T. Hallinan, Jr., N. P. Balsara, *Annu. Rev. Mater. Res.* **2013**, *43*, 503.
92. C. Zhang, R. P. Lively, K. Zhang, J. R. Johnson, O. Karvan, W. J. Koros, *J. Phys. Chem. Lett.* **2012**, *3*, 2130.
93. Y. Pan, T. Li, G. Lestari, Z. Lai, *J. Membr. Sci.* **2012**, *390–391*, 93.
94. V. Bon, N. Kavoosi, I. Senkovska, P. Muller, J. Schaber, D. Wallacher, D. M. Tobbens, U. Mueller, S. Kaskel, *Dalton Trans.* **2016**, *45*, 4407.
95. W. Ogieglo, B. Ghanem, X. Ma, I. Pinnau, M. Wessling, *J. Phys. Chem. B* **2016**, *120*, 10403.
96. C. Li, A. L. Ward, S. E. Doris, T. A. Pascal, D. Prendergast, B. A. Helms, *Nano Lett.* **2015**, *15*, 5724.
97. S. E. Doris, A. L. Ward, A. Baskin, P. D. Frischmann, N. Gavvalapalli, E. Chénard, C. S. Sevov, D. Prendergast, J. S. Moore, B. A. Helms, *Angew. Chem. Int. Ed.* **2017**, *56*, 1595.
98. J. G. Wijmans, R. W. Baker, *J. Membr. Sci.* **1995**, *107*, 1.
99. a) B. Smit, J. A. Reimer, C. M. Oldenburg, I. C. Bourg, *Introduction to Carbon Capture and Sequestration*, Vol. 1, Imperial College Press, London, 2014.
100. I. Pinnau, *J. Membr. Sci.* **1996**, *116*, 199; b) A. W. Thornton, J. M. Hill, A. J. Hill, in *Membrane Gas Separation*, John Wiley & Sons, Ltd, 2010, 85; c) E. L. Cussler, *Diffusion: Mass Transfer in Fluid Systems*, Cambridge University Press, Cambridge, United Kingdom **2009**, p. 190.
101. R. Srinivasan, S. R. Auvil, P. M. Burban, *J. Membr. Sci.* **1994**, *86*, 67.
102. S. A. Reinecke, B. E. Sleep, *Water Resour. Res.* **2002**, *38*, 16.
103. R. Ash, R. Barrer, C. Pope, "Flow of Adsorbable Gases and Vapours in a Microporous Medium. I. Single Sorbates", presented at *Proceedings of the Royal Society of London A: Mathematical, Physical and Engineering Sciences*, 1963.

104. R. Ash, R. Barrer, C. Pope, "Flow of Adsorbable Gases and Vapours in a Microporous Medium. Ii. Binary Mixtures", presented at *Proceedings of the Royal Society of London A: Mathematical, Physical and Engineering Sciences*, 1963.
105. K. L. Gleason, Z. P. Smith, Q. Liu, D. R. Paul, B. D. Freeman, *J. Membr. Sci.* **2015**, *475*, 204.
106. Q.-H. Wei, C. Bechinger, P. Leiderer, *Science* **2000**, *287*, 625.
107. E. Tajkhorshid, P. Nollert, M. Ø. Jensen, L. J. Miercke, J. O'Connell, R. M. Stroud, K. Schulten, *Science* **2002**, *296*, 525.
108. a) A. Striolo, *Nano Lett.* **2006**, *6*, 633; b) A. Berezhkovskii, G. Hummer, *Phys. Rev. Lett.* **2002**, *89*, 064503; c) A. Das, S. Jayanthi, H. S. M. V. Deepak, K. V. Ramanathan, A. Kumar, C. Dasgupta, A. K. Sood, *ACS Nano* **2010**, *4*, 1687.
109. a) V. Kukla, J. Kornatowski, D. Demuth, I. Girnus, *Science* **1996**, *272*, 702; b) J. Kärger, in *Adsorption and Diffusion*, (Eds: H. G. Karge, J. Weitkamp), Springer Berlin Heidelberg, Berlin, Heidelberg, 2008, 329.
110. P. Grathwohl, *Diffusion in Natural Porous Media: Contaminant Transport, Sorption/Desorption and Dissolution Kinetics*, Springer Science, New York, 1998.
111. E. P. Barrett, L. G. Joyner, P. P. Halenda, *J. Am. Chem. Soc.* **1951**, *73*, 373.
112. S. Eslava, M. R. Baklanov, C. E. A. Kirschhock, F. Iacopi, S. Aldea, K. Maex, J. A. Martens, *Langmuir* **2007**, *23*, 12811.
113. J. R. Izzo, A. S. Joshi, K. N. Grew, W. K. S. Chiu, A. Tkachuk, S. H. Wang, W. Yun, *J. Electrochem. Soc.* **2008**, *155*, B504.
114. W. R. Vieth, J. M. Howell, J. H. Hsieh, *J. Membr. Sci.* **1976**, *1*, 177.
115. G. K. Fleming, W. J. Koros, *Macromolecules* **1986**, *19*, 2285.
116. W. J. Koros, S. K. Burgess, Z. Chen, in *Encyclopedia of Polymer Science and Technology*, John Wiley & Sons, Inc., Hoboken, New Jersey, 2015, 1.
117. I. C. Sanchez, R. H. Lacombe, *Macromolecules* **1978**, *11*, 1145.
118. F. Doghieri, G. C. Sarti, *Macromolecules* **1996**, *29*, 7885.
119. P. M. Budd, N. B. McKeown, D. Fritsch, *J. Mater. Chem.* **2005**, *15*, 1977.
120. W. J. Koros, D. R. Paul, *J. Polym. Sci. Polym. Phys. Ed.* **1978**, *16*, 1947.
121. T. C. Merkel, V. Bondar, K. Nagai, B. D. Freeman, *J. Polym. Sci. Part B: Polym. Phys.* **2000**, *38*, 273.
122. a) Z. P. Smith, R. R. Tiwari, T. M. Murphy, D. F. Sanders, K. L. Gleason, D. R. Paul, B. D. Freeman, *Polymer* **2013**, *54*, 3026; b) P. Li, T. Chung, D. Paul, *J. Membr. Sci.* **2014**, *450*, 380.
123. S. Kim, H. J. Jo, Y. M. Lee, *J. Membr. Sci.* **2013**, *441*, 1.
124. Z. P. Smith, D. F. Sanders, C. P. Ribeiro Jr, R. Guo, B. D. Freeman, D. R. Paul, J. E. McGrath, S. Swinnea, *J. Membr. Sci.* **2012**, *416*, 558.
125. P. Li, T. S. Chung, D. R. Paul, *J. Membr. Sci.* **2013**, *432*, 50.
126. P. Bernardo, E. Drioli, G. Golemme, *Ind. Eng. Chem. Res.* **2009**, *48*, 4638.
127. H. B. Park, S. H. Han, C. H. Jung, Y. M. Lee, A. J. Hill, *J. Membr. Sci.* **2010**, *359*, 11.
128. W. Koros, D. Paul, G. Huvard, *Polymer* **1979**, *20*, 956.
129. D. W. Breck, in *Zeolite Molecular Sieves: Structure, Chemistry, and Use*, John Wiley & Sons, New York, NY, 1973, 636.
130. T. C. Merkel, V. I. Bondar, K. Nagai, B. D. Freeman, I. Pinnau, *J. Polym. Sci. Part B: Polym. Phys.* **2000**, *38*, 415.
131. P. Pandey, *Prog. Polym. Sci.* **2001**, *26*, 853.

132. K. Tanaka, H. Kita, M. Okano, K.-i. Okamoto, *Polymer* **1992**, *33*, 585.
133. H. Eyring, *J. Chem. Phys.* **1936**, *4*, 283.
134. M. H. Cohen, D. Turnbull, *J. Chem. Phys.* **1959**, *31*, 1164.
135. H. Fujita, in *Fortschritte Der Hochpolymeren-Forschung*, Springer Berlin Heidelberg, Berlin, Heidelberg, 1961, 1.
136. a) A. Bondi, *Physical Properties of Molecular Crystals, Liquids and Glasses*, John Wiley & Sons, Inc., New York, London, Sydney, 1968; b) A. Bondi, *J. Phys. Chem.* **1964**, *68*, 441; c) D. W. Van Krevelen, *Properties of Polymers: Their Correlation with Chemical Structure, Third Edition*, Elsevier, Amsterdam, 1997; d) J. Y. Park, D. R. Paul, *J. Membr. Sci.* **1997**, *125*, 23; e) N. R. Horn, *J. Membr. Sci.* **2016**, *518*, 289.
137. Y. Jean, P. Mallon, D. Schrader, *Principles and Applications of Positron & Positronium Chemistry*, World Scientific, Singapore, 2003.
138. R. Barrer, E. K. Rideal, *Trans. Faraday Soc.* **1939**, *35*, 644.
139. P. Meares, *J. Am. Chem. Soc.* **1954**, *76*, 3415.
140. L. M. Robeson, *J. Membr. Sci.* **1991**, *62*, 165.
141. a) B. D. Freeman, *Macromolecules* **1999**, *32*, 375; b) A. Y. Alentiev, Y. P. Yampolskii, *J. Membr. Sci.* **2000**, *165*, 201.
142. J. Su, H. Guo, *J. Phys. Chem. B* **2012**, *116*, 5925.
143. Z. Qin, M. J. Buehler, *Nano Lett.* **2015**, *15*, 3939.
144. a) E. Tocci, L. De Lorenzo, P. Bernardo, G. Clarizia, F. Bazzarelli, N. B. McKeown, M. Carta, R. Malpass-Evans, K. Friess, K. Pilnáček, M. Lanč, Y. P. Yampolskii, L. Strarannikova, V. Shantarovich, M. Mauri, J. C. Jansen, *Macromolecules* **2014**, *47*, 7900; b) I. Rose, M. Carta, R. Malpass-Evans, M.-C. Ferrari, P. Bernardo, G. Clarizia, J. C. Jansen, N. B. McKeown, *ACS Macro Lett.* **2015**, *4*, 912; c) M. Carta, P. Bernardo, G. Clarizia, J. C. Jansen, N. B. McKeown, *Macromolecules* **2014**, *47*, 8320.
145. a) P. M. Budd, K. J. Msayib, C. E. Tattershall, B. S. Ghanem, K. J. Reynolds, N. B. McKeown, D. Fritsch, *J. Membr. Sci.* **2005**, *251*, 263; b) B. S. Ghanem, N. B. McKeown, P. M. Budd, D. Fritsch, *Macromolecules* **2008**, *41*, 1640.
146. N. Du, H. B. Park, G. P. Robertson, M. M. Dal-Cin, T. Visser, L. Scoles, M. D. Guiver, *Nat. Mater.* **2011**, *10*, 372.
147. M. Carta, R. Malpass-Evans, M. Croad, Y. Rogan, J. C. Jansen, P. Bernardo, F. Bazzarelli, N. B. McKeown, *Science* **2013**, *339*, 303.
148. P. Budd, N. McKeown, B. Ghanem, K. Msayib, D. Fritsch, L. Starannikova, N. Belov, O. Sanfirova, Y. Yampolskii, V. Shantarovich, *J. Membr. Sci.* **2008**, *325*, 851.
149. S. Kim, Y. M. Lee, *Prog. Polym. Sci.* **2015**, *43*, 1.
150. N. Du, H. B. Park, M. M. Dal-Cin, M. D. Guiver, *Energy Environ. Sci.* **2012**, *5*, 7306.
151. Z. P. Smith, K. Czenkusch, S. Wi, K. L. Gleason, G. Hernández, C. M. Doherty, K. Konstas, T. J. Bastow, C. Álvarez, A. J. Hill, A. E. Lozano, D. R. Paul, B. D. Freeman, *Polymer* **2014**, *55*, 6649.
152. S. H. Han, N. Misdan, S. Kim, C. M. Doherty, A. J. Hill, Y. M. Lee, *Macromolecules* **2010**, *43*, 7657.
153. a) D. F. Sanders, R. Guo, Z. P. Smith, Q. Liu, K. A. Stevens, J. E. McGrath, D. R. Paul, B. D. Freeman, *Polymer* **2014**, *55*, 1636; b) D. F. Sanders, R. Guo, Z. P. Smith, K. A. Stevens, Q. Liu, J. E. McGrath, D. R. Paul, B. D. Freeman, *J. Membr. Sci.* **2014**, *463*, 73.
154. R. Guo, D. F. Sanders, Z. P. Smith, B. D. Freeman, D. R. Paul, J. E. McGrath, *J. Mater. Chem. A* **2013**, *1*, 262.

155. Z. P. Smith, G. Hernández, K. L. Gleason, A. Anand, C. M. Doherty, K. Konstas, C. Alvarez, A. J. Hill, A. E. Lozano, D. R. Paul, B. D. Freeman, *J. Membr. Sci.* **2015**, *493*, 766.
156. a) S. Kim, S. H. Han, Y. M. Lee, *J. Membr. Sci.* **2012**, *403*, 169; b) K. T. Woo, J. Lee, G. Dong, J. S. Kim, Y. S. Do, W.-S. Hung, K.-R. Lee, G. Barbieri, E. Drioli, Y. M. Lee, *J. Membr. Sci.* **2015**, *490*, 129.
157. Y. Jiang, F. T. Willmore, D. F. Sanders, Z. P. Smith, C. P. Ribeiro, C. M. Doherty, A. Thornton, A. J. Hill, B. D. Freeman, I. C. Sanchez, *Polymer* **2011**, *52*, 2244.
158. J. E. Bachman, Z. P. Smith, T. Li, T. Xu, J. R. Long, *Nat. Mater.* **2016**, *15*, 845.
159. a) T.-H. Bae, J. S. Lee, W. Qiu, W. J. Koros, C. W. Jones, S. Nair, *Angew. Chem. Int. Ed.* **2010**, *49*, 9863; b) A. Car, C. Stropnik, K. V. Peinemann, *Desalination* **2006**, *200*, 424; c) J. Hu, H. Cai, H. Ren, Y. Wei, Z. Xu, H. Liu, Y. Hu, *Ind. Eng. Chem. Res.* **2010**, *49*, 12605; d) E. V. Perez, K. J. Balkus, J. P. Ferraris, I. H. Musselman, *J. Membr. Sci.* **2009**, *328*, 165; e) B. Seoane, J. Coronas, I. Gascon, M. E. Benavides, O. Karvan, J. Caro, F. Kapteijn, J. Gascon, *Chem. Soc. Rev.* **2015**, *44*, 2421; f) T. Yang, Y. Xiao, T.-S. Chung, *Energy Environ. Sci.* **2011**, *4*, 4171; g) B. Zornoza, C. Tellez, J. Coronas, J. Gascon, F. Kapteijn, *Microporous Mesoporous Mater.* **2013**, *166*, 67.
160. T.-H. Bae, J. R. Long, *Energy Environ. Sci.* **2013**, *6*, 3565.
161. T. Rodenas, I. Luz, G. Prieto, B. Seoane, H. Miro, A. Corma, F. Kapteijn, F. X. Llabrés i Xamena, J. Gascon, *Nat. Mater.* **2015**, *14*, 48.
162. C. Zhang, Y. Dai, J. R. Johnson, O. Karvan, W. J. Koros, *J. Membr. Sci.* **2012**, *389*, 34.
163. J. E. Bachman, J. R. Long, *Energy Environ. Sci.* **2016**, *9*, 2031.
164. a) J. Ahn, W.-J. Chung, I. Pinnau, M. D. Guiver, *J. Membr. Sci.* **2008**, *314*, 123; b) J. Ahn, W.-J. Chung, I. Pinnau, J. Song, N. Du, G. P. Robertson, M. D. Guiver, *J. Membr. Sci.* **2010**, *346*, 280; c) C. J. Cornelius, E. Marand, *J. Membr. Sci.* **2002**, *202*, 97; d) N. C. Su, Z. P. Smith, B. D. Freeman, J. J. Urban, *Chem. Mater.* **2015**, *27*, 2421; e) R. Xing, W. S. W. Ho, *J. Membr. Sci.* **2011**, *367*, 91.
165. W. A. W. Rafizah, A. F. Ismail, *J. Membr. Sci.* **2008**, *307*, 53.
166. D. Q. Vu, W. J. Koros, S. J. Miller, *J. Membr. Sci.* **2003**, *211*, 311.
167. a) A. F. Ismail, P. S. Goh, S. M. Sanip, M. Aziz, *Sep. Purif. Technol.* **2009**, *70*, 12; b) S. Kim, T. W. Pechar, E. Marand, *Desalination* **2006**, *192*, 330.
168. J. Liu, T.-B. Bae, W. Qiu, S. Husain, S. Nair, C. W. Jones, R. R. Chance, W. J. Koros, *J. Membr. Sci.* **2009**, *343*, 157.
169. Y. Zhang, K. J. Balkus, I. H. Musselman, J. P. Ferraris, *J. Membr. Sci.* **2008**, *325*, 28.
170. T. H. Nguyen, H. Gong, S. S. Lee, T.-H. Bae, *ChemPhysChem* **2016**, *17*, 3165.
171. J. Ploegmakers, S. Japip, K. Nijmeijer, *J. Membr. Sci.* **2013**, *428*, 445.
172. a) W. L. Queen, M. R. Hudson, E. D. Bloch, J. A. Mason, M. I. Gonzalez, J. S. Lee, D. Gygi, J. D. Howe, K. Lee, T. A. Darwish, M. James, V. K. Peterson, S. J. Teat, B. Smit, J. B. Neaton, J. R. Long, C. M. Brown, *Chem. Sci.* **2014**, *5*, 4701; b) E. D. Bloch, W. L. Queen, R. Krishna, J. M. Zadrozny, C. M. Brown, J. R. Long, *Science* **2012**, *335*, 1606.

Chapter 2

Thermally Rearranged Polymer Membranes Containing Tröger's Base Units Have Exceptional Performance for Air Separations

2.1 Introduction

Mass transport across polymer membranes is mediated by segmental chain motion of the polymer backbone.[1] Consequently, increased backbone rigidity improves diffusive selectivity, albeit at the expense of permeability. To enhance permeability as well as selectivity, measures to increase inter-chain spacing are often required. Within this framework of polymer design, permeability-selectivity tradeoffs manifest as upper bounds to membrane performance, as articulated by Robeson.[2,3] Upper-bound polymers for membranes, such as polymers of intrinsic microporosity (PIMs) and TR polymers, are thus highly contorted, inefficiently packed, and glassy.[4] To advance beyond these limits, new polymer backbones are needed that incorporate more rigid contortion sites that introduce free-volume elements in the membrane and slow segmental chain motion for higher diffusive selectivity, while also incorporating a means to increase inter-chain spacing—e.g., via controlled solid-state chemical rearrangements—to further enhance membrane permeability.

In this chapter, I show that rationally designed, conformationally rigid monomers, when incorporated into TR polybenzoxazole membranes, yield highly permeable, size-selective micropore networks with exceptional discrimination between gases with small diffusion correlation diameters, including dioxygen and dinitrogen. Key to the success of this approach is the implementation of Tröger's Base (TB) as the site of contortion along the TR polymer backbone (Figure 2.1). Perturbations to the dihedral angle of TB incur substantially higher energetic penalties than spiro-centers used in conventional TR polymers;[5] as a result, solid-state decarboxylation of *ortho*-functional polyimides containing these inflexible moieties yields rigid-rod polybenzoxazole membranes[6] with small pores that enhance permeability and, for multiple important gas pairs, selectivity. I access this new class of TR polymers through *ortho*-acetate functionalized Tröger's base polyimide precursors: e.g., 6FDA-AcTB **1**, ODPA-AcTB **2**, and BPADA-AcTB **3** (Scheme 2.1). Notably, thermal rearrangement of 6FDA-AcTB **1** to 6FDA-TR-TB **4** produces membranes with a unique pore architecture that endows them with an O_2 permeability of 108 Barrer and O_2/N_2 selectivity of 8.9, placing the performance above the 2015 air-separation upper bound and highlighting new opportunities in membrane design with this strategy.[7]

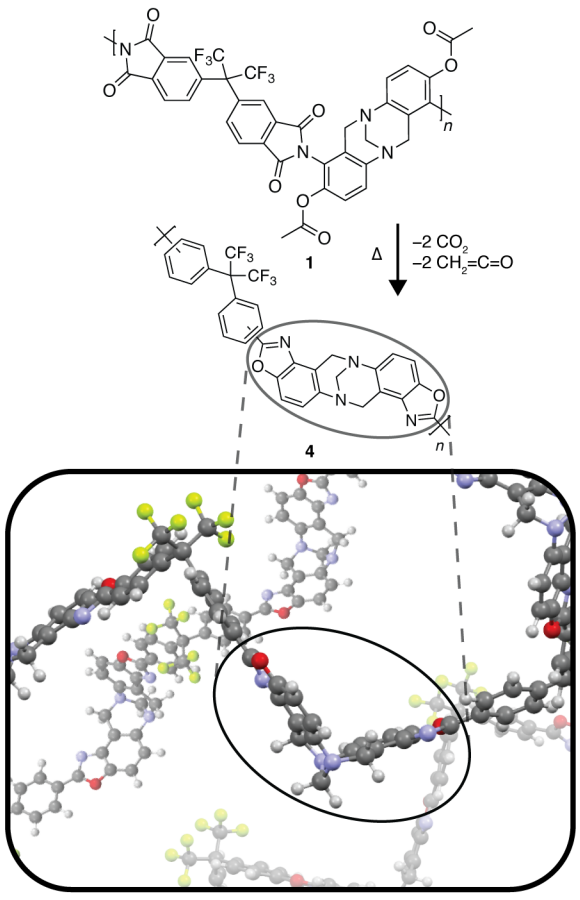

Figure 2.1 Thermal rearrangement reaction leading to a polybenzoxazole with Tröger's base sub-units (top) and molecular model of 6FDA-TR-TB **4** (bottom). C gray, N blue, F yellow, O red.

My approach provides distinct advantages over state-of-the-art membrane materials for air separations. Traditional glassy polyimides (PIs) fall below the Robeson upper bound, and systems incorporating these membranes are

permeability-limited for their range of selectivities.[7,8] Solution processable microporous polymers, including PIMs[5,9] and PIM-PIs,[10] provide permeability gains over polyimides, albeit with little to no gains in selectivity; as such, their use in air separations comes with added system complexity and cost associated with low product recovery. Selectivity gains over PIMs with TR polymers are thus attractive for air separations, but commensurate permeability gains are needed to fully realize the separation potential of TR polymer membranes.[8] In particular, what is lacking is a dedicated means of rigidifying the membrane while also increasing inter-chain spacing, a method uniquely implemented here.

2.2 Synthesis of *Ortho*-Acetate TB Polyimides

To access conformationally rigid TR polymer membranes, I synthesized *ortho*-acetate precursor polyimides (AcTBs) that incorporate bicyclic TB units such that the thermal rearrangement yields a benzoxazole on each aromatic ring of the foundational architectural motif. AcTBs were synthesized through the condensation polymerization of *ortho*-hydroxy Tröger's base diamine **6** with a desired dianhydride (Scheme 2.1).

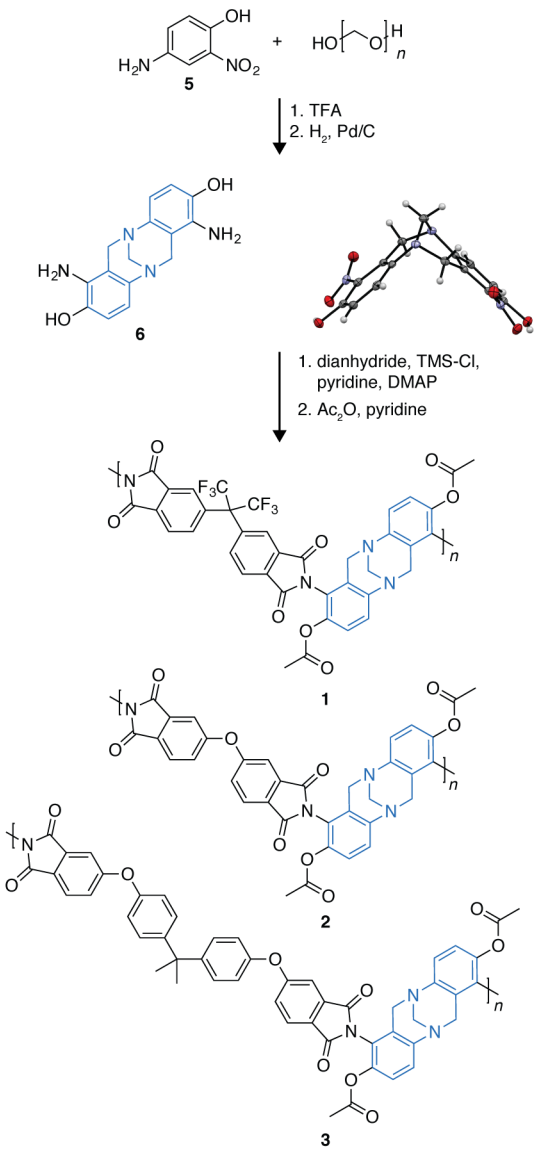

Scheme 2.1 Synthesis of *ortho*-acetate polyimides 6FDA-AcTB **1**, ODPA-AcTB **2**, and BPADA-AcTB **3**. The single-crystal XRD structure of the dinitro precursor to diamine **6** demonstrates the contortion of the Tröger's base unit.

I synthesized the diamine monomer through the reaction of 4-amino-2-nitrophenol **5** with paraformaldehyde followed by hydrogenation of the nitro groups. Single-crystal X-ray diffraction revealed that the amine substituents are regiospecifically *ortho* to the Tröger's base bridge, flanked on both sides by methylene and hydroxyl groups. Steric hindrance at the amine potentially limits access to high molecular weight polymers, but I overcame this limitation by silylating the amine prior to polymerization using chlorotrimethylsilane (TMS-Cl), 4-(dimethylamino)pyridine (DMAP) as a silylation catalyst, and pyridine as an acid scavenger.[11] Importantly, silylation increases electron density on the amine, activating the monomer for polymerization.[12] After silylation, the dianhydride monomer was introduced into the reaction mixture to begin polymerization. Dehydration of the resulting polymer with an excess of acetic anhydride yielded the polyimide, whose *ortho*-hydroxy groups were concomitantly acetylated. The resulting AcTB polymers possessed high molecular weights (Figure 2.2) and excellent solubility for membrane casting.

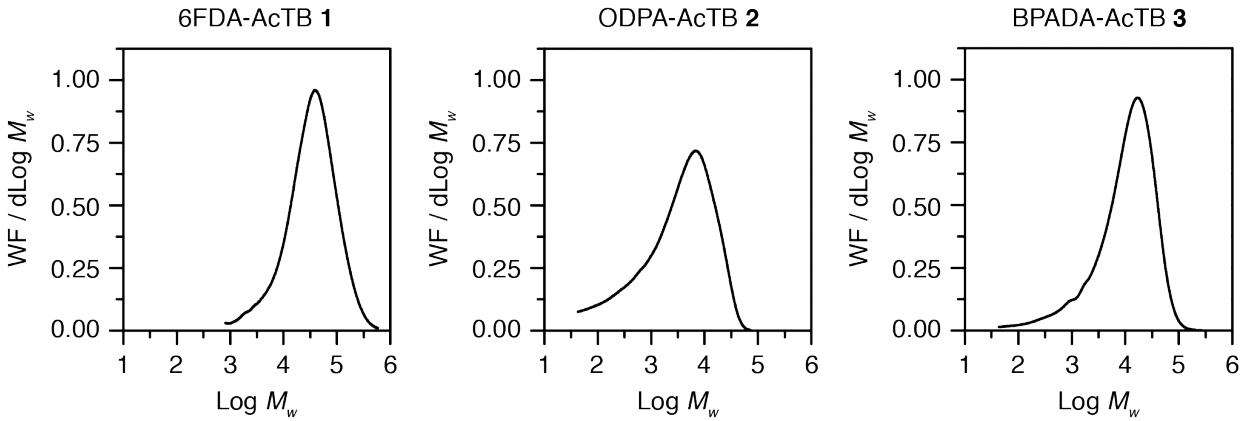

Figure 2.2 Molecular weight distributions of polyimides 6FDA-AcTB **1**, ODPA-AcTB **2**, and BPADA-AcTB **3**.

2.3 Controlling the Physical Properties of *Ortho*-Acetate Polyimides Through Backbone Chemistry

To assess the scope of this polymerization scheme and understand architectural outcomes, AcTB polymers **1–3** were synthesized from three different dianhydride monomers: 4,4′-(hexafluoroisopropylidene)diphthalic anhydride (6FDA), 4,4′-oxydiphthalic anhydride (ODPA), and 4,4′-(4,4′-isopropylidenediphenoxy)*bis*(phthalic anhydride) (BPADA). No glass transition was observed up to 325 °C for 6FDA-AcTB **1** or ODPA-AcTB **2**, but a clear transition was recorded at T_g = 294 °C for BPADA-AcTB **3** (Figure 2.3). The BET surface area, as measured by nitrogen gas adsorption at 77 K, dropped precipitously with the removal of bulky trifluoromethyl substituents (172 $m^2\ g^{-1}$ for 6FDA-AcTB **1** *vs.* 51 $m^2\ g^{-1}$ for ODPA-AcTB **2**, Figure 2.4), and when excess flexibility was introduced in BPADA-AcTB **3**, no N_2 uptake was observed. These results demonstrate that the physical properties and pore networks of AcTB polymers (and films) are tunable through chemical design of the dianhydride. Further, the highly glassy and porous nature of 6FDA-AcTB **1** suggests it would be the most promising membrane material for air separations; as such, it was further investigated through the full TR reaction pathway.

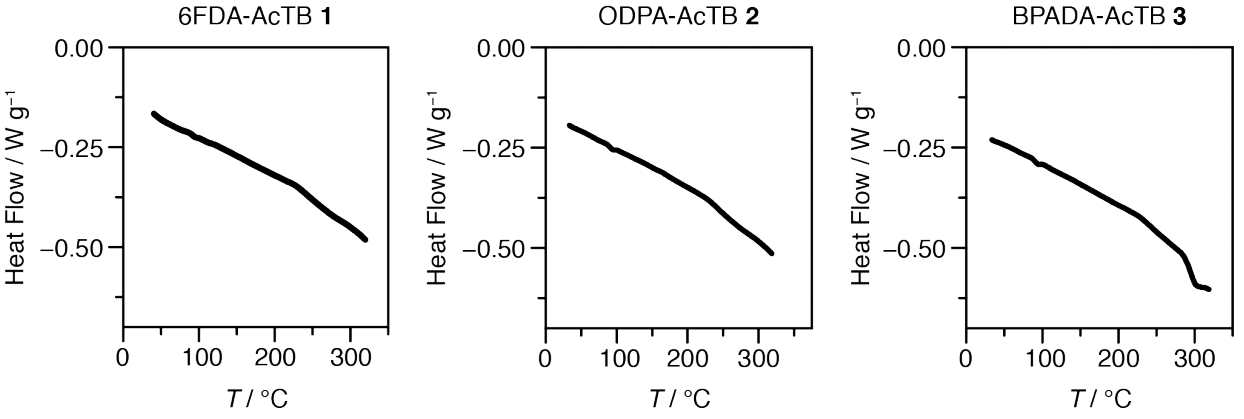

Figure 2.3 DSC plots of polyimides 6FDA-AcTB **1**, ODPA-AcTB **2**, and BPADA-AcTB **3**. Only BPADA-AcTB **3** shows a T_g (294 °C).

2.4 Characterizing the Thermal Rearrangement to TR-TB Polymer Membranes

TR-TB polymer membranes accessed through the solid-state decarboxylation of AcTB polyimide films feature the rigidity of the polybenzoxazole structure, enhanced porosity from polymer chain reconfiguration, and complementary intra-chain rigidity and frustrated inter-chain packing from the TB sub-unit. To understand the thermal reaction pathway through which 6FDA-AcTB **1** proceeds, I employed thermo-gravimetric analysis coupled with mass-spectrometry (TGA-MS). During thermal rearrangement, two mass loss events are expected: the first loss results from elimination of acetate groups, producing ketene and leaving behind a hydroxy group;[13] carbon dioxide is then driven off during rearrangement to the benzoxazole. Figure 2.5a shows total mass loss and relative intensities of the ketene and carbon dioxide mass peaks as a function of temperature. Acetate loss begins around 300 °C and peaks just below 400 °C. As the thermal rearrangement reactions can be sequential, 400 °C is considered the lower-bound temperature for thermal rearrangement in this system. Carbon dioxide evolution is marked by a local maximum around 450 °C, coinciding with a peak in the first derivative mass loss (Figure 2.5b), consistent with the proposed polybenzoxazole formation mechanism.

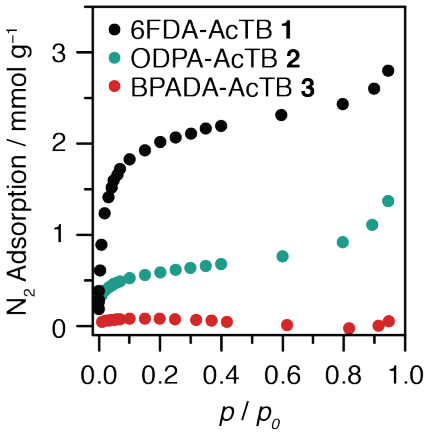

Figure 2.4 N_2 adsorption isotherms at 77 K of polyimides 6FDA-AcTB **1**, ODPA-AcTB **2**, and BPADA-AcTB **3**.

To maximize conversion to the benzoxazole while minimizing polymer backbone decomposition, care must be taken in developing thermal rearrangement protocols, which typically involve a high-temperature isothermal soak. Ideally, the experimental mass loss is

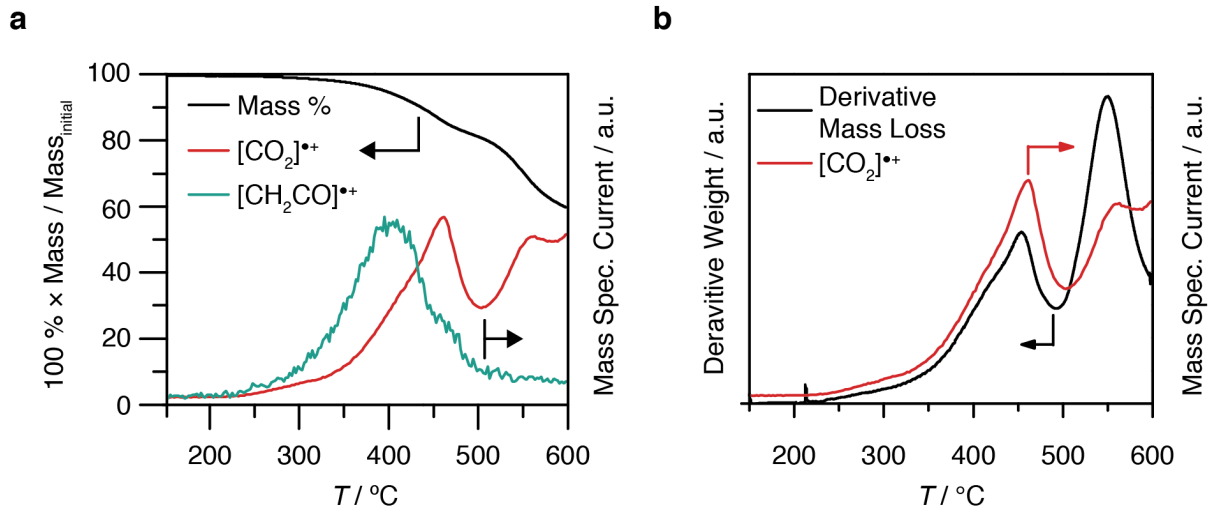

Figure 2.5 Thermal rearrangement reaction characterized by TGA-MS. a) TGA-MS of 6FDA-AcTB **1** heated to 600 °C at a ramp rate of 10 °C min^{-1}. b) The derivative weight loss of 6FDA-AcTB **1** compared to the mass spectrometer signal from CO_2 shows strong agreement, indicating that the first weight-loss event is consistent with benzoxazole formation.

equivalent to the theoretical value. Isothermal TGA experiments were used to monitor TR conversion at different soak temperatures. Films were heated at 5 °C min^{-1} to 300 °C under flowing argon and held at that temperature for 1 h to fully imidize the polymer and drive off any residual solvent. The films were then heated at 5 °C min^{-1} to a final soak temperature varying between 400–440 °C. The theoretical 22.2% mass loss for complete thermal rearrangement was reached in ~7 min at 440 °C, ~27 min at 420 °C, and ~94 min at 400 °C (Figure 2.6). Based on these findings, I adopted a final soak temperature of 420 °C for 30 min. Large-format membranes were thermally treated in a tube furnace under flowing argon. Thermally-treated films were insoluble in all solvents tested, as is common for TR polymers.[6]

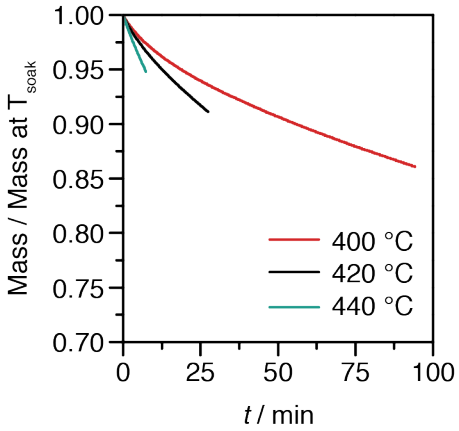

Figure 2.6 Isothermal TGA experiments used to determine thermal rearrangement conditions. Each trace is normalized to the mass when the final soak temperature was reached and cut off at the theoretical mass loss to benzoxazole formation.

2.5 The Effects of Thermal Rearrangement on Selective Gas Transport

To understand the influence of thermal treatment on analyte transport through AcTB polymer films, we measured the permeability of CO_2, O_2, N_2, and CH_4 through films of 6FDA-AcTB **1** and 6FDA-TR-TB **4**. For all four gases, permeability increases with thermal rearrangement, from 17 to 108 Barrer for O_2, 72 to 158 Barrer for CO_2, 3.9 to 12 Barrer for N_2, and 3.4 to 6.7 Barrer for CH_4. Smaller gases generally exhibit the greatest enhancements (Figure 2.7a). The less pronounced increase in CO_2 permeability, which is largely dictated by solubility, suggests that the observed enhancements are diffusivity-driven. The increase in O_2 permeability is most significant, improving both permeability and selectivity for O_2/N_2 separations and placing the membrane far above the 2008 upper bound[3] and slightly above the more recently suggested 2015 upper bound (Figure 2.7b).[7]

The chemical origins of these membrane performance enhancements were investigated spectroscopically. Carbon X-ray photoelectron spectroscopy (XPS) revealed that both 6FDA-AcTB **1** and 6FDA-TR-TB **4** have a broad peak near 284 eV, as well as a small peak at 293 eV from trifluoromethyl carbons (Figure 2.8a). Of note, the carbonyl carbon peak near 288 eV in the 6FDA-AcTB **1** spectrum is greatly diminished in the 6FDA-TR-TB **4** spectrum. This result suggests successful evolution of the acetate groups and reaction of the imide sites, as is expected during benzoxazole formation. Because overlapping signals in the large XPS features near 284 eV were difficult to deconvolute into meaningful components, FT-IR spectroscopy was used to further investigate the chemical evolution during thermal rearrangement (Figure 2.8b). The 6FDA-AcTB **1** spectrum contains peaks at 1774 cm^{-1} (carbonyl), 1730 cm^{-1} (carbonyl), and 1374 cm^{-1} (imide C–N) that are greatly diminished in the 6FDA-TR-TB **4** spectrum, consistent with the loss of carbonyl signal in the XPS. Furthermore, peaks at 1497 cm^{-1} and 1097 cm^{-1}, attributed to benzoxazole formation,[13] are evident in the 6FDA-TR-TB **4** spectrum. Together, this spectroscopic information supports near complete thermal rearrangement.

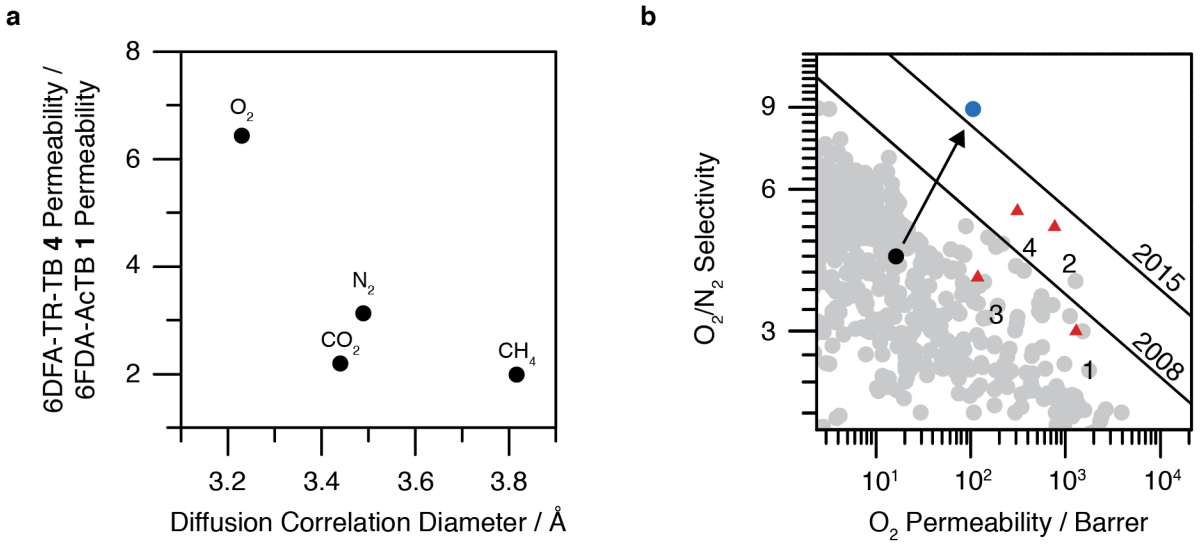

Figure 2.7 a) Permeability enhancements versus gas diffusion correlation diameter[14] from the thermal rearrangement of 6FDA-AcTB **1** to 6FDA-TR-TB **4**. b) 6FDA-AcTB 1 (black) and 6FDA-TR-TB 4 (blue) membrane performance at 1.9 atm and 35 °C plotted against the upper bound for air separations. Red triangles mark the performance of previously reported TR polymers: 1 cTR-450,[15] 2 tTR-450, 3 spiroTR-PBO-6F,[16] and 4 TR TDA1-APAF.[17] Gray circles represent polymer membranes reported in the literature.

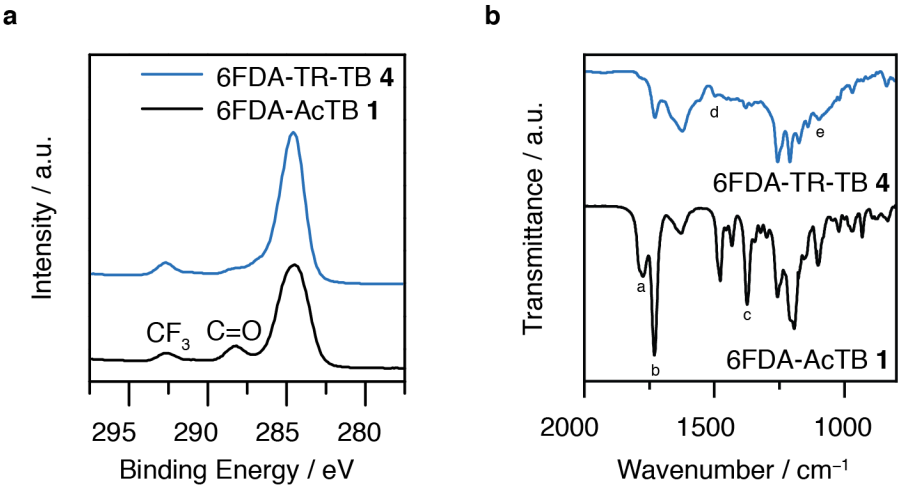

Figure 2.8 Chemical characterization of 6FDA-AcTB **1** and 6FDA-TR-TB **4**. a) Carbon XPS shows the diminution of the carbonyl peak at 288 eV. b) FT-IR analysis shows the disappearance of the carbonyl stretching (a, 1774 cm^{-1} and b, 1730 cm^{-1}) peaks and C–N stretching (c, 1374 cm^{-1}) upon thermal rearrangement. The 6FDA-TR-TB **4** spectrum has small peaks (d, 1497 cm^{-1} and e, 1097 cm^{-1}) attributed to benzoxazole formation.[13] For clarity, the traces are normalized to the C–F stretch at 1257 cm^{-1}.

2.6 Characterization of TR-TB Pore Architecture

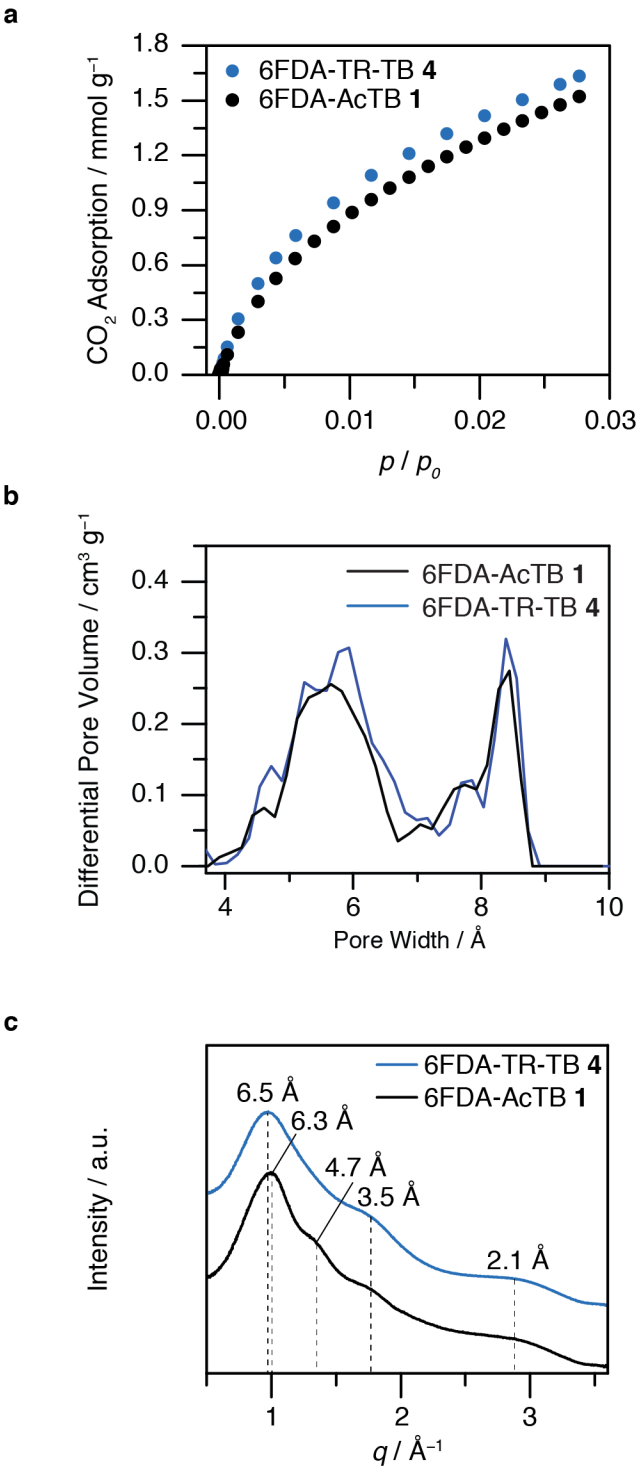

Figure 2.7 Characterization of the pore architecture evolution during thermal rearrangement. a) CO_2 adsorption isotherm at 273 K, b) nonlocal DFT pore size distribution, and c) WAXS patterns of 6FDA-AcTB **1** and 6FDA-TR-TB **4**.

While restricted intra-chain mobility arising from local chemical changes can account for some membrane performance attributes, global pore-network evolution during thermal rearrangement is also important in dictating transport outcomes. Carbon dioxide adsorption isotherms collected at 273 K show higher uptake in 6FDA-TR-TB **4** *vs.* 6FDA-AcTB **1**, consistent with the predicted porosity increase and the observed permeability increase with thermal rearrangement (Figure 2.9a). Nonlocal DFT pore-size distributions produced from these isotherms reveal significant ultramicroporosity (i.e., pores of diameter < 7 Å, Figure 2.9b). The isotherms and pore-size distributions were similar for both polymers, motivating further study of the pore networks with synchrotron wide-angle X-ray scattering (WAXS, Figure 2.9c). A small decrease in the peak position of the main scattering feature near 1 $Å^{-1}$ reflects an increase in average inter-chain *d*-spacing from 6.3 Å in 6FDA-AcTB **1** to 6.5 Å in 6FDA-TR-TB **4**. This increased inter-chain spacing is consistent with increased porosity and permeability. Notably, a shoulder feature in the 6FDA-AcTB **1** scattering pattern corresponding to 4.7 Å disappears from the 6FDA-TR-TB **4** scattering pattern, and the feature corresponding to 3.5 Å grows in relative intensity and broadness after thermal rearrangement.

These changes to the WAXS patterns with thermal rearrangement could signal the coalescence of pores into more uniform free-volume elements with spacing between the diameters of O_2 and N_2. Polymer segments too inflexible to exhibit segmental chain motion-dictated transport may be exhibiting a molecular sieving effect; such a shift in transport mechanism would explain the marked increase in O_2/N_2 selectivity despite more modest performance increases

in CO_2/CH_4 and CO_2/N_2 separations. High-q scattering features in porous polymer WAXS patterns, however, sometimes reflect distances between given repeat units rather than the space between chains.[18] Even if the scattering peaks arise from the positions of repeat units, the results still signal a shift to a more uniform distribution of occupied volume in the porous material. Overall, characterization of the TR polymer pore network suggests that an increase in pore size and total porosity is responsible for the enhanced permeability while the formation of immobile size-discriminating windows enhances size-selectivity for air separations.

2.7 Conclusions

The exceptional performance of 6FDA-TR-TB **4** membranes and the characterization of their pore network validates our design strategy of incorporating conformationally rigid units such as TB into a TR polybenzoxazole to produce highly selective membranes without sacrificing permeability. I propose that these membranes could be relevant in applications where inert gas production is needed in confined areas, such as backfilling fuel tanks on aircraft. I note that the permselectivity of TR-TB membranes could be further tuned through the chemical structure of the dianhydride residue, but the rational design of more conformationally rigid motifs is necessary to substantially advance TR polymer membranes. Strategies to this end will likely include the development of sterically-hindered polycyclic monomers, an approach that has seen recent success in advanced PIMs.[19] Leading-Edge materials genomics screens may be an effective tool in accelerating this discovery process.[20] The TR-TB platform reported here is an important first step and effective guidepost along this design trajectory.

2.8 Experimental Details

2.8.1 Materials

Acetic anhydride (98%), 4-(dimethylamino)pyridine (DMAP, ≥ 99%), Celite® 535, palladium on carbon (Pd/C, 10% *w/w*), paraformaldehyde, 4-amino-2-nitrophenol (97%), and trifluoroacetic acid (TFA, 99%) were obtained from Sigma Aldrich and used without further purification. Ethyl ether and potassium hydroxide were obtained from BDH; pyridine (≥ 99%) was obtained from Acros Organics; d_6-dimethyl sulfoxide (d_6-DMSO, 99.9 atom % D) was obtained from Cambridge Isotope Laboratories; methanol, ethyl acetate, and acetone (all HPLC grade) were obtained from EMD Millipore; *N,N*-dimethylformamide (DMF) was obtained from Fischer Scientific; chlorotrimethylsilane (TMS-Cl, ≥ 99.0%) was obtained from Fluka; reagent alcohol (absolute) was obtained from Macron; tetrahydrofuran (THF, HPLC grade) and hexanes (64% *n*-hexane) were obtained from OmniSolv; and hydrogen gas (4.5 grade) was obtained from Praxair. All were used without further purification. Potassium bromide (KBr) was obtained from International Crystal Labs and dried in a vacuum oven at 200 °C overnight prior to use. *N*-Methyl-2-pyrrolidone (NMP, anhydrous, 99.5%) used for polyimide synthesis was obtained from Sigma Aldrich and stored in a dry nitrogen atmosphere until use. 4,4′-Oxydiphthalic anhydride (ODPA, 97%) and 4,4′-(hexafluoroisopropylidene)diphthalic anhydride (6FDA, 99%) were obtained from Sigma Aldrich and were sublimed at 210 °C and 230 °C, respectively, in a CreaPhys DSU-05 vacuum sublimation system immediately prior to use. 4,4′-(4,4′-Isopropylidenediphenoxy)-bis(phthalic anhydride) (BPADA, 97%) was obtained from Sigma Aldrich and recrystallized from acetic anhydride.

2.8.2 Characterization Methods

^{1}H and ^{13}C NMR spectra were recorded on a Bruker Avance II 500 MHz NMR spectrometer. Chemical shifts are reported in δ (ppm) relative to the residual solvent peak (d_6-DMSO: 2.50 for ^{1}H; 39.51 for ^{13}C). Coupling constants (*J*) are expressed in Hertz (Hz). Splitting patterns are designated as s(singlet), d(doublet), t(triplet), q(quartet), dd(doublet of doublets), m(multiplet), and br(broad).

Elemental analyses were performed by the University of California, Berkeley College of Chemistry Microanalytical Facility using a Perkin Elmer 2400 Series II combustion analyzer. Single-crystal X-ray diffraction experiments were performed at the UC Berkeley CHEXRAY crystallographic facility. Measurements of 1,7-dinitro-6*H*,12*H*-5,11-methanodibenzo[*b*,*f*][1,5]diazocine-2,8-diol were performed on a Bruker APEX-II area detector using Cu Kα radiation (λ = 1.54178 Å). Crystals were kept at 100(2) K throughout collection. Data collection was performed with Bruker APEX2 software (v. 2014.11). Data refinement and reduction were performed with Bruker SAINT (V8.34A). All structures were solved with SHELXT.53. Structures were refined with SHELXL-2014. Molecular graphics were computed with Mercury 3.9. All non-hydrogen atoms were refined anisotropically, and hydrogen atoms were either included at the geometrically calculated positions and refined using a riding model or located as Q peaks in the Fourier difference map.

Size-Exclusion chromatograpy (SEC) was performed using DMF (containing 0.2% *w*/*v* lithium bromide) as the mobile phase. A home built system was used and consisted of a Shimadzu LC-20AD pump, Viscotek VE 3580 refractive index detector, and two mixed bed columns connected in series (Viscotek GMHHR-M). The system was operated at a temperature of 70 °C. Calibration on the system was performed with narrow poly(methyl methacrylate) standards (Polymer Laboratories) ranging from 620 g mol^{-1} to 910,500 g mol^{-1}.

Differential scanning calorimetry (DSC) data was recorded on a TA Instruments Q200 calorimeter. Samples were heated and cooled at a rate of 20 °C min^{-1}, and the second heating cycle is reported.

Films were formed from 2.5% (*w*/*v*) chloroform solutions, which were filtered through a glass acrodisc syringe filter (1 μm) and sonicated for 30 s prior to casting in polytetrafluoroethylene wells. The solvent was allowed to evaporate overnight to produce tan films 30 to 40 μm thick. Thermal rearrangement of large-format films was performed in a quartz tube under a 200 mL min^{-1} argon flow. Circular samples 1.6 cm in diameter were punched from larger 6FDA-AcTB **1** films and placed between two silicon wafers to prevent deformation at high temperature. Films were heated using a Lindberg Blue M tube furnace at a rate of 5 °C min^{-1} to 300 °C, held at that temperature for 1 h, heated to 420 °C at 5 °C min^{-1}, held at that temperature for 30 min, and then cooled to room temperature at a rate ≤ 5 °C min^{-1}. 6FDA-AcTB **1** films not subject to thermal rearrangement were heated to 150 °C for at least 12 h under vacuum to remove residual solvent prior to analysis.

Thermogravimetric analysis coupled with mass spectrometry (TGA-MS) was performed on a TA Instruments TGA5500 Discovery Series unit with a Pfeiffer Vacuum ThermoStar™ Mass Spec attachment. Samples were run in an argon atmosphere and heated at 10 °C min^{-1} to 600 °C with

a 1 h hold at 150 °C to remove residual solvent unless otherwise noted. Mass spectrometry currents are normalized for clarity.

Fourier-Transform infrared (FT-IR) spectra were recorded on a PerkinElmer Spectrum One spectrometer in transmission using KBr pellets. X-ray photoelectron spectroscopy (XPS) was performed in a Thermo Scientific™ K-AlphaPlus™ instrument equipped with monochromatic Al Kα radiation (1486.7 eV) as the excitation source. The X-ray analysis area for measurement was set at 200 x 400 μm (ellipse shape) and a flood gun was used for charge compensation. The pass energy was 200 eV for the wide (survey) spectra and 50 eV for the high-resolution regions (narrow spectra). The base pressure of the analysis chamber was less than ~1×10^{-9} mbar. The analysis chamber pressure was at 1×10^{-7} mbar during data acquisition. Data were collected and processed using the Thermo Scientific Avantage XPS software package.

Nitrogen adsorption isotherms were collected on a Micromeritics Tristar II 3020 gas sorption analyzer at 77 K. Carbon dioxide adsorption isotherms were collected on an Micromeritics ASAP 2020 gas sorption analyzer at 273 K. Nonlocal DFT pore-size distributions from carbon dioxide adsorption isotherms were calculated using software provided by micromeritics; medium regularization was applied to the pore-size distributions. Polyimide samples were degassed under vacuum at 100 – 150 °C overnight, and TR polymer samples were degassed at 200 °C overnight prior to analysis.

Wide-angle X-ray scattering (WAXS) data was collected in transmission under a helium atmosphere at the Advanced Light Source beamline 7.3.3 using a Pilatus 2M detector, a photon energy of 10 keV, and a sample-to-detector distance of 269 mm.

Gas permeation measurements were conducted using a custom-built constant volume-variable pressure apparatus. Membrane thickness was determined using a depth gauge. Samples were affixed to brass shim disks using impermeable epoxy glue. The remaining membrane area exposed to gas permeation was measured using a scanner. Samples were loaded into a stainless-steel filter holder (Millipore XX4502500). Before permeation tests, the system was held under static vacuum and the leak rate into the downstream volume was determined. This leak rate was then subtracted from permeation rates, and was always <1% of the permeation rate. Measurements were taken at p = 1.9 atm and T = 35 °C.

2.8.3 Synthetic Procedures

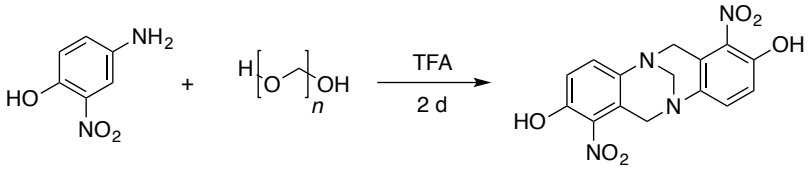

Synthesis of 1,7-dinitro-6*H*,12*H*-5,11-methanodibenzo[*b*,*f*][1,5]diazocine-2,8-diol
TFA (460 mL) was added to a 1 L round-bottomed flask charged with 4-amino-2-nitrophenol **5** (35.0 g, 227 mmol) at 0 °C with stirring. When a homogeneous solution was observed, paraformaldehyde (14.4 g, 480 mmol) was added in one portion. The solution was allowed to slowly warm to room temperature while stirring in the dark for 2 d. The reaction mixture was

precipitated into 5.0 M aqueous KOH (960 mL) solution over ice. The precipitate was collected by vacuum filtration and mixed with acetone, which was subsequently removed under vacuum to azeotropically remove residual TFA. The crude product was dissolved in minimal DMF and purified by flash chromatography using a hexanes-ethyl acetate mobile phase. A mixture of red-orange crystals and bright orange powder was collected (6.45 g, 16% yield). ^{1}H NMR (500 MHz, d_6-DMSO): δ 10.67 (s, 2H), 7.27 (d, J = 8.95 Hz, 2H), 6.92 (d, J = 8.95 Hz, 2H), 4.57 (d, J = 17.15 Hz, 2H), 4.23 (s, 2H), 3.92 (d, J = 17.15 Hz, 2H) ppm; ^{13}C NMR (125 MHz, d_6-DMSO): δ 146.0, 139.0, 137.0, 129.0, 121.0, 117.0, 65.2, 54.7 ppm; Anal. Calc'd for $C_{15}H_{12}N_4O_6$: C, 52.33; H, 3.51; N, 16.27; Found: C, 52.24; H, 3.45; N, 16.12.

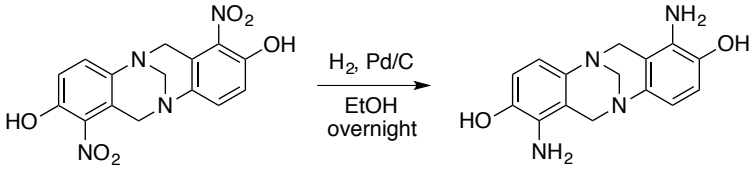

Synthesis of 1,7-diamino-6*H*,12*H*-5,11-methanodibenzo[*b*,*f*][1,5]diazocine-2,8-diol (6)
In a typical reaction, ethanol (90 mL) was added to a 500-mL round bottom flask charged with 1,7-dinitro-6*H*,12*H*-5,11-methanodibenzo[*b*,*f*][1,5]diazocine-2,8-diol (4.00 g, 11.6 mmol), forming an orange suspension. The flask was then sparged with dry nitrogen for 50 min with stirring. Pd/C (400 mg, 10%) was added as an ethanol slurry, bringing the total volume to 110 mL. The headspace was purged and backfilled with dry nitrogen three times then purged and backfilled with hydrogen three times. The reaction was left stirring under a hydrogen atmosphere overnight. DMF (50 mL) was added to the black/grey suspension to improve solubility and the mixture was vacuum filtered over Celite®. The Celite® pad was washed with DMF (200 mL), EtOH (200 mL), and THF (100 mL) until the filtrate was clear and solvent was removed *in vacuo*. The brown powder was dissolved in the minimum amount of NMP, filtered through a 0.2-μm PVDF syringe filter to remove any residual Celite®, and the product precipitated using diethyl ether. The precipitate was collected by vacuum filtration, washed with ether and hexanes, and left to dry under vacuum at 140 °C overnight, producing a light brown powder (2.87 g, 87% yield). ^{1}H NMR (500 MHz, d_6-DMSO): δ 8.67 (s, 2H), 6.48 (d, J = 8.35 Hz, 2H), 6.19 (d, J = 8.35 Hz, 2H), 4.17 (d, J = 16.65 Hz, 2H), 4.13 (s, 4H), 3.96 (s, 2H), 3.83 (d, J = 16.65 Hz, 2H) ppm; ^{13}C NMR (125 MHz, d_6-DMSO): δ 140.8, 139.2, 132.2, 113.7, 112.8, 112.2, 65.9, 55.8 ppm; Anal. Calc'd for $C_{15}H_{16}N_4O_2$: C, 63.37; H, 5.67; N, 19.71; Found: C, 63.26; H, 5.65; N, 19.50.

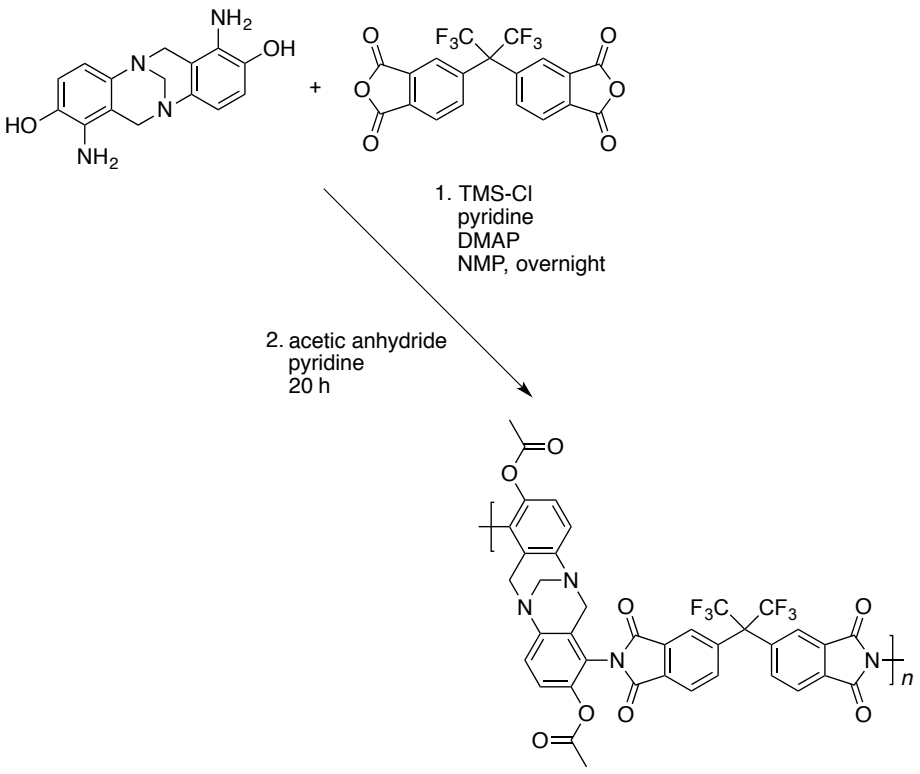

Synthesis of 6FDA-AcTB (1)

In a typical reaction, a 100 mL 2-neck round bottomed flask was charged with diamine **6** (800.9 mg, 2.817 mmol), and purged with nitrogen for 5 min. Anhydrous NMP (5 mL) was added and the reaction was allowed to stir under dry nitrogen for 1 h. The dark brown mixture was cooled to 0 °C before roughly 4 equivalents TMS-Cl (1.45 mL, 11.4 mmol) and pyridine (0.95 mL, 11.8 mmol) were added. The suspension became clear and was left to stir for 1 h. DMAP (138.2 mg, 1.13 mmol) was then added, and freshly sublimed 6FDA (1.2515 g, 2.817 mmol) followed in a single portion. Additional anhydrous NMP (5.5 mL) was added, the headspace was purged with nitrogen and the mixture was left to warm to room temperature with stirring overnight. Five equivalents acetic anhydride (1.33 mL, 14.1 mmol) and pyridine (1.14 mL, 14.1 mmol) were added to the cloudy reaction mixture, which cleared. The reaction was left to stir for 19 h, heated to 60 °C for 1 h, then crashed out in DI water. The precipitate was filtered, washed with MeOH, then dissolved in THF and precipitated in ether twice. The product was rinsed with hexanes and dried at 100 °C under high vacuum, producing a tan powder (1.94 g, 89% yield). ^{1}H NMR (500 MHz, d_6-DMSO): δ 8.22 (s, 2H), 8.00 (s, 2H), 7.88 (br, 2H), 7.26 (s, 2H), 7.20 (s, 2H), 4.38 (s, 4H), 4.20 (s, 2H), 2.01 (br, 6H) ppm; Anal. Calc'd for $C_{38}H_{22}F_6N_4O_8$: C, 58.77; H, 2.86; N, 7.21; Found: C, 57.17; H, 3.13; N, 7.03.

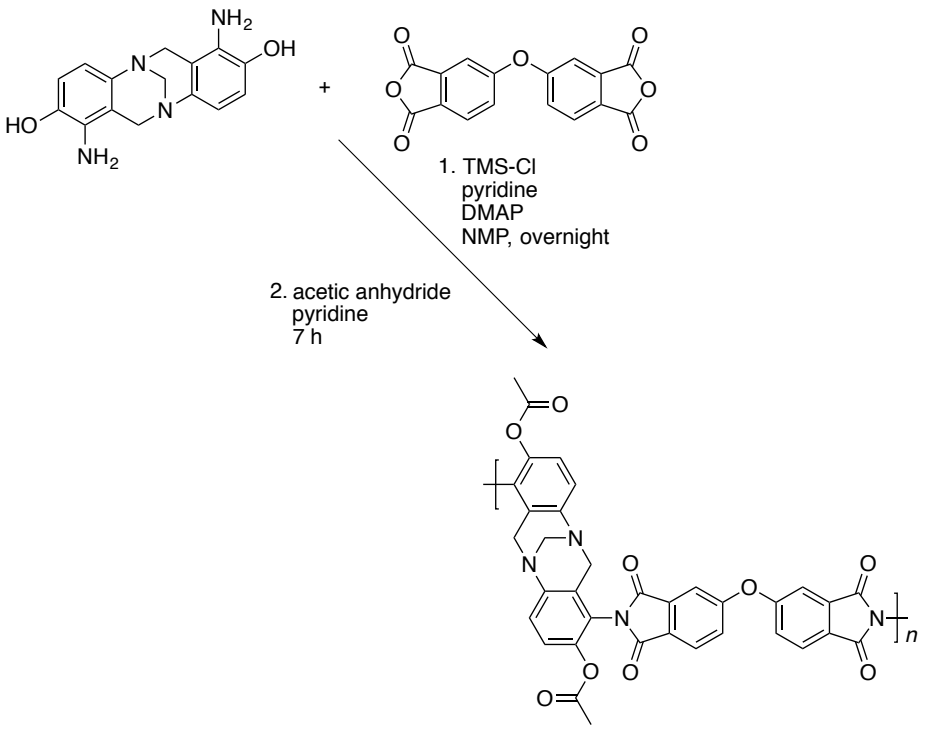

Synthesis of ODPA-AcTB (2)

A similar procedure was followed as in the synthesis of 6FDA-AcTB **1**. Diamine **6** (211.7 mg, 0.7446 mmol) was reacted with TMS-Cl (0.353 mL, 2.77 mmol), pyridine (0.225 mL, 2.79 mmol), DMAP (34.0 mg, 0.278 mmol) and ODPA (215.9 mg, 0.6960 mmol) in 1.5 mL NMP overnight. Pyridine (0.281 mL, 3.47 mmol) and acetic anhydride (0.329 mL, 3.48 mmol) were added, left to stir 6 h at room temperature and 1 h at 60 °C, and crashed out in DI water. Reprecipitations were carried out once with chloroform/methanol and once with DMF/ethyl acetate. The product was obtained as a dark brown powder (111 mg, 25% yield). ^{1}H NMR (500 MHz, d_6-DMSO): 8.12 (br, 2H), 7.75 – 7.70 (m, 4H), 7.28 (s, 2H), 7.19 (s, 2H), 4.40 (br, 2H), 4.28 (s, 2H), 4.20 (s, 2H), 2.00 (s, 6H) ppm; Anal. Calc'd for $C_{35}H_{22}N_4O_9$: C, 65.42; H, 3.45; N, 8.72; Found: C, 61.52; H, 3.84; N, 8.67.

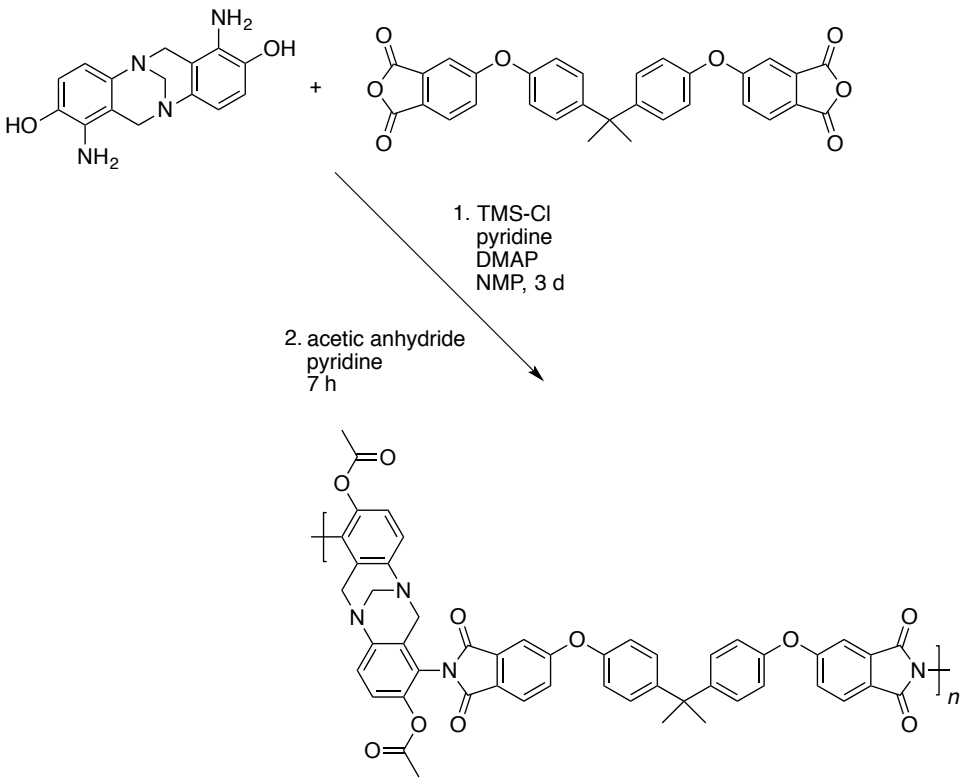

Synthesis of BPADA-AcTB (3)

A similar procedure was followed as in the synthesis of 6FDA-AcTB **1**. Diamine **6** (100.3 mg, 0.3528 mmol) was reacted with TMS-Cl (0.179 mL, 1.41 mmol), pyridine (0.114 mL, 1.42 mmol), DMAP (17.2 mg, 0.141 mmol) and BPADA (183.6 mg, 0.3527 mmol) in 1.4 mL NMP. After 3 d, pyridine (0.142 mL, 1.77 mmol) and acetic anhydride (0.166 mL, 1.76 mmol) were added, left to stir 6 h at room temperature and 1 h at 60 °C, and crashed out in DI water. Reprecipitations were carried out with chloroform/methanol. The product was obtained as a light tan powder (152 mg, 50% yield). ^{1}H NMR (500 MHz, d_6-DMSO): 8.00 (d, J = 7.95 Hz, 2H), 7.45 – 7.36 (m, 8H), 7.25 (d, J = 8.60 Hz, 2H), 7.18 – 7.13 (m, 6H), 4.37 (d, J = 17.35 Hz, 2H), 4.24 – 4.16 (m, 4H), 1.97 (s, 6H), 1.72 (s, 6H) ppm; Anal. Calc'd for $C_{50}H_{36}N_4O_{10}$: C, 70.42; H, 4.25; N, 6.57; Found: C, 68.71; H, 4.35; N, 6.35.

2.9 Acknowledgements

I would like to thank all of the coauthors who made this work possible, including Jonathan Bachman, Benjamin Robertson, Chenhui Zhu, Jeffrey Long, and Brett Helms. This work was supported by the Center for Gas Separations Relevant to Clean Energy Technologies, an Energy Frontier Research Center funded by the U.S. Department of Energy, Office of Science, Basic Energy Sciences under Award # DE-SC0001015. Ben Robertson was supported by the U.S. Department of Energy, Office of Science, Office of Workforce Development for Teachers and Scientists (WDTS) under the Science Undergraduate Laboratory Internship (SULI) program. Portions of this work, including synthesis, characterization, and film processing, were carried out as a User Project at the Molecular Foundry, which is supported by the Office of Science, Office of Basic Energy Sciences, of the U.S. Department of Energy under Contract No. DE-AC02-

05CH11231. WAXS was carried out at beamline 7.3.3 of the Advanced Light Source, which is supported by the Director, Office of Science, Office of Basic Energy Sciences, of the U.S. Department of Energy under the same contract. We thank Liana Klivansky for assistance with XPS and Nicholas Settineri for assistance with single-crystal X-ray diffraction.

2.10 References

1. B. D. Freeman, *Macromolecules* **1999**, *32*, 375.
2. L. M. Robeson, *J. Membr. Sci.* **1991**, *62*, 165.
3. L. M. Robeson, *J. Membr. Sci.* **2008**, *320*, 390.
4. a) L. M. Robeson, M. E. Dose, B. D. Freeman, D. R. Paul, *J. Membr. Sci.* **2017**, *525*, 18; b) C. Li, S. M. Meckler, Z. P. Smith, J. E. Bachman, L. Maserati, J. R. Long, B. A. Helms, *Adv. Mater.* **2018**, *30*, 1704953.
5. M. Carta, R. Malpass-Evans, M. Croad, Y. Rogan, J. C. Jansen, P. Bernardo, F. Bazzarelli, N. B. McKeown, *Science* **2013**, *339*, 303.
6. H. B. Park, C. H. Jung, Y. M. Lee, A. J. Hill, S. J. Pas, S. T. Mudie, E. Van Wagner, B. D. Freeman, D. J. Cookson, *Science* **2007**, *318*, 254.
7. R. Swaidan, B. Ghanem, I. Pinnau, *ACS Macro Letters* **2015**, *4*, 947.
8. D. F. Sanders, Z. P. Smith, R. Guo, L. M. Robeson, J. E. McGrath, D. R. Paul, B. D. Freeman, *Polymer* **2013**, *54*, 4729.
9. a) P. M. Budd, B. S. Ghanem, S. Makhseed, N. B. McKeown, K. J. Msayib, C. E. Tattershall, *Chem. Comm.* **2004**, 230; b) B. S. Ghanem, R. Swaidan, X. Ma, E. Litwiller, I. Pinnau, *Adv. Mater.* **2014**, *26*, 6696.
10. a) B. S. Ghanem, N. B. McKeown, P. M. Budd, J. D. Selbie, D. Fritsch, *Adv. Mater.* **2008**, *20*, 2766; b) M. Lee, C. G. Bezzu, M. Carta, P. Bernardo, G. Clarizia, J. C. Jansen, N. B. McKeown, *Macromolecules* **2016**, *49*, 4147; c) X. Ma, M. Abdulhamid, X. Miao, I. Pinnau, *Macromolecules* **2017**, *50*, 9569.
11. D. M. Muñoz, M. Calle, J. G. de la Campa, J. de Abajo, A. E. Lozano, *Macromolecules* **2009**, *42*, 5892.
12. E. Lozano, J. de Abajo, J. G. de la Campa, *Macromol. Theory Simul.* **1998**, *7*, 41.
13. Z. P. Smith, D. F. Sanders, C. P. Ribeiro, R. Guo, B. D. Freeman, D. R. Paul, J. E. McGrath, S. Swinnea, *J. Membr. Sci.* **2012**, *415–416*, 558.
14. L. M. Robeson, Z. P. Smith, B. D. Freeman, D. R. Paul, *J. Membr. Sci.* **2014**, *453*, 71.
15. S. Kim, H. J. Jo, Y. M. Lee, *J. Membr. Sci.* **2013**, *441*, 1.
16. S. Li, H. J. Jo, S. H. Han, C. H. Park, S. Kim, P. M. Budd, Y. M. Lee, *J. Membr. Sci.* **2013**, *434*, 137.
17. F. Alghunaimi, B. Ghanem, Y. Wang, O. Salinas, N. Alaslai, I. Pinnau, *Polymer* **2017**, *121*, 9.
18. A. G. McDermott, G. S. Larsen, P. M. Budd, C. M. Colina, J. Runt, *Macromolecules* **2011**, *44*, 14.
19. I. Rose, C. G. Bezzu, M. Carta, B. Comesaña-Gándara, E. Lasseuguette, M. C. Ferrari, P. Bernardo, G. Clarizia, A. Fuoco, J. C. Jansen, K. E. Hart, T. P. Liyana-Arachchi, C. M. Colina, N. B. McKeown, *Nat. Mater.* **2017**, *16*, 932.
20. a) A. L. Ward, S. E. Doris, L. Li, M. A. Hughes, X. Qu, K. A. Persson, B. A. Helms, *ACS Cent. Sci.* **2017**, *3*, 399; b) L. C. H. Gerber, P. D. Frischmann, F. Y. Fan, S. E. Doris, X. Qu, A. M. Scheuermann, K. Persson, Y.-M. Chiang, B. A. Helms, *Nano Lett.* **2016**, *16*,

549; c) P. D. Frischmann, L. C. H. Gerber, S. E. Doris, E. Y. Tsai, F. Y. Fan, X. Qu, A. Jain, K. A. Persson, Y.-M. Chiang, B. A. Helms, *Chem. Mater.* **2015**, *27*, 6765.

Chapter 3

Applying Diamine-Appended M_2(dobpdc) as a Next-Generation Gas Separation Membrane Material: Ultrafast Synthesis and Mixed-Matrix Membrane Fabrication

3.1 Introduction

Among the design platforms available for gas separation membranes, mixed-matrix membranes (MMMs) are promising: MMMs offer the low cost, high processability, and mechanical properties of polymers and, if successful, the unbounded separation performance of crystalline microporous materials. Many MMMs overcome the intrinsic permeability-selectivity trade-off of pure polymers.[1] In recent years, zeolites and metal–organic frameworks (MOFs) have been used as fillers in MMMs[2] where typically molecular-sieving and solution-diffusion mechanisms[3] promote gas separation. In this chapter, I introduce the first example of a phase-change MOF,[4] mmen-Mg_2(dobpdc) (mmen = *N*,*N*′-dimethylethylenediamine; dobpdc^{4-} = 4,4′-dioxidobiphenyl-3,3′-dicarboxylate), in a MMM that displays enhanced permeability and selectivity for CO_2 over N_2 (Figure 3.1).

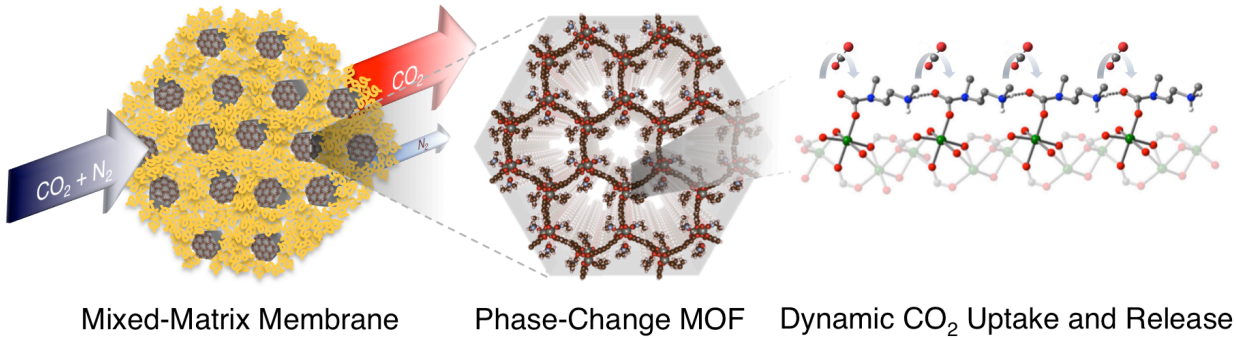

Figure 3.1 By incorporating phase-change MOFs in a mixed-matrix membrane, the permeability and selectivity for CO_2/N_2 separations can be greatly enhanced. Critical to the design of these composite membranes is the nanoscale dimension of the phase-change MOF filler, which serves to mitigate the effects of plasticization and likelihood of defects in the membrane that would negatively impact gas transport selectivity. Critical to the performance of the membranes is the dynamic uptake and release of CO_2 along the diamine molecules appended to open metal sites lining the MOF channels.

While the use of mmen-Mg_2(dobpdc) as a CO_2 adsorbent and its associated thermodynamic underpinnings have been investigated thoroughly,[4,5] the kinetics of CO_2 transport in this phase-change material in a driven (i.e., out-of-equilibrium) system have not been previously reported; thus, their prospects for improving MMM-based gas separations are still unclear. Prior to our work, it had been demonstrated that mmen-Mg_2(dobpdc) has a novel cooperative CO_2 uptake mechanism that leads to a nonclassical, steplike adsorption isotherm.[4] Having such a high, readily reversible CO_2 uptake makes the application of mmen-Mg_2(dobpdc) in membranes very attractive. Prior attempts to incorporate this phase-change MOF in an MMM had failed, likely due to the dimensions of Mg_2(dobpdc) crystals obtained through conventional synthetic approaches. These syntheses produce high aspect-ratio microrods that, when blended with polymer, typically protrude from the matrix and appear to exhibit poorly formed polymer/MOF interfaces. To resolve issues associated with compositing larger MOF crystals, we needed to develop a new synthesis of Mg_2(dobpdc) that allows a high degree of control over the crystal morphology in order to form high-quality nanocrystals. In this chapter, I first detail an exceptionally rapid synthesis of high quality M_2(dobpdc) MOFs that substitutes conventional divalent metal salts with divalent metal oxides (Figure 3.2). Then I show that this MO-based synthetic pathway can be controllably arrested to form high-quality M_2(dobpdc) nanorods suitable for MMM preparation. Within a polymer matrix, these phase-change fillers improve CO_2 permeability over that of N_2.

3.2 Metal Oxides as Reactants in M_2(dobpdc) Synthesis

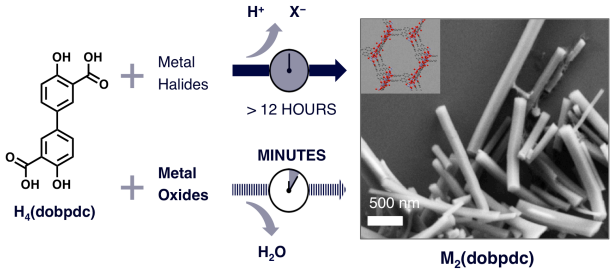

Figure 3.2 MOFs, such as M2(dobpdc), are generated in minutes under controlled reaction conditions from divalent metal oxides as precursors. Conventional syntheses from metal (pseudo)halide salts generate acidic byproducts and require multi-hour reactions times. Scale bar is 500 μm.

One of the factors currently limiting the expedient production of M_2(dobpdc) is that reaction times in excess of 12 h are required when preparing the MOF in solution (e.g., *N*,*N*-diethylformamide) from metal halide or metal pseudohalide salts and H_4(dobpdc) ligand. I hypothesized that the generation of acidic byproducts during this sequence of reactions may contribute to slow reaction times for this MOF. Recent studies have concluded as much in the synthesis of porous flexible iron fumarate MIL-88A MOF when acids were present. Organic acids were shown to inhibit crystallization while also contributing to a lower yield and a smaller particle size; conversely, increasing the pH had the opposite effect.[6] Were it possible to avoid acidic byproducts, e.g., via dissolution of MO solids as precursors, then the integration of H_4(dobpdc) into M_2(dobpdc) MOFs could, in principle, proceed at a faster rate.

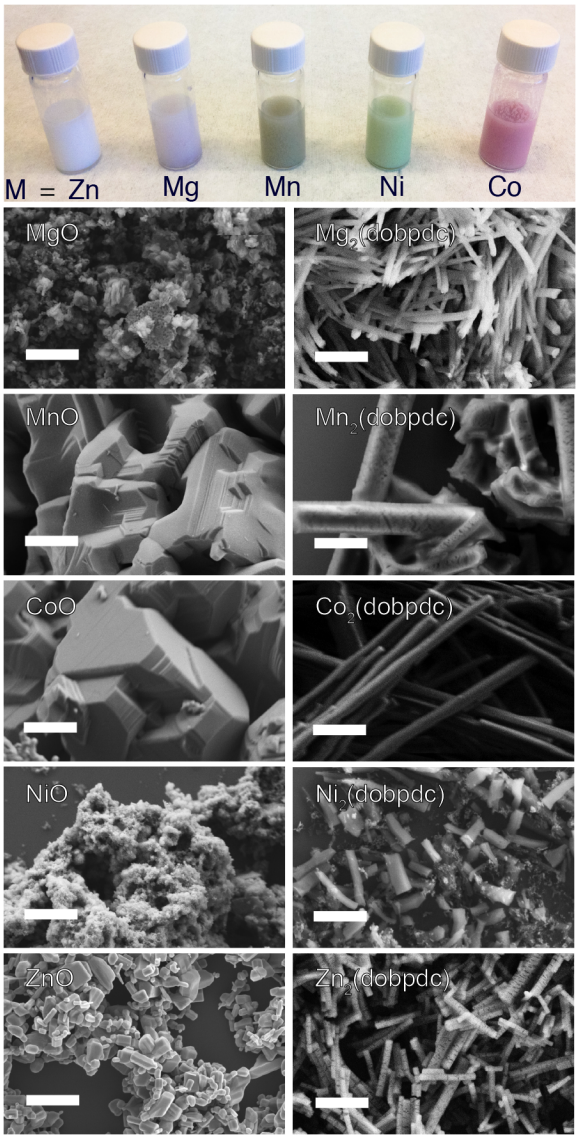

Figure 3.3 Top: Photograph of the M_2(dobpdc) MOFs dispersed in methanol. Bottom: scanning electron micrographs of MO precursors (left column) and their respective reaction products after high-temperature treatment with H_4(dobpdc) in DMF. Scale bars are 1.0 μm.

Our optimized (pseudo)halide-free M_2(dobpdc) synthesis involves the temperature-assisted dissolution of H_4(dobpdc) in *N*,*N*-dimethylformamide at 120 °C, where $[H_4(dobpdc)]_0 = 0.50$ M, and subsequent addition of the MO solid. The reaction was allowed to proceed until the solid-to-solid transformation was complete (minutes to hours, depending on the MO). Several of the reactions generated highly colored products, which was most evident after cleanup (Figure 3.3).

In navigating the reaction space for this chemical transformation, we noted that the composition and morphology of the MO precursor played central roles in the rate of M_2(dobpdc)

formation (Figure 3.3). The most rapid transformations were observed using MgO and ZnO solids as precursors to Mg_2(dobpdc) and Zn_2(dobpdc), respectively, with yields of 67% isolated yield for Mg_2(dobpdc) and 88% isolated yield for Zn_2(dobpdc). Interestingly, these reaction conditions were also applied successfully in the synthesis of standard M-MOF-74 materials, M_2(dobdc), when 2,5-dihydroxy-1,4-benzenedicarboxylic acid, H_4(dobdc), was used in the transformation. Whereas for M = Co, Fe, Ni, pure phase of M_2(dobdc) materials were obtained, chemical transformations employing ZnO solids led to mixed-phase materials (Figure 3.23).

3.3 Crystallinity and Porosimetry as Quality Metrics

Despite their unconventional method of preparation, the M_2(dobpdc) MOFs generated were of excellent quality as evidenced by their high crystallinity (Figure 3.4a,c; Figure 3.24), high surface areas (Figure 3.4b,d), and thermogravimetric analysis (TGA) analysis (Figure 3.25). All XRD spectra were well matched to their expected and previously reported data. Furthermore, their BET surface areas, 2290 ± 30 $m^2 g^{-1}$ for Zn_2(dobpdc) and 2910 ± 40 $m^2 g^{-1}$ for Mg_2(dobpdc), were in line with previous reports[4,7] (Table 3.1); the lack of hysteresis in the adsorption/desorption curves further indicated excellent measurement reliability and the absence of micropore blockages or other structure-related mass-transport bottlenecks. Finally, to demonstrate that Mg_2(dobpdc) MOFs exhibit characteristic CO_2-adsorption properties as previously reported,[4,7] we loaded *N*,*N*′-dimethylethylenediamine (mmen) into the framework, where they are chemisorbed at the open metal centers in the framework; indeed, we observed the expected step-function in CO_2 uptake at low pressure (Figure 3.5).

Table 3.1 BET parameters from for the N2 adsorption isotherms of Mg2(dobpdc) and Zn2(dobpdc) MOFs.

	Mg_2(dobpdc)	**Zn_2(dobpdc)**
BET surface area / $m^2 g^{-1}$	2914 ± 41	2294 ± 32
Slope	0.033396 ± 0.000467	0.042442 ± 0.000601
Y-Intercept	0.000091 ± 0.000030	0.000101 ± 0.000040
C	367.955864	423.098141
Correlation Coefficient	0.9995107	0.9997996
p / p_0 low	0.039248447	0.048626204
p / p_0 high	0.090682570	0.081118353

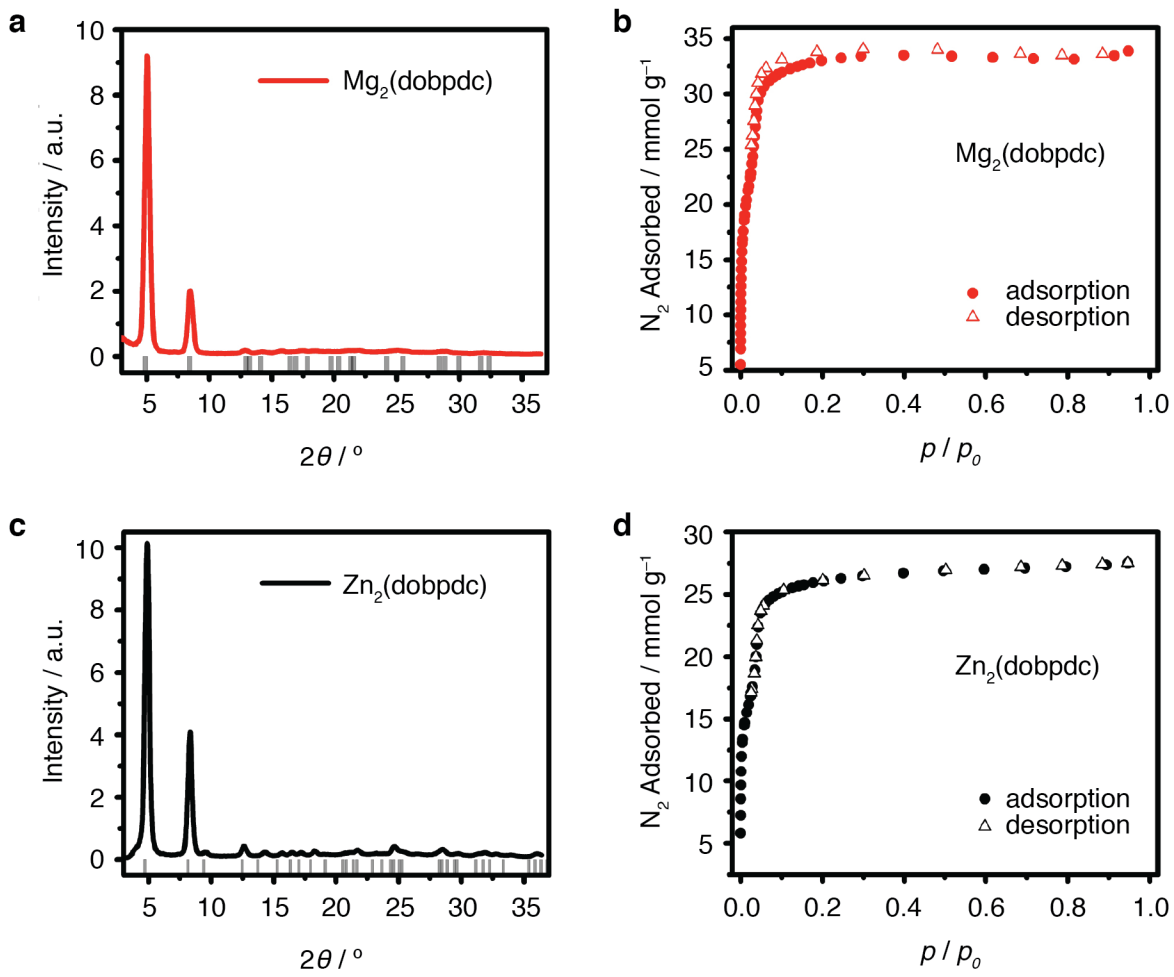

Figure 3.4 a,c) XRD patterns and b,d) BET surface area measurements for the Mg_2(dobpdc) (red curves) and Zn_2(dobpdc) (black curves).

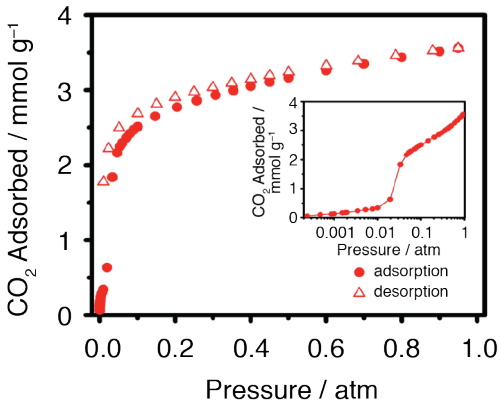

Figure 3.5 Carbon dioxide absorption/desorption for (mmen)-Mg_2(dobpdc) MOFs versus relative pressure, plotted in linear and log scale (inset). The representation in the inset highlights the characteristic step-like transition, which corresponds to a highly cooperative uptake of CO_2 as was previously reported by McDonald et al.[4]

3.4 Assessment of the Reaction Trajectory from MO Dissolution to M_2(dobpdc) Crystallization

In contrast to previously reported metal oxide-to-MOF chemical transformations,[8] we did not observe significant pseudomorphic replication or self-limited growth of the MOF around the MO starting materials (Figure 3.3). To understand this outcome better, we monitored in greater detail the dissolution–crystallization trajectory of MgO to Mg_2(dobpdc) at different reaction times by sampling aliquots and analyzing the intermediates using ex situ SEM (Figure 3.6). Within the first 30 s of the transformation, we found that clusters of Mg_2(dobpdc) had sprouted from common nucleation points across the MgO surface (Figures 3.6a,b). After 2 min, these growths elongated (Figure 3.6c), and after 5 min, urchin-like morphologies were prevalent (Figure 3.6d). At this stage of the reaction, the XRD pattern matched that for Mg_2(dobpdc) with a small peak at 44° attributed to unreacted MgO (Figure 3.9a). These intermediate urchin morphologies are critical to the formation of high-quality Mg_2(dobpdc) nanorods, as the MOF "spines" can be isolated through the selective etching of the metal oxide core, which I discuss later in section 3.9. After 10 min, the characteristic, highly anisotropic M_2(dobpdc) rod morphology (Figure 3.6e) was distinguishable from the faster forming clusters, and the MgO signature in the XRD was no longer present (Figure 3.9b). The crystal shape and crystallinity did not change significantly as reaction times were increased further, e.g., after 60 min (Figures 3.6f and 3.9b). The presence of MgO while M_2(dobpdc) rods are forming suggests MO etching is the rate-limiting step, signifying M^{2+} availability as a critical factor in optimizing this reaction pathway.

We found that the kinetic trajectories of MOF formation from ZnO and CoO were strikingly similar to that for MgO. However, the reaction was considerably slower in both cases: Zn_2(dobpdc) appeared 10 min after the reaction was initiated, and its crystallinity improved significantly between 30–60 min (Figure 3.7); however, CoO required at least 2 h to dissolve and begin to crystallize as Co_2(dobpdc) (Figure 3.8).

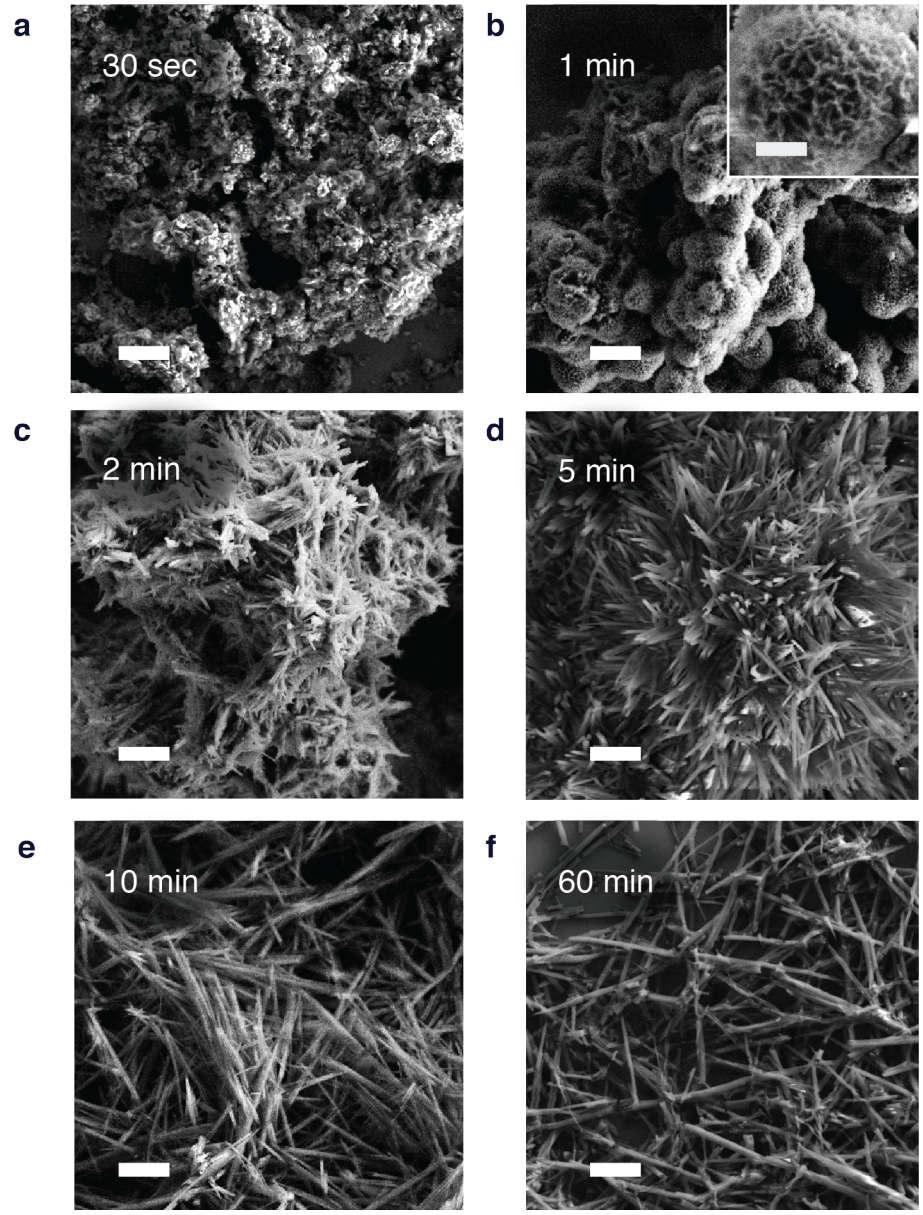

Figure 3.6 SEM along the reaction trajectory of MgO to Mg_2(dobpdc): a) 30 s; b) 1 min; c) 2 min; d) 5 min; e) 10 min; f) 60 min. Scale bars for all panels are 2.0 μm; the inset scale bar is 500 nm.

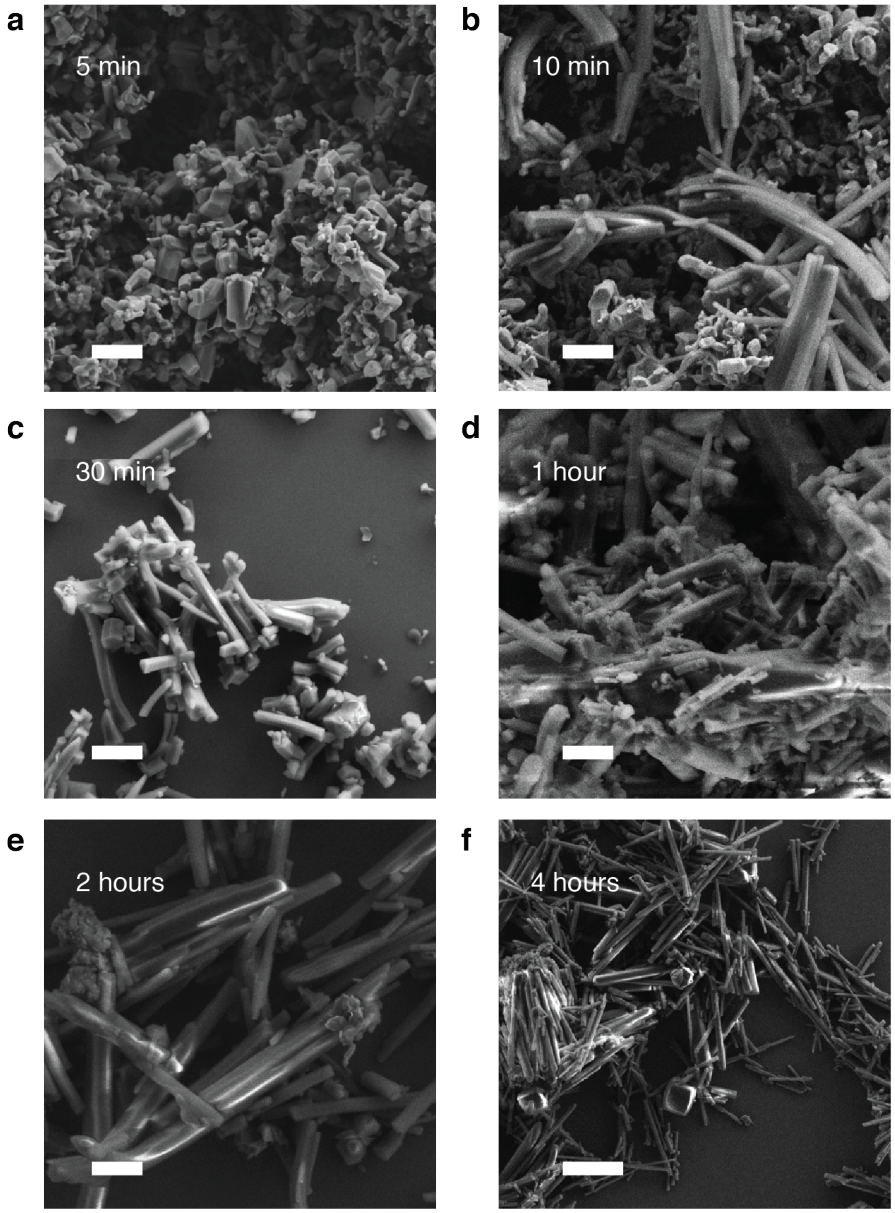

Figure 3.7 SEM along the reaction trajectory of ZnO to Zn_2(dobpdc) starting from commercial ZnO powders. a) 5 min; b) 10 min; c) 30 min; d) 1 h; e) 2 h; f) 4 h. Scale bars for panels a) through e) are 1.0 μm, scale bar for panel f) is 5.0 μm.

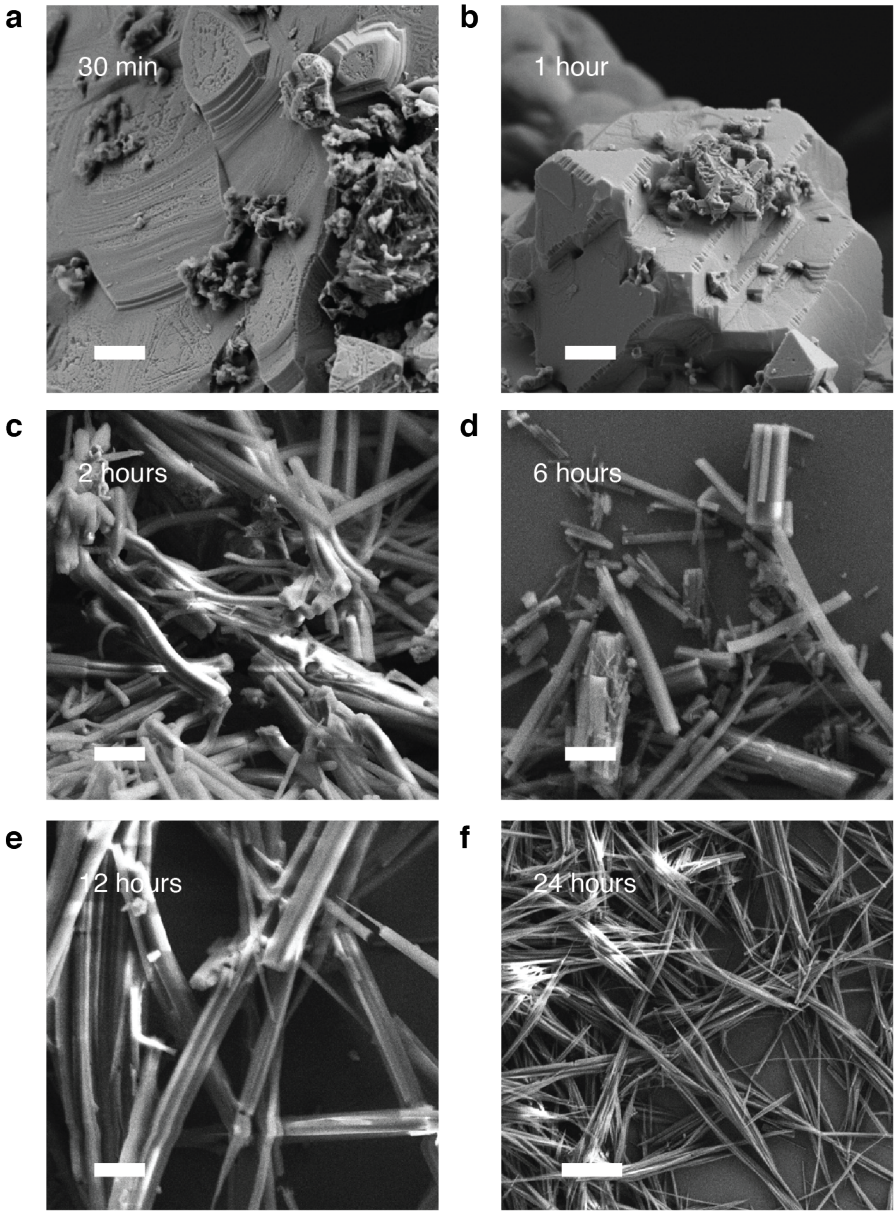

Figure 3.8 SEM along the reaction trajectory of CoO to Co_2(dobpdc) starting from commercial CoO powders. a) 30 min; b) 1 h; c) 2 h; d) 6 h; e) 12 h; f) 24 h. Scale bars for panels a) through e) are 1.0 μm, scale bar for panel f) is 5.0 μm.

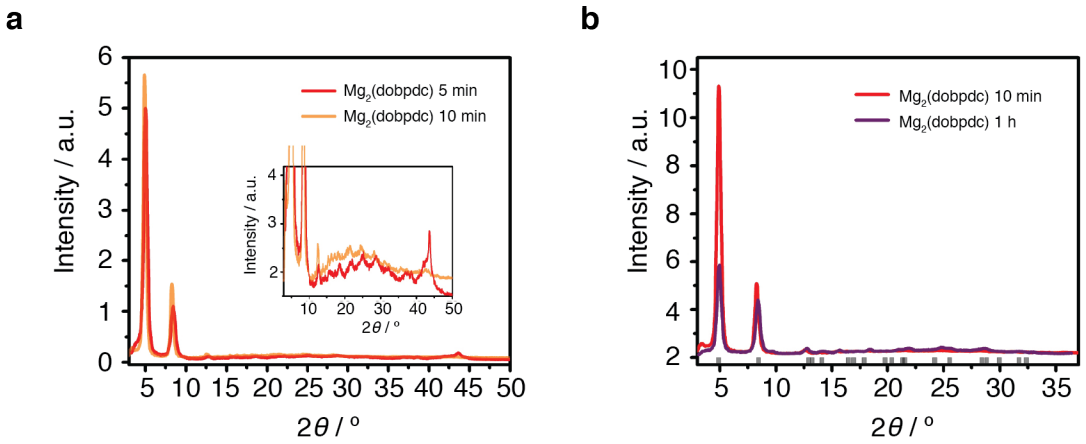

Figure 3.9 a) XRD patterns of 5 min (red curve) and 10 min (orange curve) of Mg_2(dobpdc) aliquots during crystallization. The peak at 44° assigned to residual MgO is still present after 5 min of reaction, and subsequently disappears after 10 min. b) XRD patterns showing no peak position variation after 1 h.

3.5 MO Etching Kinetics

In order to quantify the precursor dissolution rate underpinning the availability of M^{2+} during MOF formation, we introduced MO solids to a solution of salicylic acid (H_2(sal)) in DMF at 120 °C (i.e., our optimized reaction conditions). Salicylic acid here serves as a monofunctional analogue to H_4(dobpdc), which allowed us to track MO dissolution without contributing influence from other chemical species also involved in MOF crystallization. The time-evolution of MO etching by salicylic acid was observed using in situ Fourier transform infrared spectroscopy (FT-IR). Spectra were collected every 15 s over a spectral range of 600 to 2000 cm^{-1}. Metal salicylate formation $M[H(sal)]_2$ coincided with the disappearance of the H_2(sal) C–O stretch at 1219 cm^{-1}. This phenomenon was observed in all samples analyzed and was therefore a useful and selective marker for MO dissolution. Figure 3.10 shows the IR spectral changes over time from 1180 to 1300 cm^{-1} and the decrease in signal intensity, evidenced in the 2-D plot as a transition from red to blue, at 1219 cm^{-1} during the etching of ZnO, MgO, and CoO.

Our investigation of the etching process by ex situ SEM had indicated that salicylic acid first etches channels on the surface and within MO (Figure 3.11), rather than proceeding via a gradual dissolution of the solid. This outcome highlights a unique aspect of this chemistry in that the surface area of the MO increases along the reaction trajectory, while the primary dimensions of the particle do not change dramatically at early stages in the reaction. With these phenomena in mind, we were able to fit the disappearing/emerging peaks in the in situ FT-IR using the Prout–Tompkins equation.[9] The physical model from which this equation arises accounts for both the initial acceleratory kinetics due to the increase in reactive surface area (Figure 3.11) and the deceleratory kinetics, due to the depletion of metal oxide starting material with time. The experimental data points have been thus fitted with the following equation:

$$\log\left(\frac{f}{f-1}\right) = k(t - t_0) \tag{13}$$

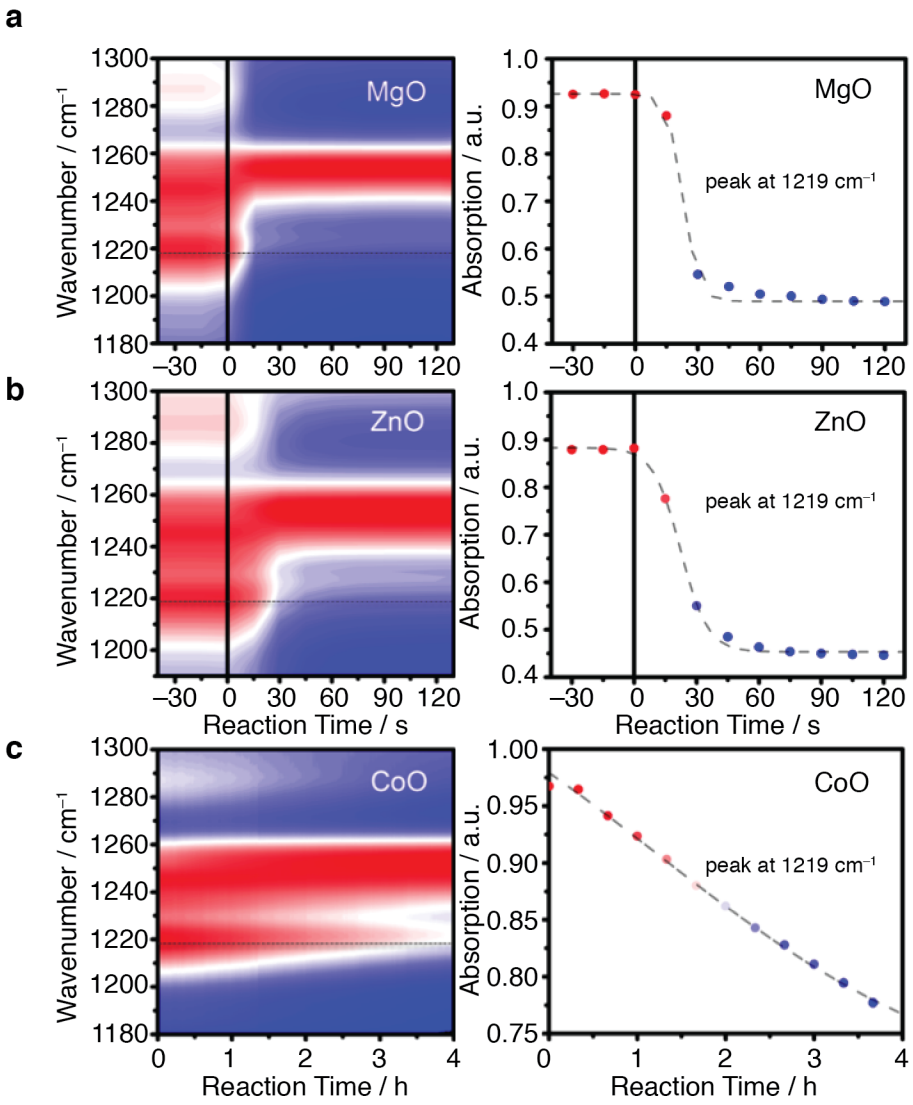

Figure 3.10 In situ FT-IR spectra was used to quantify the etch rates of divalent metal oxides in the presence of salicylic acid, H_2(sal). Solid MO precursors were added to solution of H_2(sal) in DMF (2.0 M) at 120 °C, and the spectra were recorded in situ at 15 s intervals. IR spectra over an energy range of 1180–1300 cm^{-1} are plotted versus reaction time. The color scale is set to distinguish high absorption (red) from low absorption (blue). Data along the indicated line-cuts at 1219 cm^{-1} represent the time-evolution of the interconversion of H_2(sal) to M[H(sal)]$_2$ (right column). These data were fit using the Prout–Tompkins equation (dotted lines) to extract MO etch rates under these conditions. a) MgO dissolved within 30 s, b) ZnO in 1 min, while c) CoO took 8 h to completely dissolve.

where f is the extent of reaction, k is the etching rate constant, and t_0 is the characteristic time of etching. Our treatment of the data in this manner allowed us to extract effective rate constants for MO etching by salicylic acid for MgO, ZnO, and CoO (Table 3.2).

The modeled time constants indicated that complete etching of the MO under these reaction conditions varied from tens of seconds for ZnO and MgO to hours for CoO. These data were consistent with the relative rates of M_2(dobpdc) formation (fast for M = Zn and Mg, slower for M = Co), supporting our hypothesis that fast MO etching is critical for optimized M_2(dobpdc) synthesis and that etching is rate-limiting overall.

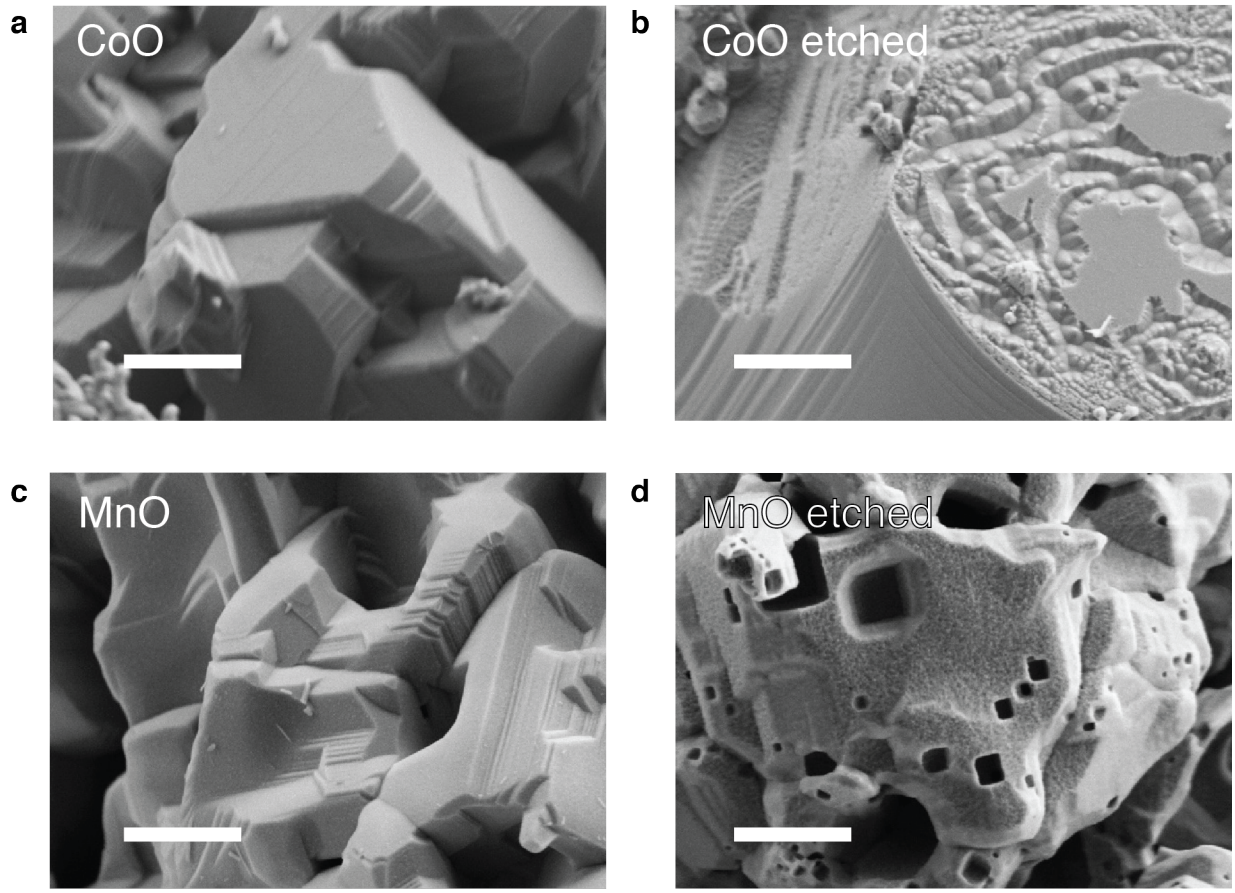

Figure 3.11 Scanning electron micrographs of two slow-reacting metal-oxide precursors: commercial powders of a) CoO and c) MnO; and etched MO after 1 h for b) CoO and d) MnO. Anisotropic etching seems to proceed along crystallographic facets of the metal oxides. Scale bars are 1.0 μm.

Table 3.2 MO etch rate constants (k) and time constants (t_0) extracted from the FT-IR spectra in Figure 3.10 after fitting to the Prout-Tompkins Equation.[9]

Fitted Parameter / MO	MgO	ZnO	CoO
k (s^{-1})	0.265	0.152	0.000156
t_0 (s)	3.77	6.57	6410

3.6 Ultrafast Synthesis of M_2(dobpdc) from MO Colloidal Nanocrystal Precursors

Based on this insight into the rate-determining step, we offer a means to push M_2(dobpdc) synthesis to its fringe kinetic limit: substitute commercially available MO powders with custom-prepared divalent MO colloidal NCs. Colloidal nanocrystals, in principle, offer at least an order of magnitude increase in available surface area. Nonetheless, to maximize interfacial contact area between the NCs and the transforming solution of H_4(dobpdc) in DMF, we elected to remove the NC's native coordinating organic ligands using BF_3-mediated chemistry recently developed in our group.[10] Cationic naked nanocrystals[10,11] generated in this manner yield homogeneous dispersions in DMF, which may further benefit reaction kinetics; furthermore, use of these dispersions in DMF obviates the use of multiple solvents in the reaction

mixture, which is known to influence MOF nucleation, crystal growth, and Ostwald ripening.[12] This BF_3-mediated ligand-stripping procedure was carried out on colloidal ZnO and CoO nanocrystals as archetypes for moderate- and slow-etching MO materials (Figure 3.10), respectively; these were hypothesized to benefit most from any rate acceleration offered by increased surface area and homogeneous reaction conditions.

Indeed, by adding dispersions of naked ZnO NCs (100 mg mL^{-1}) to H_4(dobpdc) in DMF ($[H_4(dobpdc)]_0$ = 0.50 M) at 120 °C, an instantaneous reaction was observed. Care was taken to acquire aliquots along the growth trajectory (30 s–1 h). The reaction products obtained from these aliquots were analyzed by SEM and XRD (Figure 3.12a,b) after being rinsed with DMF

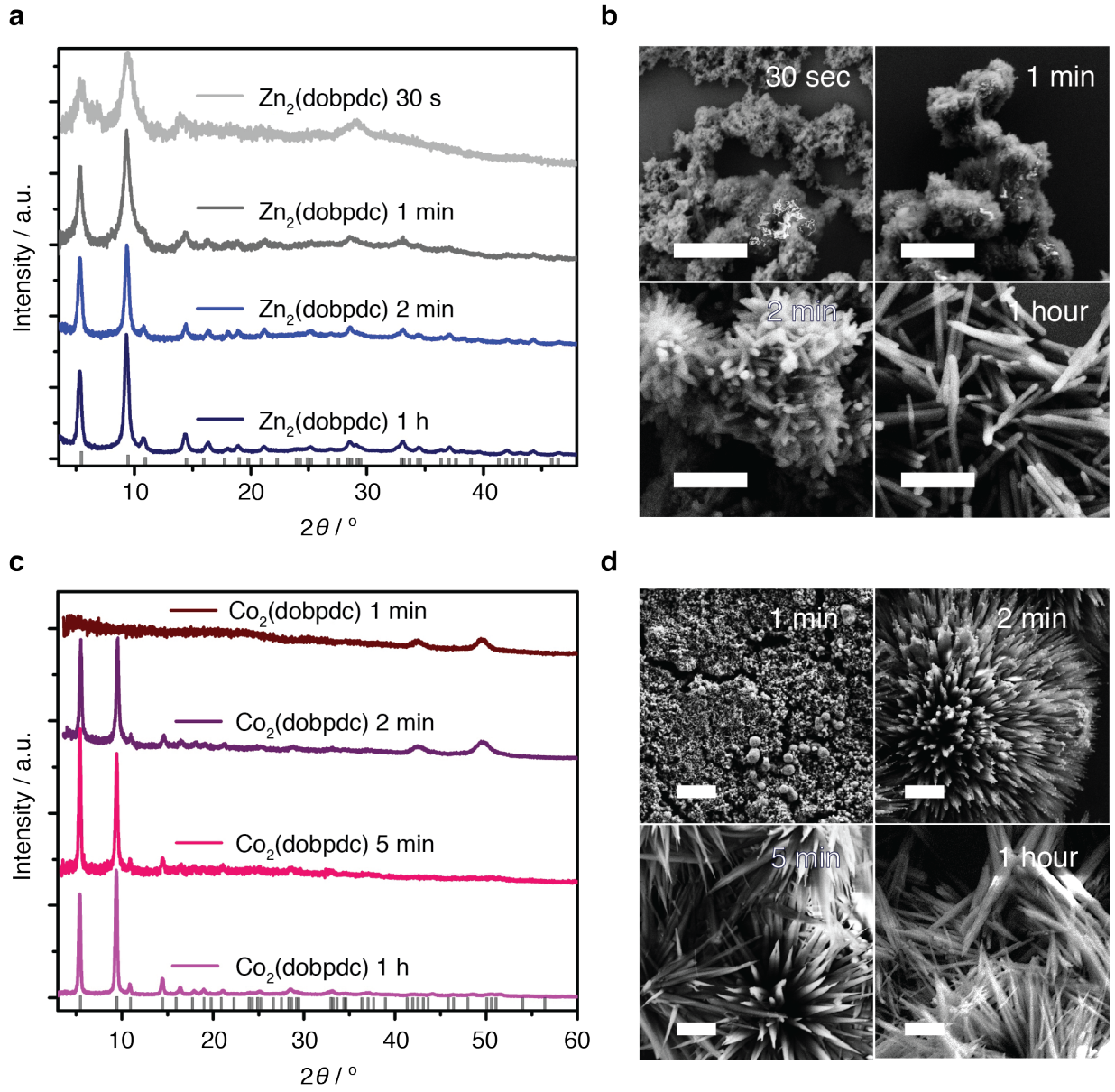

Figure 3.12 a) XRD patterns and b) corresponding SEM images acquired from reaction products along the reaction trajectory from 7 nm colloidal ZnO NCs to Zn_2(dobpdc); and c,d) the same along the reaction trajectory from 9 nm colloidal CoO NCs to Co_2(dobpdc). Scale bars are b) 1 μm and d) 2 μm.

and methanol. Notably, MOF signatures (θ = 6°–9°) in the XRD were evident even after 30 s, and crystalline ZnO was no longer observed (θ = 30°–40°). The corresponding SEM images along the reaction trajectory showed an exceptionally fast evolution in composition within the first 2 min, while the morphology (and crystallinity) of the material did not change significantly after up to 1 h of reaction. Close examination of the SEM series highlights that MOFs grown under these conditions originate from urchin-like structures, which fall apart along the reaction trajectory and ultimately result in well-dispersed crystalline needles (Figure 3.12b).

The accelerated pace of this MO-to-MOF transformation was likewise observed for naked colloidal CoO NCs,[13] where the analogous transformation from bulk MO precursors was particularly sluggish. As with ZnO, the chemical transformation from naked CoO NCs to Co_2(dobpdc) MOFs was observed over a time-span of 30 s to 1 h using our standard conditions. The XRD peaks at 43° and 49°, ascribed to unreacted CoO, were only observed within the first 2 min of reaction. After 2 min, MOF crystals were clearly visible both from XRD and SEM (Figure 3.12c,d). Furthermore, after 5 min, the CoO is completely etched and Co_2(dobpdc) is prevalent. The morphology of the Co_2(dobpdc) crystals did not change appreciably up to 1 h. Thus, we reason that the slow-etching metal oxides benefit most from the larger available surface area of naked MO NCs as hypothesized. We conclude from our work that colloidal divalent metal oxide nanocrystals[14] are unexpected yet privileged precursors to this important family of MOFs and may be so for others. Our work also challenges the conventional wisdom that the orchestration of events leading to MOF crystallization is time-intensive.[15]

3.7 Mg_2(dobpdc) Nanocrystal Synthesis from MO Precursors

To access M_2(dobpdc) nanocrystals needed for high-quality MMM preparation (Figure 3.13), we altered the MO to M_2(dobpdc) reaction trajectory to favor the growth of isolable nanorods. Here, we focused on Mg_2(dobpdc) (Figure 3.13), which is known to cooperatively uptake CO_2 at low partial pressures relevant to membrane separations.[4] We were ultimately successful by introducing the H_4(dobpdc) ligand to a superstoichiometric amount of MgO in DMF at 120 °C, which generates a coating of Mg_2(dobpdc) nanorods on MgO. Precursor stoichiometry and reaction time were varied in turn to obtain Mg_2(dobpdc) nanorods with controlled morphology and length (e.g., 100–200 nm in size) (Figure 3.13). To isolate MOF nanorods, the MgO core was simply dissolved in acetic acid. The resulting purified MOF nanorods were found to unaltered by the acetic acid treatment and they could be dispersed readily in polar aprotic solvents, such as DMF (see section 3.12). Visualization of the reaction pathway is

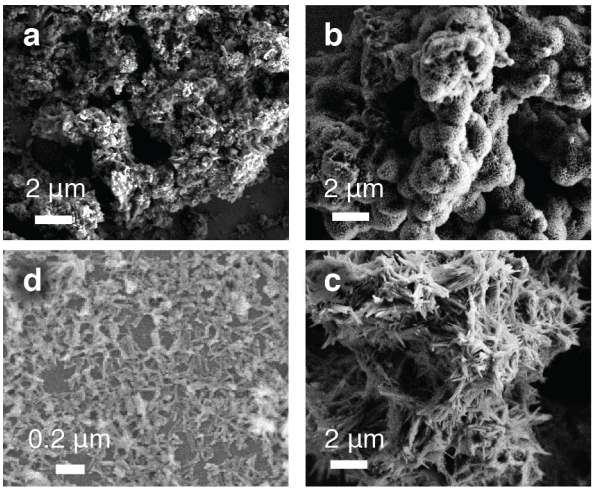

Figure 3.13 SEM images along the reaction coordinate, which first yields Mg_2(dobpdc) nanorods on MgO and then freely dispersible products post-processing. a) MgO precursor immersed for 30 s in DMF containing H_4(dobpdc). b) Reaction product after 5 min; Mg_2(dobpdc) nanorods coat the MgO crystals, forming urchins. At this point the reaction could be either let got to completion—yielding Mg_2(dobpdc) microrods (c)—or quenched and treated with acetic acid to etch the MgO core, producing dispersible Mg_2(dobpdc) nanorods (d).

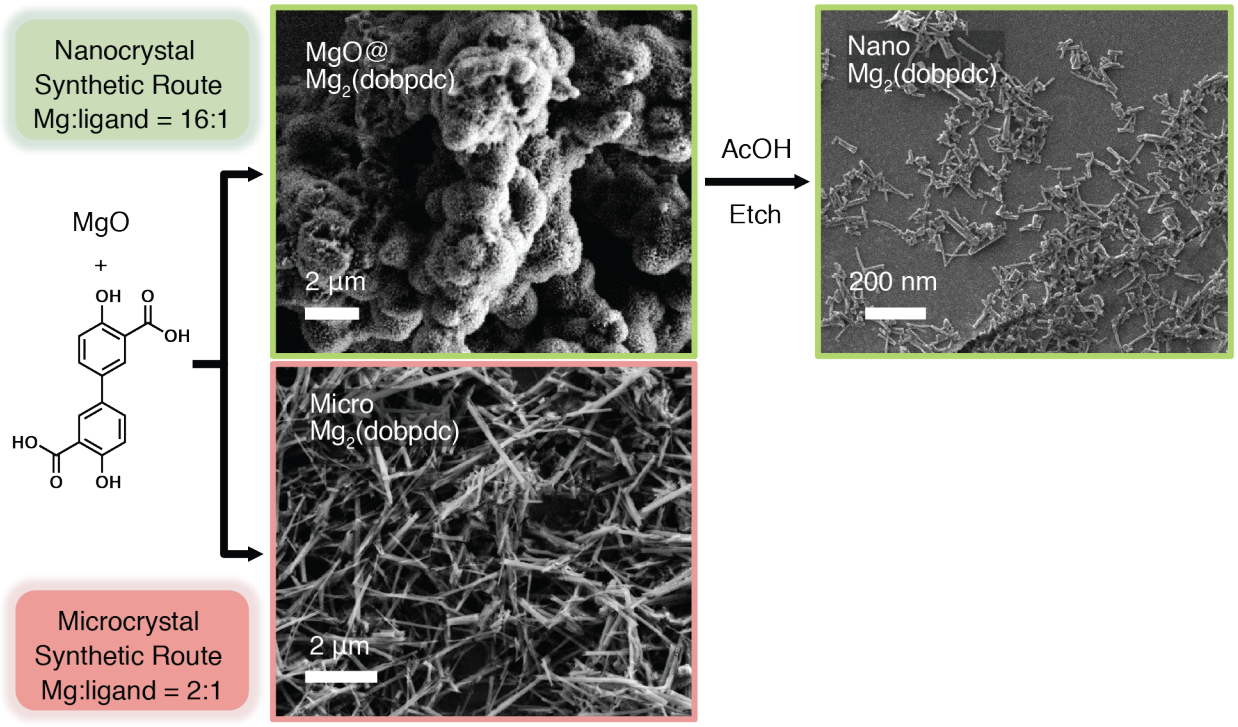

Figure 3.14 Varying the ratio of MgO to H_4dobpdc ligand during the chemical synthesis of Mg_2(dobpdc) MOFs allows the reaction coordinate to diverge, yielding either a forest of nanocrystalline MOFs on MgO solids or microcrystalline MOF rods. In the case of the former, the nanocrystalline MOFs can be released from the underlying MgO solids using acetic acid as a mild etchant. $Mg(OAc)_2$ byproducts are easily removed from the final nano-Mg_2(dobpdc) product.

depicted in Figure 3.14. Notably, we found that higher Brunauer–Emmett–Teller (BET) surface areas and higher amine loadings (Figure 3.26), were achieved after treating the nanorods in a subsequent step with H_4(dobpdc) in DMF at 120 °C, consistent with the presence of fewer defects in the final material.

Differences in the crystallinity of the Mg_2(dobpdc) nanorods compared to the micron-scale rods obtained from a bulk preparation are evident in Figure 3.16. Both experimental diffraction patterns match the calculated reflections for the crystal structure, and the peak broadening observed for the nano-MOF sample is consistent with the expected Scherrer broadening. Using Scherrer analysis, we estimate the crystallite size to be ~12 nm, corresponding to the average nanorod cross-section. We further characterized the BET surface area for both samples (Figure 3.17), which unexpectedly revealed a greater surface area for the Mg_2(dobpdc) nanorods than for the microrods. Deviations in behavior with regard to the shape of the N_2 isotherm manifests at high pressures, likely due to adsorption at surface sites, which are more prevalent in the nano-MOF.

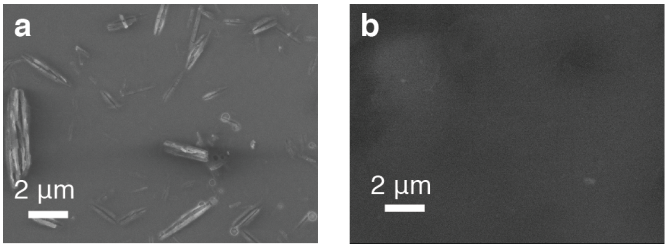

Figure 3.15 SEM micrographs comparing the morphology of mmen-Mg_2(dobpdc) / 6FDA-DAM MMMs with a) micron-sized and b) nano-sized MOF fillers.

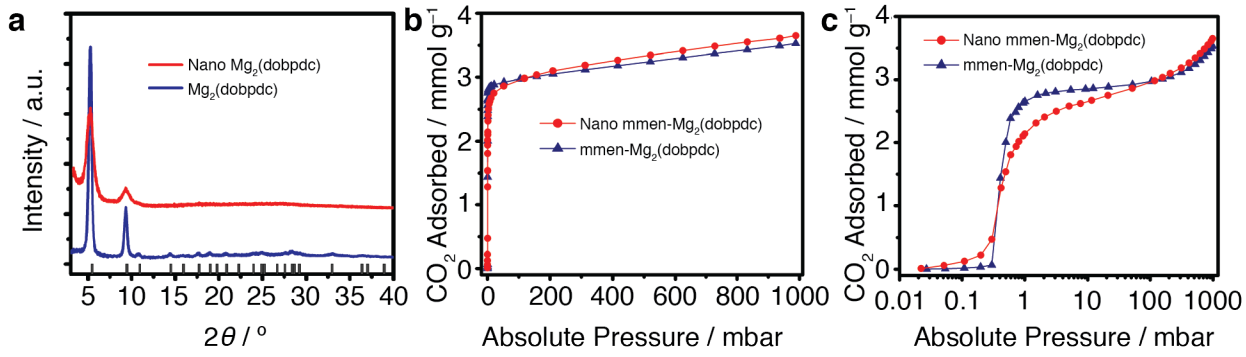

Figure 3.16 a) PXRD of Mg_2(dobpdc) nanocrystals (red) and microcrystals (blue). In the nano-MOF sample, only high intensity peaks are visible and their FWHM is broader due to the small size of the crystallites. CO_2 adsorption isotherms of nanocrystalline (red) and microcrystalline (blue) mmen-Mg_2(dobpdc) in either b) linear or c) semilog plots. Saturation values are similar for both, while the adsorption step of mmen-Mg_2(dobpdc) nanorods is broader.

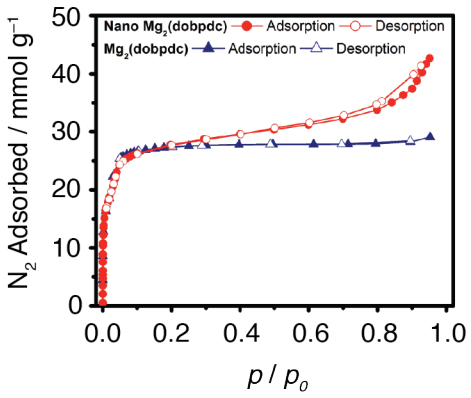

Figure 3.17 Surface-area comparison between micron-sized (blue) and nano-sized (red) Mg_2(dobpdc) rods. Both MOFs were synthesized from MgO precursors: microrods following the synthetic procedure we previously reported, and nanorods using the 3-step procedure described in this work. The N_2 adsorption/desorption curves at 77 K give calculated BET surface areas of 2700 ± 82 m^2 g^{-1} and 2878 ± 75 m^2 g^{-1} for micron- and nano-sized Mg_2(dobpdc), respectively.

3.8 Accessing Phase-Change Sorption Behavior in Mg_2(dobpdc) Nanocrystals

To complete the preparation of the phase-change filler, *N*,*N*′-dimethylethylenediamine (mmen) molecules were grafted to the Lewis acidic open-metal sites within Mg_2(dobpdc) in toluene. No activation procedure was employed prior to diamine grafting, as we found drying to be detrimental to achieving good nanorod dispersions in the polymer matrix. After activating both nano- and micron-scale samples of mmen-Mg_2(dobpdc) MOFs at 100 °C, their CO_2 uptake was evaluated. The resulting adsorption isotherms are shown in Figure 3.16 as linear and semilog plots. The linear plot (Figure 3.16b) indicates CO_2 saturation capacity is quite comparable for the two crystal sizes, while the semilog plot (Figure 3.16c) reveals that the adsorption "step" of the mmen-Mg_2(dobpdc) nanorods is broader, corresponding to a lesser degree of cooperativity in the adsorption mechanism.[16] This could be due to finite-size effects in the formation of carbamate chains that are limited by the nanocrystal length or it could be the consequence of a higher number of mmen vacancies within the crystal. To put an upper bound on the latter, TGA was

carried out on nano- and micron-sized MOFs to quantify the mmen loadings. The results indicate a decrease in mmen loading within the nanorods of only 1.4% (Figure 3.18), which we believe to be negligible (i.e., within the experimental error).

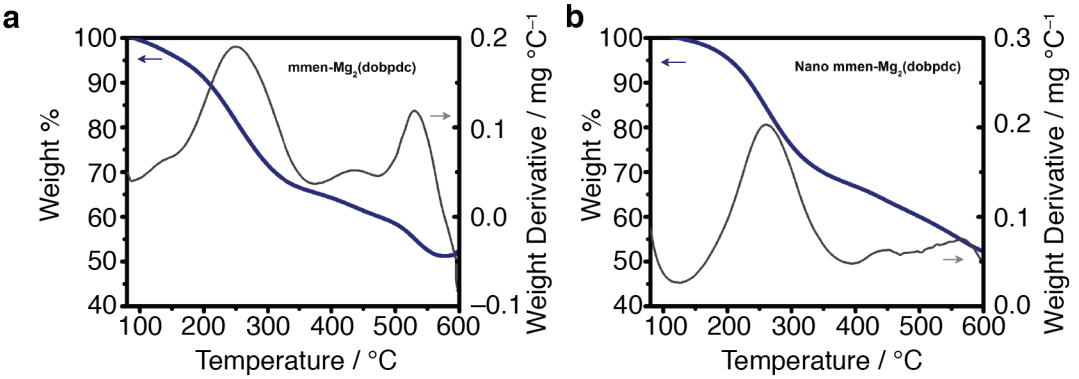

Figure 3.18 Thermogravimetric analysis (TGA) of a) micron- and b) nano-sized mmen-Mg_2(dobpdc). Weight percentage (weight derivative) vs. temperature is plotted in blue (grey). Weights have been normalized to 100% at the temperatures where the MOFs are fully activated (89 and 122 °C for micron- and nano-sized samples, respectively). The mmen-loading was calculated considering 35.4 % theoretical loss in the 120–370 °C region and comparing the experimental weight loss to that value. This results in a mmen loading of 94.3 and 92.9 % for the micron- and nano-sized samples, respectively.

3.9 MMMs Incorporating Phase-Change Fillers

To understand the influence of phase-change MOF fillers on membrane performance, we cast MMMs from a mixture of 6FDA-DAM polyimide and mmen-Mg_2(dobpdc) nanorods in dichloromethane. The quality of the dispersion was excellent, yielding transparent, flexible membranes after solvent evaporation. These membranes were tested in a custom-built, constant-volume, variable-pressure, gas-permeation apparatus. Permeabilities of N_2 and CO_2 were recorded and selectivities were calculated from the acquired data at different input (upstream) pressures. Both CO_2 permeability (Figure 3.19a) and CO_2/N_2 selectivity (Figure 3.19b) are greater in the MMM than in the neat polymer. To better clarify the role of the diamines inside the MOF, we prepared a membrane with bare Mg_2(dobpdc) nanorods within 6FDA-DAM and tested CO_2/N_2 permeation under the same conditions. The results, plotted in Figure 3.19c, are consistent with previous reports that showed that nano Mg_2(dobdc)/polymer MMMs outperform pure polymer membranes.[17] Figure 3.19c also shows that the diamines in mmen-Mg_2(dobpdc) nanorods significantly improve CO_2 permeability while also positively affecting CO_2/N_2 selectivity.

We further performed gas permeation measurements on both 6FDA-DAM and mmen-Mg_2(dobpdc)–6FDA-DAM membranes (Figure 3.20) operating at higher temperatures (35–75 °C). We noted that the decrease in CO_2/N_2 selectivity with increasing temperature for the 6FDA-DAM membrane was significantly less pronounced than that for the mmen-Mg_2(dobpdc)–6FDA-DAM MMM. We expect that with increasing temperature, solubility and selectivity are reduced in both the neat polymer and in the MMM, with solubility playing a more pronounced role in the adsorbent-loaded material. Considering the temperature-dependent step-like character of CO_2 uptake and release that is the hallmark characteristic of the phase-change mmen-Mg_2(dobpdc) filler, adsorption sites within the MOF are left increasingly unoccupied at higher temperature, effectively decreasing the CO_2 solubility of the MMM. This effect dominates the steep decrease in CO_2/N_2 selectivity with increasing temperature in the MMM and corroborates

our hypothesis that amine-appended MOFs primarily improve the performance of MMMs by increasing the CO_2 solubility. These data also suggest that the prevalence of interfacial polymer–MOF voids in the MMM is minimal or at least inconsequential.

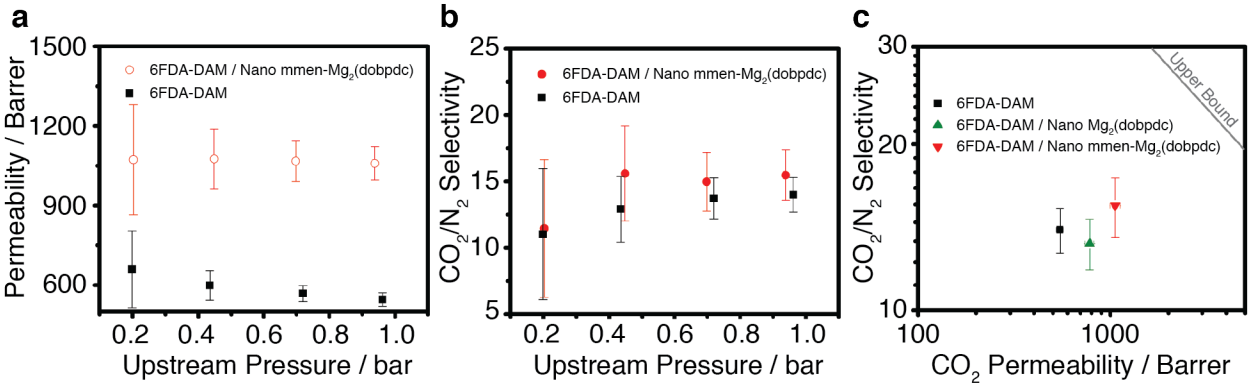

Figure 3.19 Gas permeability measurements on neat 6FDA-DAM polymer (black) and 6FDA-DAM mixed-matrix membranes (red) with loaded with 23% *w/w* mmen-Mg_2(dobpdc) nanorods: a) CO_2 permeability versus upstream pressure; and b) CO_2/N_2 selectivity versus upstream pressure. Both CO_2 permeability and CO_2/N_2 selectivity increase in the MMM compared to the neat polymer. c) Robeson plot for CO_2/N_2 separation showing performances of neat 6FDA-DAM (black), 6FDA-DAM mixed-matrix membranes incorporating Mg_2(dobpdc) nanorods (green), and 6FDA-DAM mixed-matrix membranes incorporating phase-change mmen-Mg_2(dobpdc) nanorods (red). The 2008 Robeson upper bound is plotted as a gray line.[18]

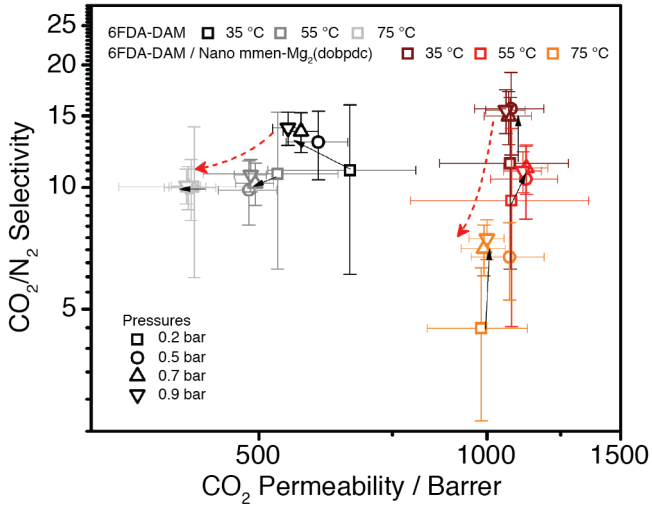

Figure 3.20 Robeson plot representation of gas permeability measurements at different temperatures on the neat 6FDA-DAM polymer (grey scale) and on the 6FDA-DAM/nano mmen-Mg_2(dobpdc). For each temperature (35 °C, 55 °C, 75 °C), data were acquired at 4 different pressures, which are represented by geometric symbols (see legend). For guiding the eye, pressure increase at a given temperature is indicated by black arrows and temperature increase at 0.9 bar is indicated by red dashed arrows, for both the pure polymer and the mixed-matrix membrane.

3.10 Analysis of Gas Transport Properties

On the basis of these results, we conclude that the diamines have an important role in the increase of CO_2 permeability and that this is likely related to the unique CO_2 cooperative adsorption behavior. We further speculate that selectivities could increase in real operating

conditions, for example, in a mixed-gas environment. Indeed, under pure N_2, the transport is unaffected by CO_2 in the pore and we may expect higher N_2 permeability. Under a CO_2 environment, CO_2 can still transport down the channel while N_2 may be excluded due to the carbamate formation that effectively reduces the pore volume. We note that in absolute terms other polymers (e.g., polymers of intrinsic microporosity or thermally-rearranged polymers) can achieve superior performance in terms of CO_2 permeability, although their lack of stability over time has been a serious concern, preventing their use in industrial applications.[19,20] MMMs are generally less susceptible to aging, and MOF nanocrystal–polymer composite membranes are resistant to plasticization.[21] Moreover, CO_2 adsorption is not affected by humidity in the amine-appended adsorbents,[19] unlike what is observed in metal–organic frameworks with bare metal sites.[20,22]

I reasoned that the presence of diamines in these phase-change MOF fillers could influence CO_2 and N_2 transport through several mechanisms, and the results presented here lend some insight into the relative impact of each. With diamines present in the MOF channel, the free diffusion of both gases is restricted due to the decrease in free volume relative to the bare framework. On the other hand, with diamines present CO_2 is chemisorbed strongly and selectively through the cooperative formation of ammonium carbamate chains; weak physisorption of either gas is still possible. Comparing the pressures used in the permeability measurements to the room-temperature CO_2 adsorption isotherm for a sample of mmen-Mg_2(dobpdc) nanorods suggests that ammonium carbamate formation should be highly favored throughout the membrane, since even the lower downstream pressure rapidly exceeds the 1 mbar adsorption threshold during the measurement. Because CO_2 saturation is measured at equilibrium, an increase in solubility, rather than diffusivity, more likely explains the increase in permeability. A detectable increase in solubility during steady-state permeability measurements suggests fast exchange between carbamate CO_2 and mobile CO_2 in the pores. To our knowledge, the kinetics of this exchange is not yet well understood, and our results thus motivate further study of the CO_2 dynamics in this system. A classical model of facilitated transport[23] captures some aspects of this system, but does not adequately describe the cooperative uptake. As N_2 does not participate in cooperative adsorption, its permeability is less dependent on the MOF chemical functionality and generally trends with free volume, which should be higher in the MMMs. Interestingly, the modest increase in selectivity upon the addition of diamines may be related to diamine pore-blocking impeding N_2 transport.

3.11 Conclusion

As further theoretical studies aimed at understanding out-of-equilibrium kinetics of CO_2 adsorption/desorption along the diamines emerge, our work presents the first validated guidepost as to their significance in phase-change MMM design rules. Our insights in that regard benefitted from pinhole free composites, which were only available when the particle dimensions were scaled to nanoscopic dimensions, introducing along the way a novel synthesis of Mg_2(dobpdc) nanorods based on kinetic control over the reaction coordinate. Our phase-change MMMs, when tested for CO_2/N_2 separation, yielded a 2-fold improvement in the CO_2 permeability, as well as a similarly high CO_2/N_2 selectivity, boding well for other membrane-based gas separations where the selector incorporates phase-change fillers.

3.12 Methods

3.12.1 Materials

Cobalt oxide (99.998% trace metals basis) was purchased from Alfa Aesar, while magnesium oxide (99% trace metal basis, ~325 mesh), zinc oxide (99.0% (KT)), manganese oxide (99.99% trace metals basis), and nickel oxide (99.99% trace metals basis) were purchased from Sigma-Aldrich. All the other chemicals, reagents, and solvents were purchased from Sigma-Aldrich and used as received without further purification.

3.12.2 Methods

Brunauer–Emmett–Teller (BET) Surface Area Measurements

Dry, freshly activated MOF samples were transferred to a preweighed glass sample tube under nitrogen atmosphere. In a typical experiment, 40 mg of adsorbent were loaded into a Micromeritics TriStar II, put under vacuum (<10 mTorr) and cooled to 77 K. The adsorption measurement was performed using N_2.

CO_2 Adsorption Measurements

mmen-Mg_2(dobpdc) was activated and transferred to a Micrometric ASAP 2020 instrument. Pressure range for CO_2 introduced was 0–1 bar.

SEM

Images were obtained with a Zeiss Gemini Ultra-55 analytical scanning electron microscope equipped with secondary electron detectors at beam energy of 3 keV. Samples were deposited onto silicon wafers from a dispersion of M_2(dobpdc) in methanol; loaded substrates were dried in air prior to imaging.

XRD

Spectra were recorded in air on a Bruker Gadds-8 diffractometer with either a Cu–Kα source operating at 40 kV and 20 mA or a Co-Kα source operating at 35 kV and 40 mA.

Thermogravimetric Analysis (TGA)

Data were acquired on a TA Q5000 thermogravimetric analyzer. In a typical experiment, 2.5 mg of dry mmen-Mg_2(dobpdc) were loaded into an Al pan. The sample weight variation was recorded linearly ramping its temperature from RT to 600 °C at a rate of 5 °C min^{-1} under a constant Ar flux of 25 mL min^{-1}.

Mixed-Matrix Membrane Preparation

For each membrane, 6FDA-DAM (50 mg) was dissolved in dichloromethane (2 mL) and the solution filtered using a glass syringe filter (1-μm cut-off). Subsequently, a dispersion of nano mmen-Mg_2(dobpdc) in toluene (100 μL, 115 mg mL^{-1}) was added to the polymer solution. The MOF loading in the membrane was therefore estimated to be 23% by mass. The mixture was probe-sonicated for 4 min, immediately cast in a Teflon well, and left to dry overnight. The membrane was then peeled off and the thickness measured.

Permeation Measurements

Gas permeation measurements were conducted on using custom-built apparatus. Membrane thickness was determined using a depth gauge. Samples were affixed to brass shim S10 stock disks using impermeable polydimethylsiloxane (PDMS) glue. The remaining membrane area exposed to gas permeation was measured using a scanner. Samples were loaded into a stainless-steel filter holder (Millipore XX4502500). For bare Mg_2(dobpdc)/6FDA-DAM membranes, the film was heated at 180 °C in-situ under dynamic vacuum for ~12 h using heating tape. Before permeation tests, the system was held under static vacuum and the leak rate into the downstream volume was determined. This leak rate was then subtracted from permeation rates, and was always <1% of the permeation rate. N_2 permeation was measured prior to CO_2 on each sample to ensure no plasticization effects are observed. Uncertainty in gas permeability is determined from the propagation of uncertainty of membrane thickness, area, temperature, and upstream pressure.

3.12.3 Synthesis

4,4′-Dihydroxy-(1,1′-biphenyl)-3,3′-dicarboxylic Acid (H_4(dobpdc))

H_4(dobpdc) was synthesized using a previously reported procedure.[7] Briefly, 4,4′-dihydroxybiphenyl (1.16 g, 6.24 mmol), $KHCO_3$ (2.00 g, 20.0 mmol), solid CO_2 (4.2 g), and 1,2,4-trichlorobenzene (3 mL) were added to a PTFE insert within a 20 mL steel pressure reactor and heated at 255 °C for 17 h. After cooling to room temperature, the mixture was rinsed with diethyl ether and filtered. The collected solid was suspended in distilled water (300 mL) and again filtered. To the filtrate, conc. HCl was added dropwise until pH 2 was reached. The resulting crude product was collected by filtration. The material was recrystallized overnight at 4 °C in 50 mL of acetone and 50 mL of water per gram of crude material. ^{1}H NMR (500 MHz, DMSO-d_6): δ = 14.40–13.90 (br, 2H) 11.20–11.30 (br, 2H), 7.97 (d, 2H, J = 2.4 Hz), 7.80 (dd, 2H, J = 8.6 Hz, J = 2.4 Hz), 7.05 (d, 2H, J = 8.6 Hz).

M_2(dobpdc) (M = Zn, Mg, Mn, Co, Ni) from Commercial MO Powders

A 4 mL dram vial was charged with DMF (0.20 mL) and H_4(dobpdc) (27.4 mg, 0.1 mmol). The vial was heated to 120 °C in a thermally insulating aluminum block allowing for complete dissolution of the ligand, resulting in an initial ligand concentration of $[H_4(dobpdc)]_0$ = 0.50 M. The desired MO powder (0.2 mmol) was then added, and the reaction mixture maintained at 120 °C for a defined reaction time: 10 min for Mg_2(dobpdc), 1 h for Zn_2(dobpdc), 3 h for Co_2(dobpdc), 3 h for Mn_2(dobpdc), and 20 h for Ni_2(dobpdc). After cooling the reaction mixture, an additional portion of DMF was added, and the product isolated after centrifugation of the crude M_2(dobpdc) solids. The solids were further washed with DMF (2×) and then methanol (3×). M_2(dobpdc) solids were activated under dynamic vacuum (<20 μTorr) at 250 °C for 12 h. Porosimetry measurements were carried out immediately after activation, reducing to a minimum the MOF's exposure to air. Attempts to yield Fe_2(dobpdc) and Cu_2(dobpdc) from FeO and CuO commercial powders were not immediately successful using these reaction conditions.

Insertion of *N*,*N*′-Dimethylethylenediamine (mmen) in Mg_2(dobpdc)

Fully activated Mg_2(dobpdc) (30 mg) was immersed in 10 mL of anhydrous hexane containing *N*,*N*′-dimethylethylenediamine (1 mL). After 4 h, excess mmen-Mg_2(dobpdc) was rinsed from the MOFs using fresh hexane, and the MOFs activated under dynamic vacuum at 100 °C for 4 h.

Synthesis of ZnO Nanocrystals

ZnO nanocrystals were synthesized following a previously reported procedure.[10] Briefly, to a 500 mL round-bottom flask, KOH (902 mg, 16 mmol) was dissolved in methanol (150 mL). The solution was heated to 60 °C while stirring and kept at this temperature for 30 min. Next, zinc acetate dihydrate (1.757 g, 8.0 mmol) in methanol (50 mL) was added and the temperature raised to 60 °C. The reaction was allowed to proceed for 2 h before quenching the reaction (i.e., by allowing the vessel to cool to RT). Colloidal ZnO NCs were precipitated by adding hexanes (5 volumetric equivalents) and isopropanol (1 volumetric equivalent). The ZnO solids were isolated by centrifugation. The NCs were redispersed in the minimal volume of methanol, and the above cleaning steps were repeated twice. To interchange the surface hydroxyls to organic surfactants, ZnO NCs were dispersed in chloroform (3 mL) containing oleylamine (375 μL) and oleic acid (121 μL) for 12 h before precipitating ligand-coated ZnO NCs using acetone. Excess ligand was removed from the final product by repeated (3×) precipitation (acetone) and redispersion (hexanes). Full characterization of these ~7 nm ZnO NCs is given in Figure 3.21a,e,f.

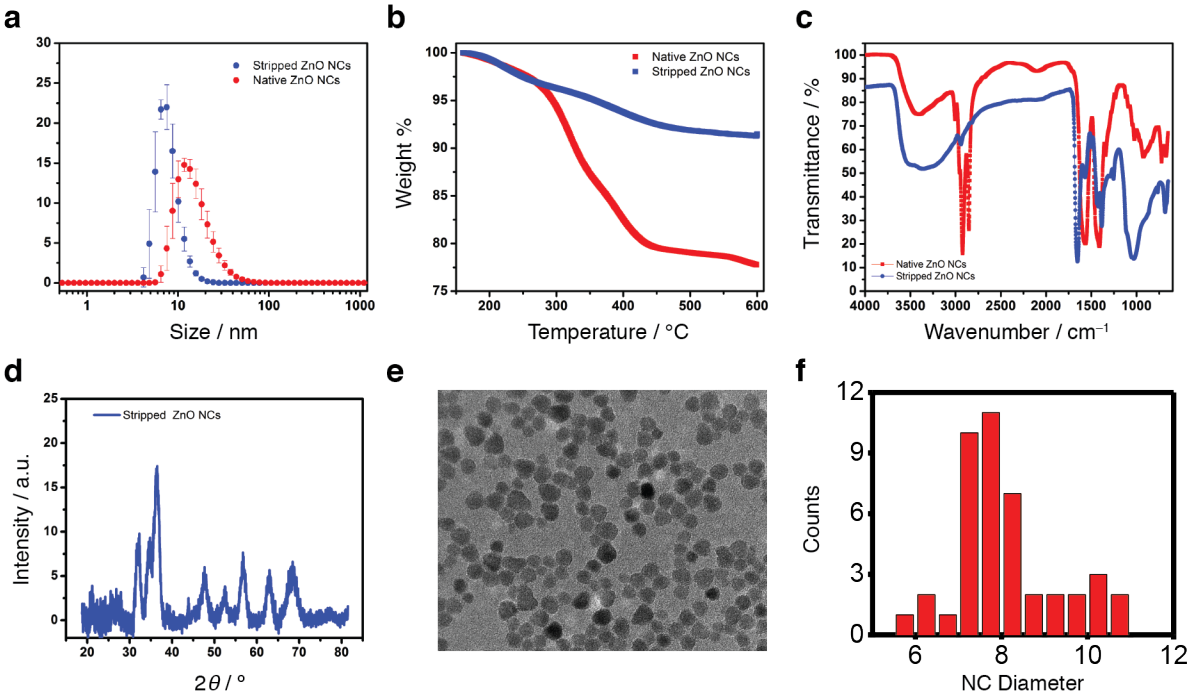

Figure 3.21 Characterization of ligand-coated (red curves) and ligand-stripped (blue curves) colloidal ZnO nanocrystals by a) dynamic light scattering, b) thermogravimetric analysis, and c) FT-IR. All highlight that the removal of native ligands is commensurate with smaller solvodynamic radius, and vanishingly low degree of contamination by residual organic surfactant. Additional characterization of the naked ZnO nanocrystals by d) XRD and e) transmission electron microscopy and f) associated size distribution.

Synthesis of CoO Nanocrystals

Cobalt oxide nanocrystals were synthesized using a slightly modified procedure reported elsewhere.[13] To a 150 mL 3-neck round-bottom flask was added solid hexadecylamine (HDA) (38.6 g, 160 mmol), which was subsequently melted upon heating at 70 °C. Cobalt acetylacetonate [$Co(acac)_2$] (514 mg, 2 mmol) was then added to the solvent melt, and the reaction mixture degassed at 100 °C for 1 h under dynamic vacuum. To grow the nanocrystals,

the reaction temperature was raised to 240 °C and kept at that temperature for 3 h before raising it to 260 °C for an additional 30 min. During heating, the initially pink solution turned purple and dark green; at this stage, the reaction mixture appeared turbid. The reaction mixture was quenched by rapid cooling using an air stream. CoO NCs prepared in this manner were cubic phase (confirmed by XRD, Figure 3.22c) with a size of ~9 nm (Figure 3.22d,e).

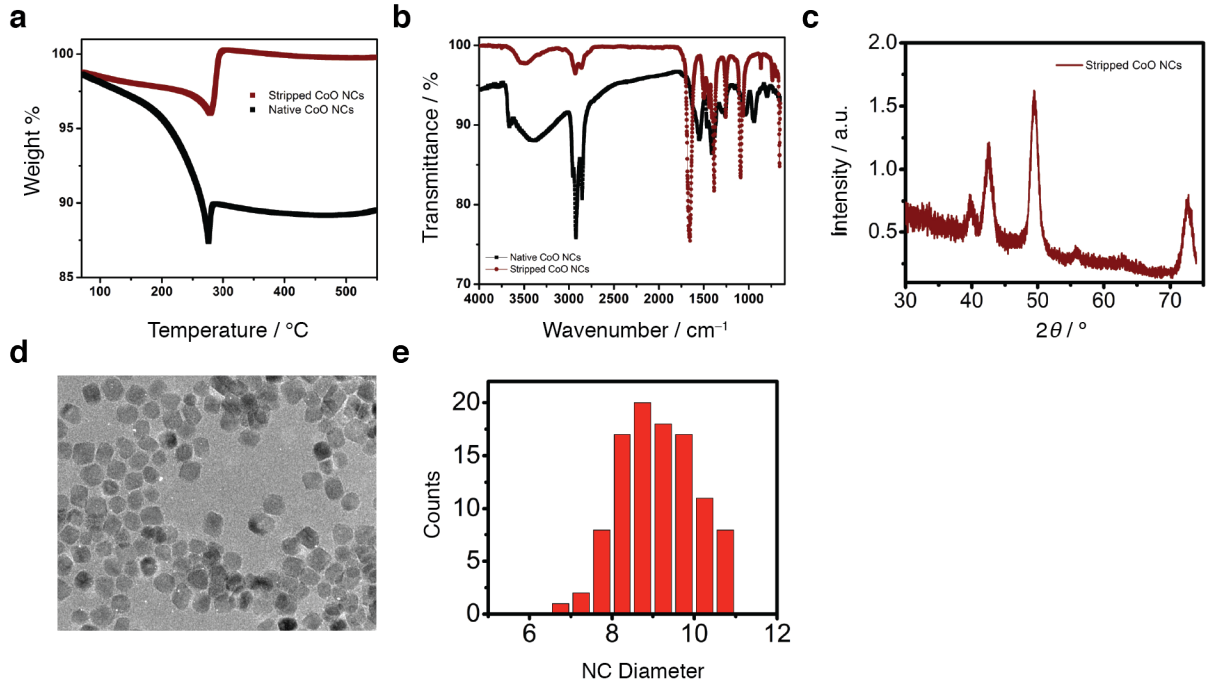

Figure 3.22 Characterization of ligand-coated (black curves) and ligand-stripped (wine curves) colloidal CoO nanocrystals by a) thermogravimetric analysis and b) FT-IR. Additional characterization of the naked CoO nanocrystals by c) XRD and d) transmission electron microscopy and e) associated size distribution.

Preparation of Naked MO Colloidal Nanocrystals

Nanocrystals were relieved of their coordinating organic ligands following a procedure previously developed by us.[10] Briefly, in a nitrogen glovebox, a dispersion of MO nanocrystals in hexanes (1 mL) was introduced to a glass vial containing DMF (1 mL) and BF_3:Et_2O (100 µL, 36% *w*/*w* in Et_2O) and toluene (7 mL). The ligand-stripped nanocrystals precipitated over a few min and were subsequently isolated by centrifugation and decanting (discarding) the supernatant. Further purification was carried out by several cycles of redispersion in DMF (1 mL), precipitation upon addition of hexanes/toluene (1:7, 8 mL), centrifugation (5 min), and decanting off the supernatant. Purified samples of naked NCs were dispersed in DMF to obtain a final concentration of 100 µmol mL^{-1}.

Zn_2(dobpdc) or Co_2(dobpdc) from Ligand-Stripped ZnO or CoO NCs

H_4(dobpdc) (27.4 mg, 100 µmol) in DMF (100 µL) was heated to 120 °C before adding naked ZnO or CoO NCs as a dispersion in DMF (100 µL, 100 µmol mL^{-1}). Aliquots were taken at 30 s, 1 min, 2 min, 5 min, 10 min, 30 min, and 1 h. Zn_2(dobpdc) or Co_2(dobpdc) thus produced were washed with DMF and methanol as described above prior to analysis.

3.12.4 Supplemental Figures

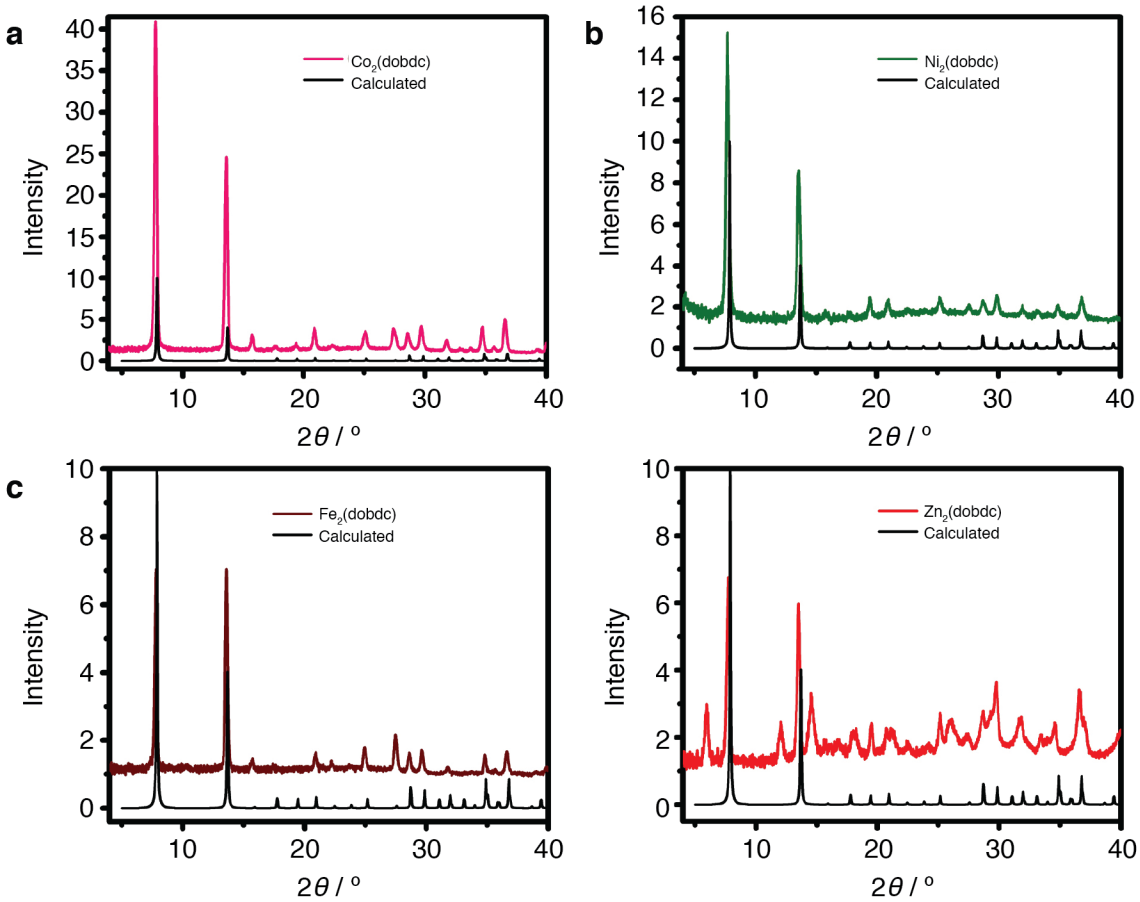

Figure 3.23 XRD patterns of M_2(dobdc) MOFs (i.e., MOF-74) synthesized from metal-oxide precursors: a) CoO; b) NiO; c) FeO; d) ZnO. Notably, M_2(dobdc) materials generated by this method are all pure phase except for the ZnO, which is polymorphic.

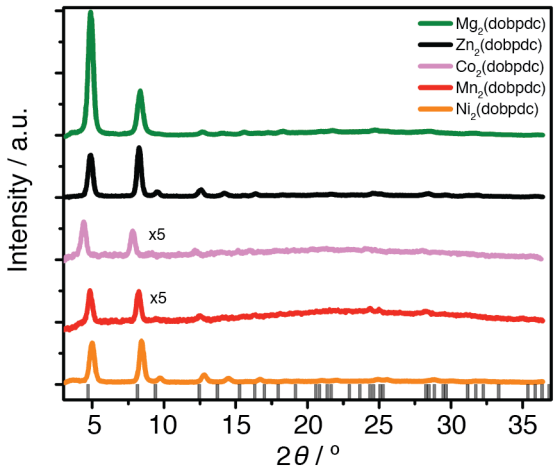

Figure 3.24 XRD patterns of M_2(dobpdc) MOFs obtained from metal-oxide precursors. Slight shifts in peak positions are due to residual solvent present in the 1D MOF channels.

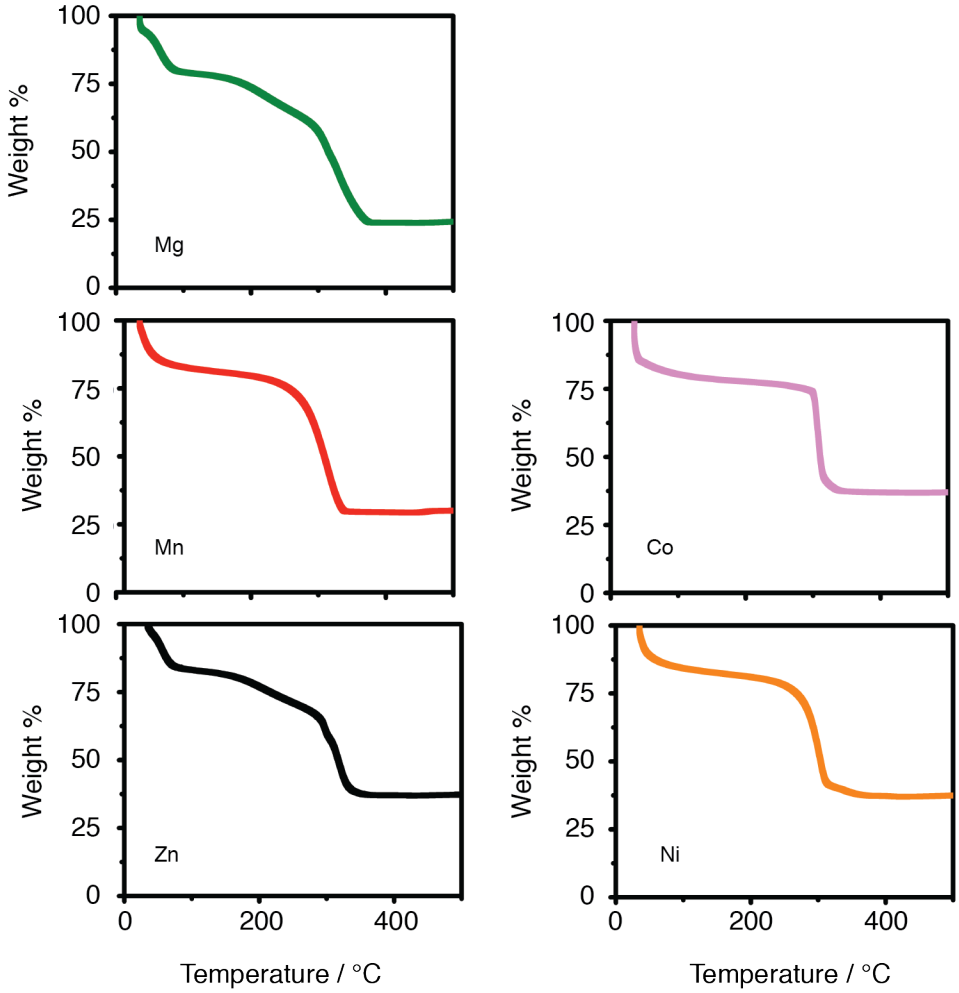

Figure 3.25 Thermogravimetric analysis of M_2(dobpdc) MOFs, each indicating MOF decomposition ~300 ºC, as previously observed.[4]

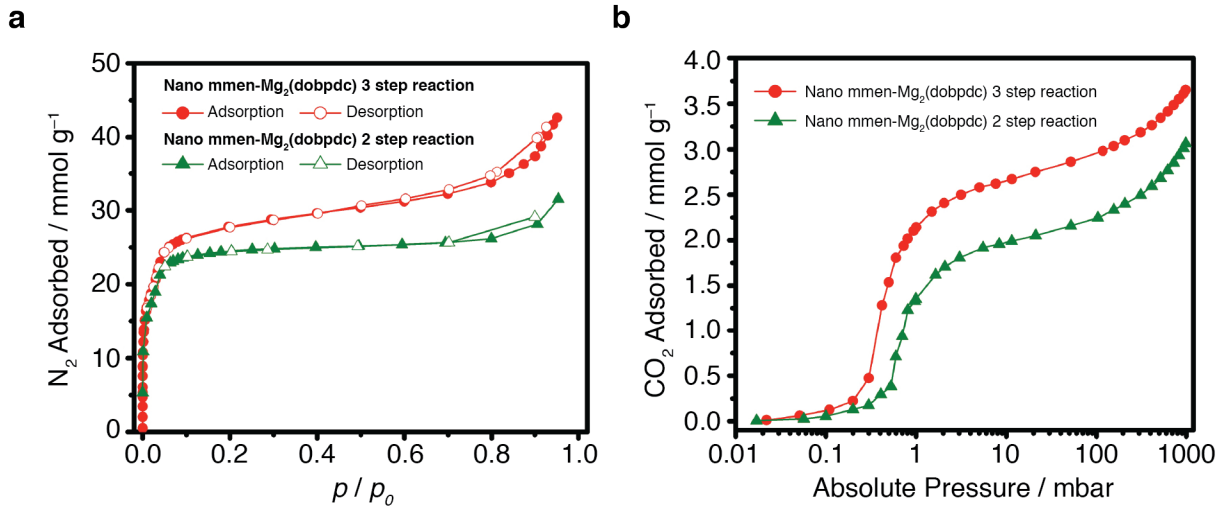

Figure 3.26 Comparison between pre- and post-ligand treatment on Mg_2(dobpdc) nanorods, shown in green and in red, respectively. a) N_2 adsorption/desorption curves at 77 K. Calculated BET surface areas are 2550 ± 64 m^2 g^{-1} and 2878 ± 75 m^2 g^{-1} for the 2- and 3- step procedure, respectively. b) CO_2 adsorption at 25 °C.

3.13 Acknowledgements

I would like to thank all of the coauthors responsible for making this work possible, including Lorenzo Maserati, Changyi Li, Jonathan Bachman, Jeffrey Long, and Brett Helms. We would also like to thank Wendy Queen, Daniel Sun, David Britt, and Thomas McDonald for helpful discussions as well as Teresa Williams and M. Virginia Altoe for assistance with TEM. This work was supported by the Center for Gas Separations Relevant to Clean Energy Technologies, an Energy Frontier Research Center funded by the U.S. Department of Energy, Office of Science, Basic Energy Sciences under Award #SC0001015. Portions of this work, including MOF synthesis, characterization, and composite processing, were carried out as a User Project at the Molecular Foundry, which is supported by the Office of Science, Office of Basic Energy Sciences, of the U.S. Department of Energy under Contract No. DE-AC02-05CH11231. B.A.H. acknowledges support from the Office of Science, Office of Basic Energy Sciences, of the U.S. Department of Energy under the same contract.

3.14 References

1. a) G. Dong, H. Li, V. Chen, *J. Mater. Chem. A* **2013**, *1*, 4610; b) D. Bastani, N. Esmaeili, M. Asadollahi, *J. Ind. Eng. Chem.* **2013**, *19*, 375.
2. a) N. Rangnekar, N. Mittal, B. Elyassi, J. Caro, M. Tsapatsis, *Chem. Soc. Rev.* **2015**, *44*, 7128; b) W. J. Koros, C. Zhang, *Nat. Mater.* **2017**, *16*, 289; c) B. Ghalei, K. Sakurai, Y. Kinoshita, K. Wakimoto, A. P. Isfahani, Q. Song, K. Doitomi, S. Furukawa, H. Hirao, H. Kusuda, S. Kitagawa, E. Sivaniah, *Nat. Energy* **2017**, *2*, 17086.
3. B. Seoane, J. Coronas, I. Gascon, M. E. Benavides, O. Karvan, J. Caro, F. Kapteijn, J. Gascon, *Chem. Soc. Rev.* **2015**, *44*, 2421.
4. T. M. McDonald, J. A. Mason, X. Kong, E. D. Bloch, D. Gygi, A. Dani, V. Crocella, F. Giordanino, S. O. Odoh, W. S. Drisdell, B. Vlaisavljevich, A. L. Dzubak, R. Poloni, S. K. Schnell, N. Planas, K. Lee, T. Pascal, L. F. Wan, D. Prendergast, J. B. Neaton, B. Smit, J. B. Kortright, L. Gagliardi, S. Bordiga, J. A. Reimer, J. R. Long, *Nature* **2015**, *519*, 303.
5. a) T. M. McDonald, W. R. Lee, J. A. Mason, B. M. Wiers, C. S. Hong, J. R. Long, *J. Am. Chem. Soc.* **2012**, *134*, 7056; b) W. S. Drisdell, R. Poloni, T. M. McDonald, T. A. Pascal, L. F. Wan, C. D. Pemmaraju, B. Vlaisavljevich, S. O. Odoh, J. B. Neaton, J. R. Long, D. Prendergast, J. B. Kortright, *Phys. Chem. Chem. Phys.* **2015**, *17*, 21448; c) D. Wu, T. M. McDonald, Z. Quan, S. V. Ushakov, P. Zhang, J. R. Long, A. Navrotsky, *J. Mater. Chem. A* **2015**, *3*, 4248; d) B. Vlaisavljevich, S. O. Odoh, S. K. Schnell, A. L. Dzubak, K. Lee, N. Planas, J. B. Neaton, L. Gagliardi, B. Smit, *Chem. Sci.* **2015**, *6*, 5177; e) M. Hefti, L. Joss, Z. Bjelobrk, M. Mazzotti, *Faraday Discuss.* **2016**, *192*, 153.
6. T. Chalati, P. Horcajada, R. Gref, P. Couvreur, C. Serre, *J. Mater. Chem.* **2011**, *21*, 2220.
7. T. M. McDonald, W. R. Lee, J. A. Mason, B. M. Wiers, C. S. Hong, J. R. Long, *J. Am. Chem. Soc.* **2012**, *134*, 7056.
8. a) J. Reboul, S. Furukawa, N. Horike, M. Tsotsalas, K. Hirai, H. Uehara, M. Kondo, N. Louvain, O. Sakata, S. Kitagawa, *Nat. Mater.* **2012**, *11*, 717; b) E. Zanchetta, L. Malfatti, R. Ricco, M. J. Styles, F. Lisi, C. J. Coghlan, C. J. Doonan, A. J. Hill, G. Brusatin, P. Falcaro, *Chem. Mater.* **2015**, *27*, 690.
9. E. G. Prout, F. C. Tompkins, *Trans. Faraday Soc.* **1944**, *40*, 488.
10. S. E. Doris, J. J. Lynch, C. Li, A. W. Wills, J. J. Urban, B. A. Helms, *J. Am. Chem. Soc.* **2014**, *136*, 15702.

11. a) A. Dong, X. Ye, J. Chen, Y. Kang, T. Gordon, J. M. Kikkawa, C. B. Murray, *J. Am. Chem. Soc.* **2011**, *133*, 998; b) E. L. Rosen, R. Buonsanti, A. Llordes, A. M. Sawvel, D. J. Milliron, B. A. Helms, *Angew. Chem. Int. Ed.* **2012**, *51*, 684.
12. a) W. Lin, J. W. Rieter, K. M. L. Taylor, *Angew. Chem. Int. Ed.* **2009**, *48*, 650; b) A. M. Spokoyny, D. Kim, A. Sumrein, C. A. Mirkin, *Chem. Soc. Rev.* **2009**, *38*, 1218; c) S. M. Meckler, C. Li, W. L. Queen, T. E. Williams, J. R. Long, R. Buonsanti, D. J. Milliron, B. A. Helms, *Chem. Mater.* **2015**, *27*, 7673.
13. Y. Li, M. Afzaal, P. O'Brien, *J. Mater. Chem.* **2006**, *16*, 2175.
14. a) Y. Chen, E. Johnson, X. Peng, *J. Am. Chem. Soc.* **2007**, *129*, 10937; b) T. D. Schladt, T. Graf, W. Tremel, *Chem. Mater.* **2009**, *21*, 3183; c) J. Ning, G. Xiao, L. Wang, B. Zou, B. Liu, G. Zou, *Nanoscale* **2011**, *3*, 741.
15. a) O. M. Yaghi, M. O'Keeffe, N. W. Ockwig, H. K. Chae, M. Eddaoudi, J. Kim, *Nature* **2003**, *423*, 705; b) O. Shekhah, H. Wang, D. Zacher, R. A. Fischer, C. Wöll, *Angew. Chem. Int. Ed.* **2009**, *48*, 5038; c) G. Férey, M. Haouas, T. Loiseau, F. Taulelle, *Chem. Mater.* **2014**, *26*, 299.
16. J. N. Weiss, *FASEB J.* **1997**, *11*, 835.
17. T. H. Bae, J. R. Long, *Energy Environ. Sci.* **2013**, *6*, 3565.
18. L. M. Robeson, *J. Membr. Sci.* **2008**, *320*, 390.
19. J. A. Mason, T. M. McDonald, T. H. Bae, J. E. Bachman, K. Sumida, J. J. Dutton, S. S. Kaye, J. R. Long, *J. Am. Chem. Soc.* **2015**, *137*, 4787.
20. N. C. Burtch, H. Jasuja, K. S. Walton, *Chem. Rev.* **2014**, *114*, 10575.
21. J. E. Bachman, Z. P. Smith, T. Li, T. Xu, J. R. Long, *Nat. Mater.* **2016**, *15*, 845.
22. J. Kundu, T. Pascal, D. Prendergast, S. Whitelam, *Phys. Chem. Chem. Phys.* **2016**, *18*, 21760.
23. E. L. Cussler, R. Aris, A. Bhown, *J. Membr. Sci.* **1989**, *43*, 149.

Chapter 4

Sub-Micron Polymer-Zeolitic Imidazolate Framework Layered Hybrids via Controlled Chemical Transformation of Naked ZnO Nanocrystal Films

4.1 Introduction

A hybrid material can exhibit functional properties greater than the sum of its parts when its components are chosen and arranged rationally.[1] Assembling such a composite requires attention to the chemistry, size, and morphology of each component. Furthermore, controlling composite architecture necessitates consideration of the interfaces between these components. While there are many examples of functional composites with a dispersed phase in a host matrix (e.g., mechanically reinforced polymer composites,[2] composite electrodes for electrochemical devices,[3] and switchable photonic displays[4]), those with layered architectures are fewer and are often more difficult to fabricate. This is the case with ZIF–polymer composites, where producing layered composites is more time-consuming and less controllable than the formation of mixed-matrix composites.[5,6-8]

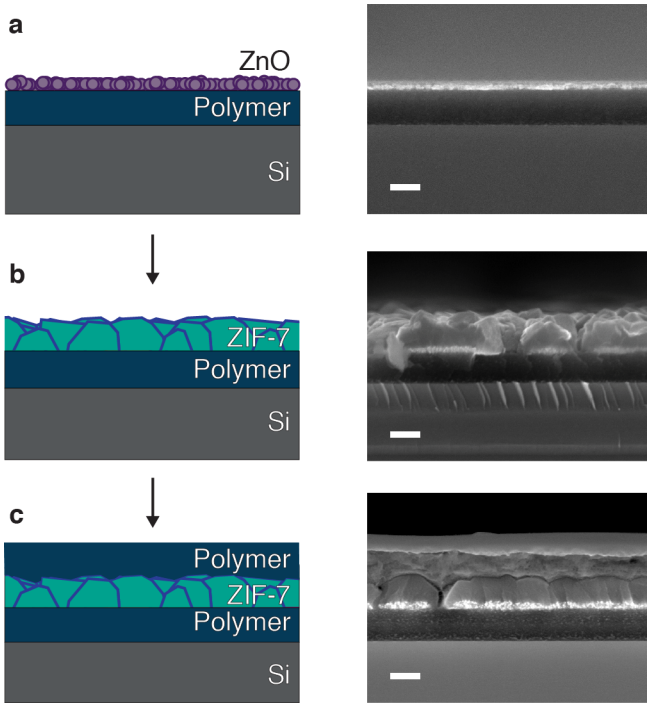

Figure 4.1 Scheme and cross-sectional SEM images depicting a) ZnO nanocrystals on a polymer film, b) a ZIF-7 film grown from sacrificial ZnO nanocrystals, and c) a PIM/ZIF-7/PIM trilayer structure. Scale bars are 200 nm.

Here I show that sub-micron-thick ZIF films can be grown in a controllable manner via a ZnO-to-ZIF dissolution–crystallization scheme carried out on polymers of intrinsic microporosity (PIMs), yielding layered microporous composites for the first time (Figure 4.1). ZIFs are robust materials demonstrating great promise in a variety of applications including separations, catalysis, sensing, and electronics.[7, 9] The ultrathin films reported here are especially promising for asymmetric membranes, where thin selective layers provide high selectivity without sacrificing flux. The morphology of these ZIF films on polymer is strongly influenced by the reaction conditions used to convert nanocrystalline ZnO to either ZIF-7 or ZIF-8, highlighting the deterministic role solvent plays on ZnO dissolution as well as ZIF nucleation and growth. The unique layered architecture made possible by these synthetic advances required me to apply synchrotron X-ray techniques to understand the structure and composition of the composite in a quantitative manner. Through the use of these techniques, I was able to directly probe the nanoscale ZIF films rather than relying on the products of analogous bulk reactions.

My implementation of cationic naked ZnO nanocrystals as precursors to sub-micron-thick ZIF films is unique and overcomes several challenges previously encountered with direct growth methods from solution-phase precursors. In those cases, ZIF films with thicknesses of microns or even tens of microns are more common.[5,10,11] Thinner films, which help shorten molecular diffusion paths, generally require multistep layer-by-layer strategies (e.g., SURMOFs), and while 100 nm ZIF-8 films have been grown solvothermally on glass and silicon, extending this technique to polymers frequently requires substrate modification.[11,12,13] In my scheme, I limit the total Zn(II) available for ZIF formation simply by controlling the ZnO nanocrystal film thickness, and as the ZIF growth is directed by the ZnO nanocrystal layer, no

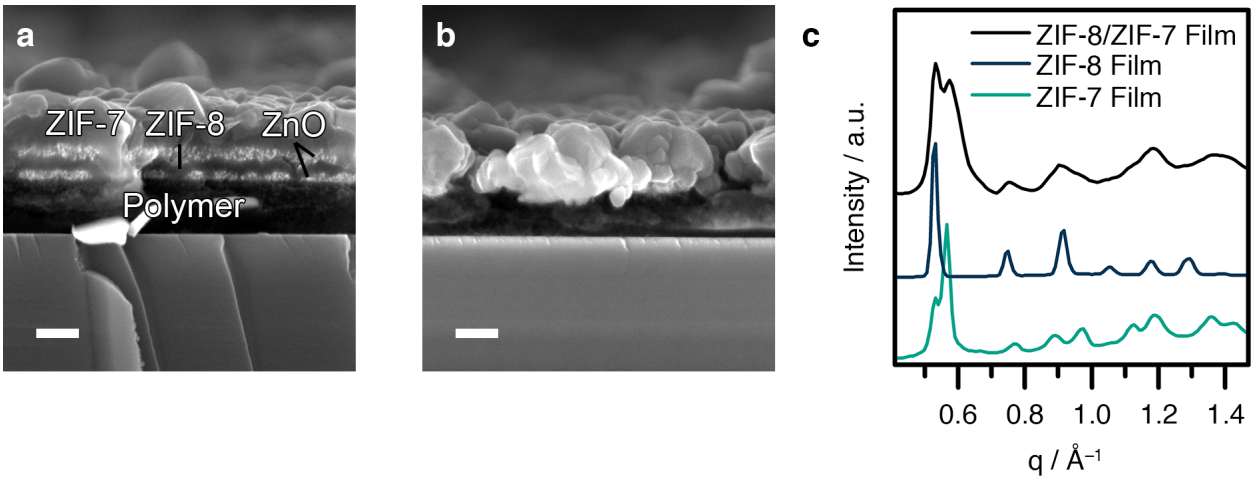

Figure 4.2 a) Cross-sectional SEM image of a layered composite comprised of PIM-1, ZIF-8, ZIF-7, and ZnO. The ZIF-7 layer was grown from ZnO nanocrystals deposited on a ZIF-8 coating. Scale bar is 200 nm. b) Cross-sectional SEM image of a ZIF-8/ZIF-7 composite film on PIM with little to no residual ZnO between the two ZIF layers. Scale bar is 200 nm. c) Grazing incidence X-ray diffraction (GIXD) patterns of the ZIF-8/ZIF-7 composite.

functionalization of the polymer is necessary. I also hypothesize that the high surface area inherent to these 0D nanostructures aids in conversion rate and efficacy. In that regard, my results are complementary to previous work reporting ZIF growth on nanoscopic ZnO and $Zn(OH)_2$ materials, which have been transformed into both 1D and 2D ZnO–ZIF or $Zn(OH)_2$–ZIF hybrids.[14,15-17] Metal oxides and hydroxides have also been used to grow other classes of porous crystals, including metal–organic frameworks (MOFs) via pseudomorphic replication.[18,19] Common to these schemes is the etching of the metal oxide or hydroxide by the ligand (i.e., dissolution) and subsequent nucleation and growth of the framework material (i.e., crystallization).

4.2 ZIF-PIM Composite Formation

I found that the conversion of cationic naked ZnO nanocrystal films (15–30 nm thick) to either ZIF-7 or ZIF-8 coatings (100–500 nm thick) on cross-linked films of PIM-1 (~200 nm thick) proceeded readily using a low-temperature microwave reaction (Figure 4.1a,b). Typically, I spin coated ~7 nm ZnO nanocrystals on a cross-linked polymer film atop a silicon substrate. I then submerged the nanocrystal-coated polymer film facedown in a solution of either

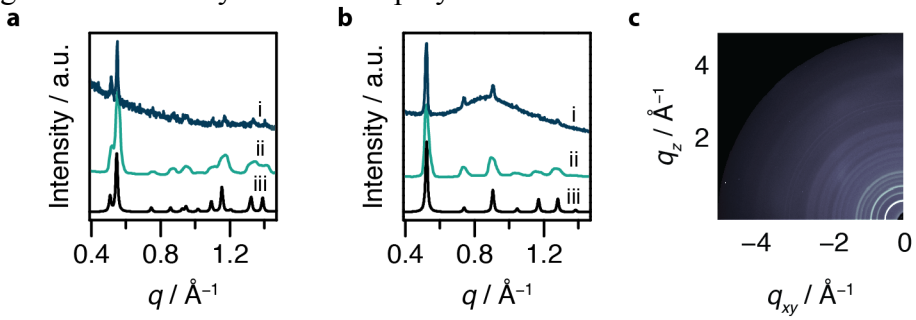

Figure 4.3 Diffraction patterns of a) ZIF-7 and b) ZIF-8 thin films on PIM-1 polymer supports, including i) PXRD, ii) GIXD, and iii) simulated diffraction patterns. c) The 2D GIXD patterns are fully isotropic, revealing no preferential crystal orientation with respect to the plane of the support.

benzimidazole or 2-methylimidazole in a water/DMF mixture ([imidazole ligand]$_0$ = 1.11 M) to induce transformation to ZIF-7 or ZIF-8, respectively. I subjected the vessel to microwave radiation without stirring to maintain an internal solution temperature of 50 °C for 30 min. Substrates were then retrieved and washed by dipping in a solvent bath (DMF for ZIF-7 films; deionized water for ZIF-8 films) to remove excess ligand. A sandwich structure with the ZIF between two layers of polymer was generated by spin-coating another layer of PIM-1 over the ZIF surface (Figure 4.1c). Unusual ZIF-8/ZIF-7 multilayers could also be prepared on cross-linked PIM-1 films through the sequential deposition and transformation of ZnO nanocrystal films with 2-methylimidazole and benzimidazole in turn (Figure 4.2). Notably, in no cases was surface modification of PIM-1 necessary to adhere the ZnO nanocrystals or ZIF films, where in previous work, amine functionalization of the polymer was needed to promote heterogeneous nucleation and adhesion of the ZIF.[13]

4.3 Structural Characterization of Composites

Using cross-sectional and top-down SEM, I studied the resultant film morphology. Contrast differences between residual ZnO nanocrystals and the overlying ZIF made each phase readily distinguishable. Crystalline ZIF-7 or ZIF-8 within the layered hybrid was detected using powder X-ray diffraction (PXRD) and synchrotron grazing incidence X-ray diffraction (GIXD) (Figure 4.3). GIXD patterns provided high signal-to-noise crystallographic identification with increased surface sensitivity, mitigating the overwhelming baseline from the amorphous polymer seen in the PXRD data.[20] This allowed me to directly collect diffraction patterns of ZIF on the polymer films. The 2D GIXD patterns were isotropic, revealing no preferential ZIF orientation with respect to the plane of the film (Figure 4.3c). To provide further insight into the fundamental steps in the present scheme, I explored in greater detail the reaction conditions that

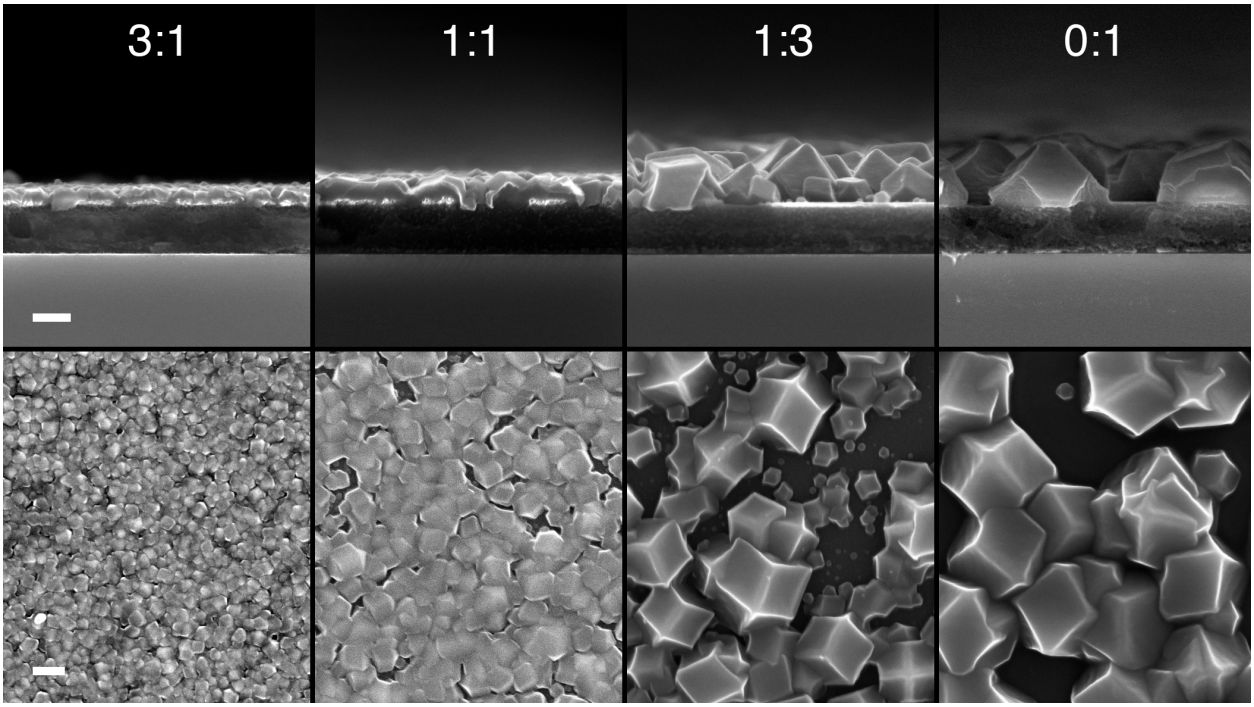

Figure 4.4 SEM images of ZIF-8 coatings transformed from 30 nm thick sacrificial ZnO films at various DMF:water (*v*/*v*) ratios. Both cross-sectional (top row) and top-down (bottom row) views are shown. Scale bars are 200 nm.

influenced ZIF film formation on PIM-coated substrates.

My systematic investigation of the reaction conditions used for the ZnO-to-ZIF-8 film transformation revealed significant control over film thickness and grain size with changes to the reaction solvent: here, mixtures of water and DMF (Figure 4.4). Other reaction parameters, including temperature, ligand concentration, and reaction time, were investigated but failed to both provide control over ZIF film growth and produce high-quality coatings. Transformations employing reaction mixtures up to 50 vol% water yielded comparatively smooth, continuous ZIF-8 films as thick as ~150 nm. The continuous nature of the films produced under these reaction conditions suggests the formation of many ZIF-8 nuclei and comparatively slow crystal growth. Unincorporated Zn(II) is presumed to be lost to solution or retained as residual ZnO trapped at the ZIF–polymer interface. If all the ZnO were successfully transformed, a 30 nm nanocrystal layer would produce a ~320 nm thick ZIF-8 film.[21] As the water content of the reaction mixture increased beyond 50 vol%, significantly less ZnO was visible in the cross-sectional SEM images and the ZIF-8 grain size increased. In these cases, the ZIF-8 coatings ceased to be continuous; instead, I observed the growth of faceted, isolated crystals

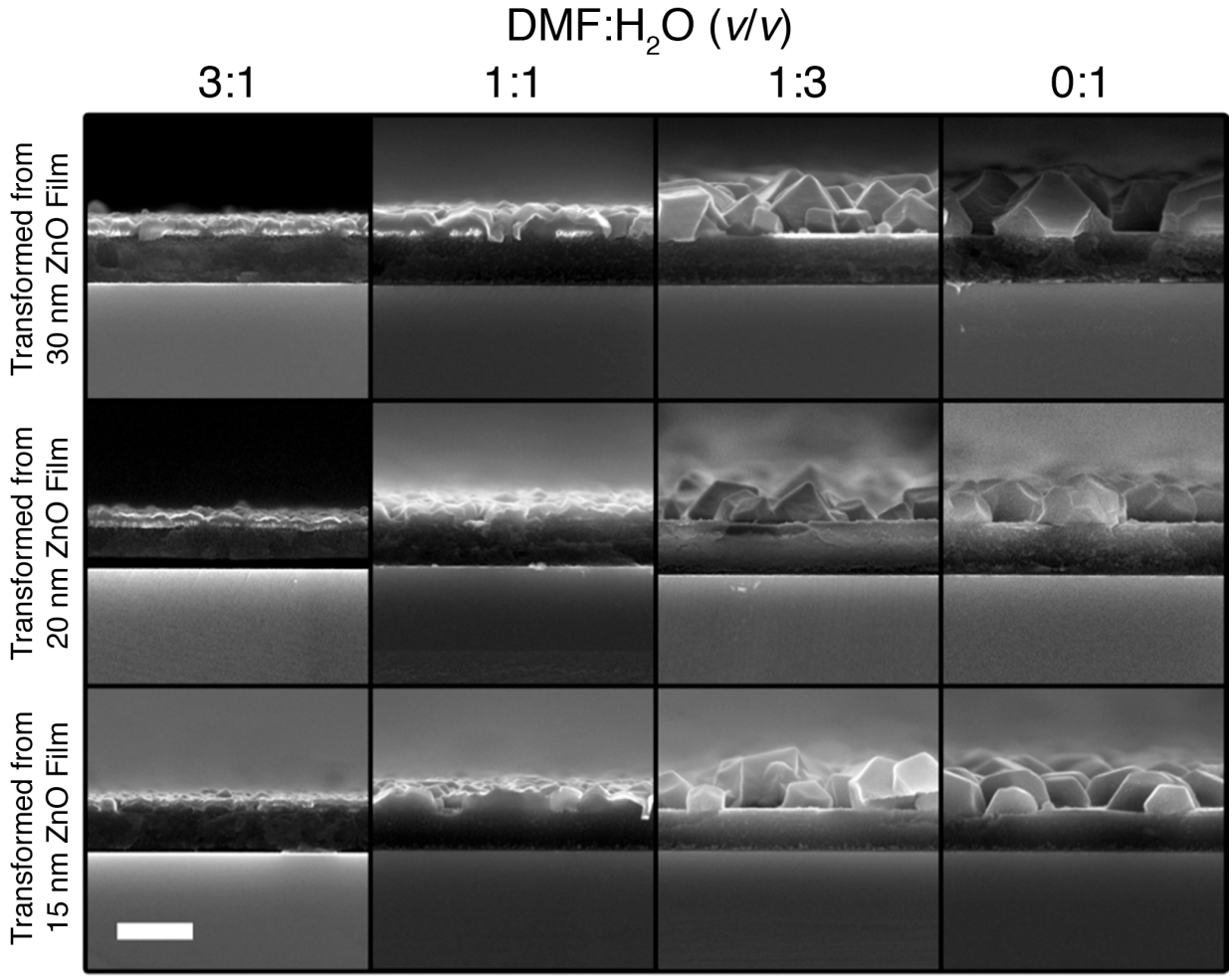

Figure 4.5 Cross-sectional SEM images of ZIF-8 coatings transformed from 30 nm (top row), 20 nm (middle row), and 15 nm (bottom row) thick ZnO nanocrystal films on PIM in various DMF:H2O (*v*/*v*) solutions. Scale bar is 400 nm.

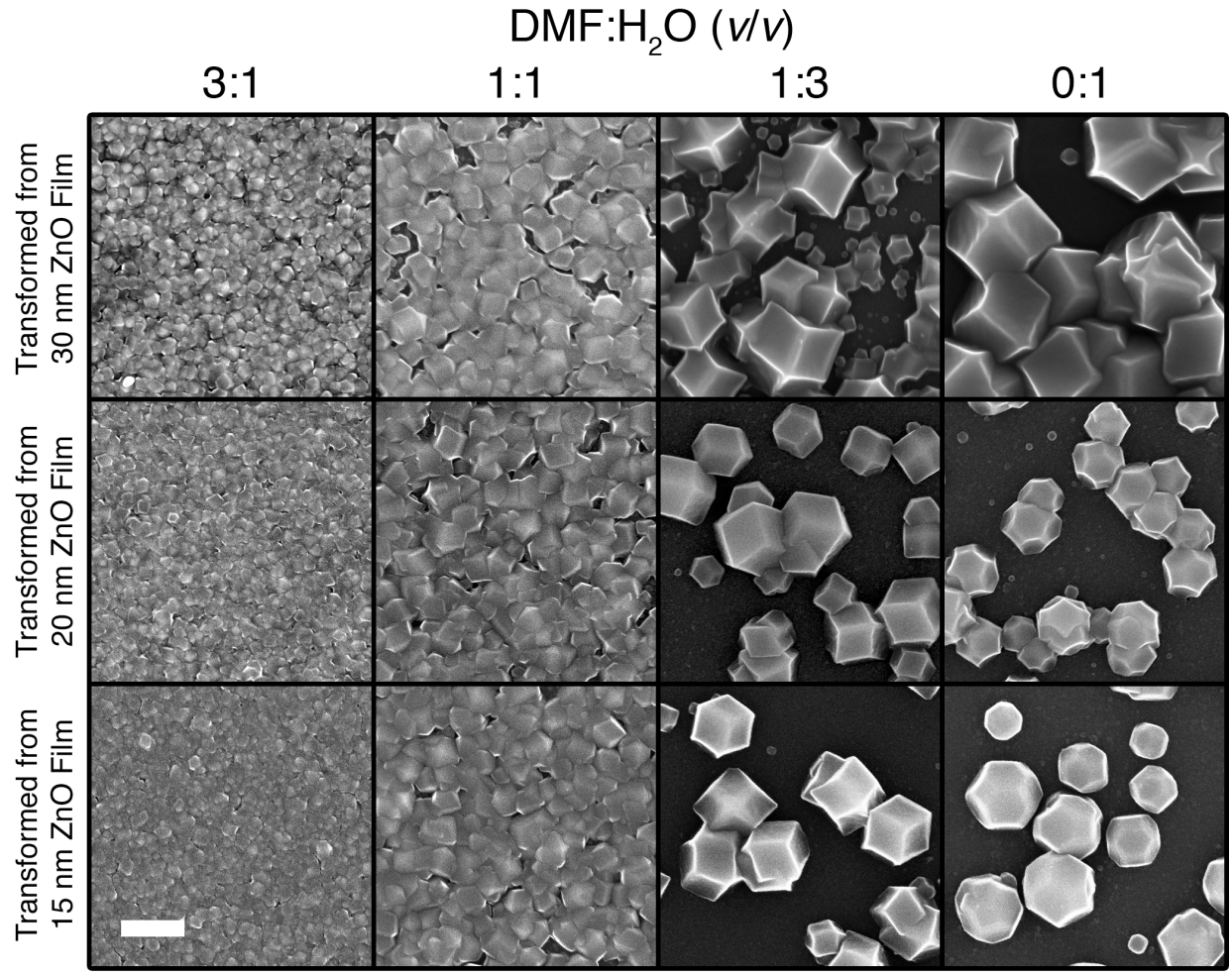

Figure 4.6 Top-down SEM images of ZIF-8 coatings transformed from 30 nm (top row), 20 nm (middle row), and 15 nm (bottom row) thick ZnO nanocrystal films on PIM in various DMF:H2O (*v*/*v*) solutions. Scale bar is 400 nm.

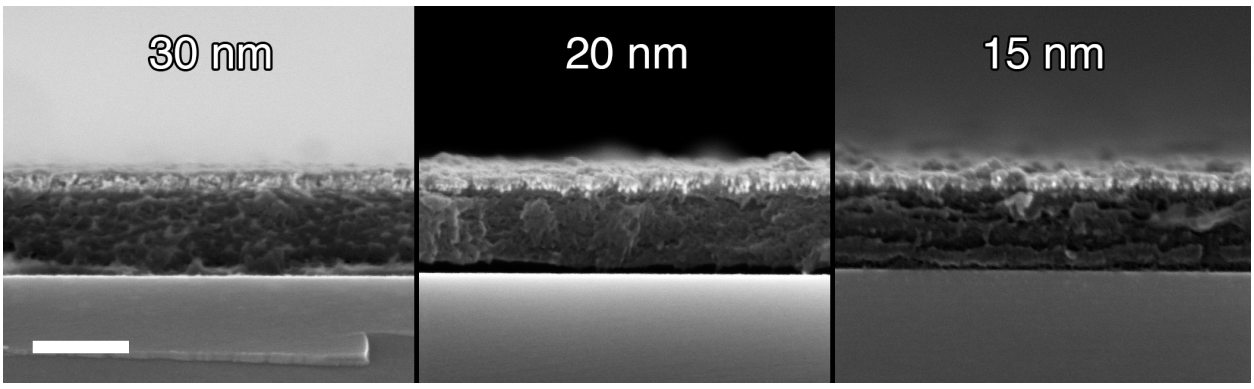

Figure 4.7 Cross-sectional SEM images of ZnO nanocrystal films of varying thicknesses on PIM. More exact thickness measurements were made impossible by the surface roughness, the amorphous carbon coating needed for SEM imaging, and slight heterogeneities in the polymer films. Scale bar is 200 nm.

adhered to the polymer surface. Reducing the thickness of the sacrificial ZnO layer only slightly changed the morphology of the ZIF coatings but resulted in significantly less residual ZnO in the SEM cross sections (Figures 4.5 and 4.6). I controlled ZnO nanocrystal film thicknesses by diluting the dispersion from which the films were cast and measured approximate ZnO film thicknesses using cross-sectional SEM (Figure 4.7). ZIF-8 coatings formed from even the thinnest ZnO precursor films fabricated. In most cases, the equilibrium rhombic dodecahedral ZIF-8 crystal morphology was observed rather than the kinetically favored cubic morphology.[22] Reactions in pure DMF were not reproducible, which I attribute to the ease with which naked ZnO nanocrystals redisperse in this solvent. As benzimidazole is sparingly soluble in water, an analogous study of the ZnO-to-ZIF-7 transformation is not included here.

4.4 Quantification of Residual ZnO Through X-Ray Absorption Spectroscopy

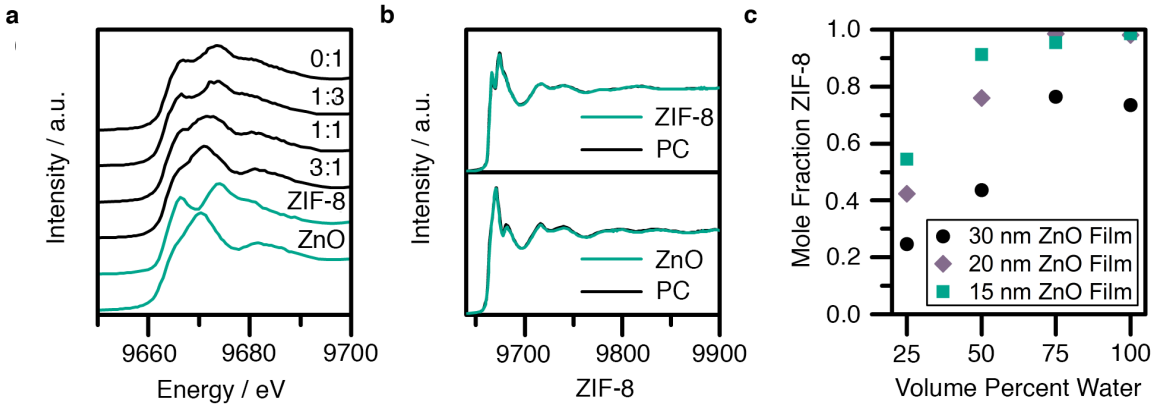

Figure 4.8 Quantitative XANES characterization of ZIF-8 films transformed from ZnO coatings at various DMF:water (*v*/*v*) ratios. a) Spectra of bulk ZnO and ZIF-8 (green) and of ZIF-8 films (black). b) The two principal components (PC) best expressing change in the experimental data set (black) match experimentally collected bulk ZIF-8 and ZnO spectra (green). c) Mole fraction of Zn in ZIF-8 after the chemical transformation of ZnO nanocrystal films (average film thickness = 15 nm, 20 nm, or 30 nm) using different solvent mixtures. These data can be taken as a measure of film purity with respect to ZIF and residual ZnO.

To quantify the purity of ZIF-8 layers produced in different solvent mixtures (i.e., with respect to any residual ZnO), I compared X-ray absorption near-edge structure (XANES) spectra of representative samples produced in four DMF:water mixtures were to reference spectra for ZnO nanocrystals and ZIF-8. XANES total fluorescence yield spectra of the Zn K-edge are well-suited to the analysis of our hybrid films: they are unaffected by the presence of the underlying PIM-1 film; the probe depth is micron scale; and the fluorescence intensities of Zn atoms in different electronic environments, here ZIF-8 and ZnO, are the same (see Experimental Section 4.7 for more information). I collected XANES spectra from each sample at multiple spots near the center of the film and averaged them together to faithfully represent the sample composition and to reduce beam damage on the ZIF-8 (Figure 4.8a). I performed principal component analysis (PCA) on the data set and compared the two principal components best expressing change in the data set against reference spectra taken of ZIF-8 and ZnO (Figure 4.8b). Both exhibit excellent agreement, suggesting the Zn content of the films can be accurately modeled as a mixture of only ZIF-8 and ZnO. Least-squares fits of the reference spectra to each experimental

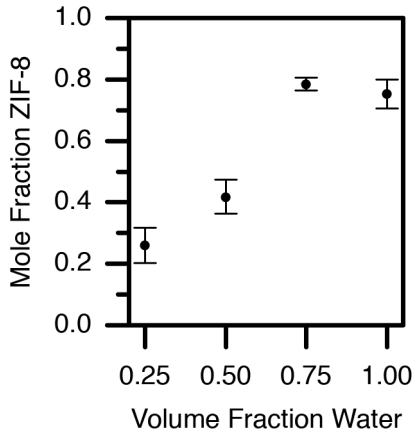

Figure 4.9 XANES fits for 30 nm ZnO films showing sample-to-sample variation. Analysis of Reported values are the mean of four samples at each condition, and the error bars, which represent standard error, demonstrate sample-to-sample reproducibility.

film provided a quantitative fraction of the total Zn present in each crystalline phase (Figure 8c). To demonstrate the reproducibility of sample preparation, the experiment was repeated for the 30 nm thick ZnO films three times, and in no case was the standard error greater than 8 mol% (Figure 4.9). The XANES fits reveal that as the volume fraction of water in the reaction medium increases and the thickness of the ZnO precursor film decreases, the films tend toward pure ZIF-8, which is in good agreement with the phenomenological interpretation of the SEM cross sections. I obtained continuous, nearly pure ZIF-8 coatings from 15 nm thick ZnO films transformed in 50 vol% water solutions (Figure 4.10).

4.5 Insights into the Metal Oxide-to-MOF Chemical Transformation Mechanism

While several metal oxide-to-MOF chemical transformations have been reported in the literature, the mechanism of this chemical conversion is still under investigation. Different metal oxide/ligand pairs and the conditions in which the reaction is carried out may change the mechanism of MOF formation.[15, 18] Clearly, the metal oxide-to-MOF conversion depends on the competing rates of several processes: (1) metal oxide dissolution, (2) metal-ion diffusion away from the polymer surface, (3) MOF nucleation (possibly from an amorphous precursor), (4) MOF growth, and (5) Ostwald ripening (Figure 4.11). The relative rates of these processes dictate the overall kinetics of the reaction and the resultant morphology and composition of the product.

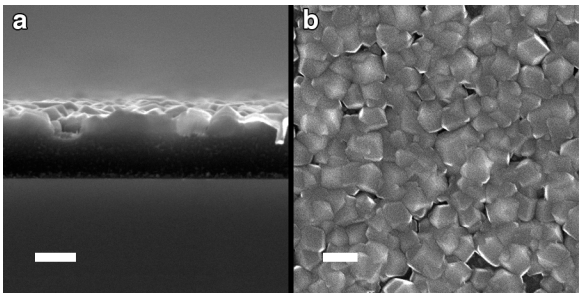

Figure 4.10 a) Cross-sectional SEM image of a ZIF-8 coating on PIM that is >90% pure with respect to residual ZnO. b) Top-down image of the same film shows significant surface coverage. Scale bars are 200 nm.

In the scheme presented here, water and DMF each affect these competing rates. The transforming solutions show an increase in pH with increasing water content, from pH 9 at 25

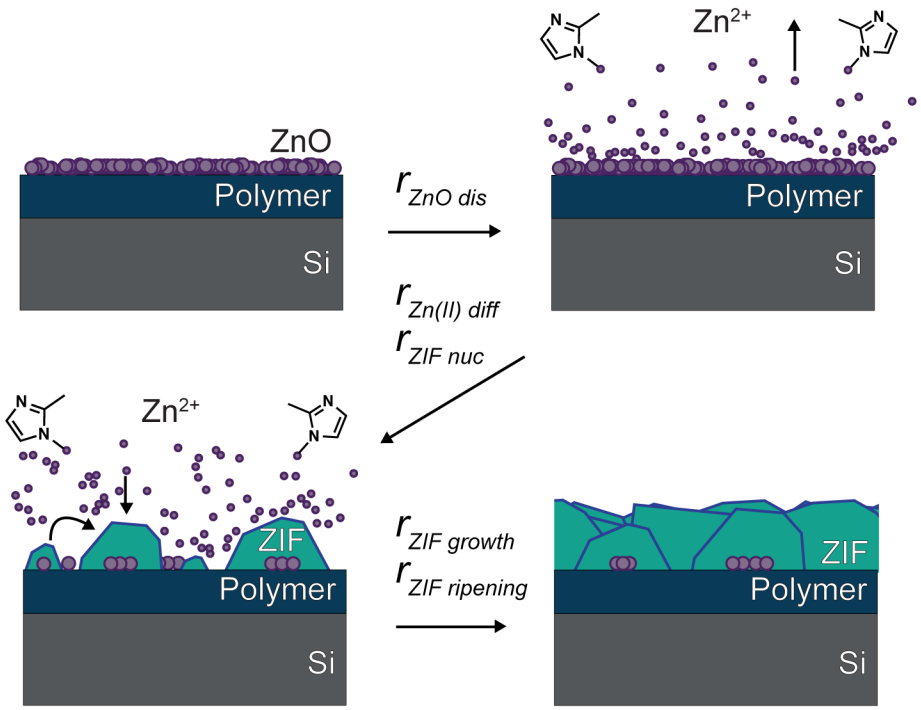

Figure 4.11 Scheme detailing the competitive processes determining the morphology and composition of ZIF coatings accessed via ZnO nanocrystal precursor films. The competing rates are 1) metal-oxide dissolution, 2) metal-ion diffusion away from the polymer surface, 3) ZIF nucleation, 4) ZIF growth, and 5) Ostwald ripening.

vol% water to pH 11 at 100 vol% water. Increasing the vol% of water therefore results in faster etching of the amphoteric ZnO, increased proton mobility overall, and more facile deprotonation of the ZIF crystal surfaces, which in turn promotes crystal growth over nucleation of new crystallites.[23] DMF, aside from regulating etching by modulating pH, may also be responsible for inhibiting ZIF growth as has been reported in some solvothermal ZIF-8 syntheses.[24] Finally, I considered whether differences in microwave absorption might affect the energy available to the system. However, since water and DMF have similar loss tangent values, both solvents can be expected to behave similarly under microwave radiation.[25]

As ZnO has been reported previously as an effective templating agent for the solvothermal growth of ZIF films, I reasoned that metal oxide may be necessary for a local ZIF nucleation event, consistent with a heterogeneous nucleation mechanism.[6,17,26] Phase-pure ZIF at the polymer surface was not measured in any of the XANES experiments when the initial ZnO film thickness was 30 nm. If ZnO is needed for heterogeneous nucleation, the voids between crystals due to rapid nanocrystal dissolution are concomitant with fewer nucleation sites in those regions on PIM-1. This is consistent with our observation that voids account for greater fractions of the surface area in films formed using high water content solutions, where ZnO dissolution is more rapid. ZIF coatings transformed from thinner ZnO films produced nearly pure ZIF-8 coatings, which may result from ZIF nucleation occurring directly at the polymer surface, presumably at the nitrile groups decorating the PIM-1 backbone.[27] However, we believe it is more likely the ZIF preferentially nucleates on ZnO nanocrystals that are subsequently etched via diffusion through the ZIF pores, a phenomenon previously reported in similar chemical conversions.[16]

Finally, studying the time-evolution of ZIF-8 film growth in a 75 vol% water solution provided further insight into the contributing and competing influences of ZIF-8 nucleation, growth, and Ostwald ripening (Figure 4.12). Large crystals, seen in films grown from 75 vol% or pure water solutions, form when nucleation is slow relative to crystal growth. Nucleation occurs as long as ZnO is exposed to the solution, and crystal growth stops when all accessible Zn(II) is depleted, explaining the increased ZIF-8 polydispersity observed in reactions with a high water content. After microwave irradiation for 10 min, few nucleation sites have formed and the surface is primarily ZnO. By 30 min, the surface ZnO is lost to solution, converted into ZIF-8, or covered by ZIF-8. The crystal size is static over longer reaction times, demonstrating that Ostwald ripening is likely not a significant factor in film formation and that the 30 min reaction time is sufficient to obtain the final film morphology.

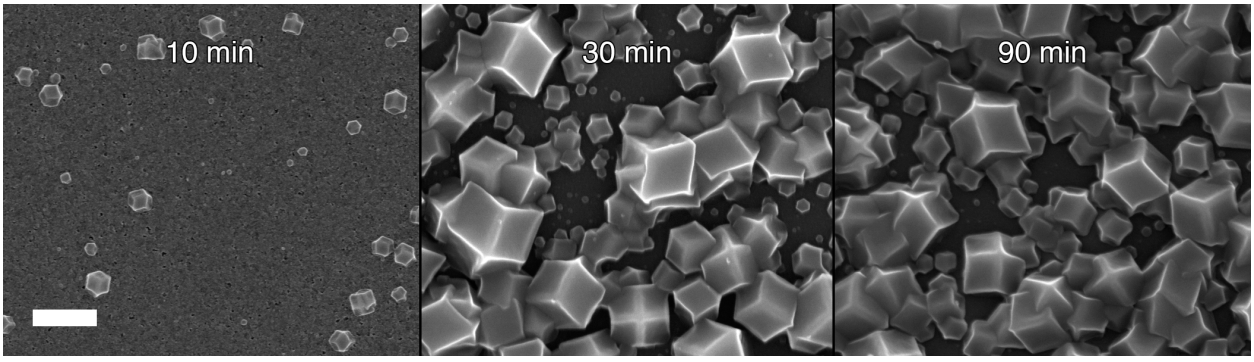

Figure 4.12 Top-down SEM images showing the time-evolution of ZIF-8 films grown from 30 nm thick ZnO nanocrystal films in 75 vol% water solutions. The slow appearance of ZIF-8 nuclei followed by rapid crystal growth is observed, suggesting ZIF-8 polydispersity is a result of different growth times before the Zn(II) source is consumed. The lack of morphological evolution after 30 min suggests Ostwald ripening is slow. Scale bar is 400 nm.

4.6 Conclusions

I obtained sub-micron ZIF-7 and ZIF-8 coatings and bilayers on microporous polymer substrates through the chemical conversion of naked ZnO nanocrystal precursor films. The high surface area of the nanocrystal films facilitated a rapid conversion under mild conditions to ZIF coatings with morphologies that I controlled by choice of solvent. I confirmed crystal structures by GIXD and measured the morphology and chemical composition of the ZIF-8 films formed under varying reaction conditions using SEM and XANES spectroscopy, respectively. Sub-micron-thick ZIF films encased on both sides by polymer and ZIF-8/ZIF-7 multilayers were accessible, demonstrating an attractive and versatile new methodology to fabricate layered composite architectures. These composite architectures may be well suited to applications in selective separations and sensing. In that the deposition of metal oxide nanocrystals within or on other materials is foreseeable, my techniques may also be applicable to ZIF–polymer composites in a variety of porous polymer formats, including hollow polymer fibers, polymer monoliths, polymer membranes, and polymer beads. My unique access to ZIF-on-ZIF multilayers likewise suggests new avenues for selective species transport.

4.7 Experimental Details

4.7.1 Materials

Zinc acetate dihydrate (99.999% or ≥99%), oleic acid (90%), tetrafluoroterephthalonitrile (99%), 5,5',6,6'-tetrahydroxy-3,3,3',3'-tetramethyl-1,1'-spirobisindane (96%), 2-methylimidazole (99%), benzimidazole (98%), 1,4-dioxane (≥99.0%) and chlorobenzene (98%, anhydrous) were purchased from Sigma Aldrich. Oleylamine (80–90%), boron trifluoride-etherate (BF_3-etherate, ca. 48% BF_3), and chloroform-d (>99.6%) were purchased from Acros Organics. Potassium hydroxide was purchased from BDH Chemicals, 2,6-Bis(4-azidobenzylidene)cyclohexanone (wetted with 30% water by weight, >90%) from TCI chemicals, and potassium carbonate (>99.9%) from Fischer Scientific. Benzimidazole solutions were passed through a 0.45 µm filter as needed to remove any insoluble contaminants; all other chemicals were used as received. N,N-dimethylformamide (DMF) used for PIM-1 synthesis and the ZnO to ZIF transformations was taken from a JC Meyer Solvent System; DMF (99.8%, anhydrous), toluene (99.8%, anhydrous), and hexanes (≥99%, anhydrous) used for nanocrystal stripping were purchased from Sigma Aldrich; all other solvents were HPLC grade and used as received.

4.7.2 Synthesis and Sample Preparation

Syntheses of the ZnO nanocrystals,[28,29] PIM-1,[30] and ZIF-8[31] used as the standard for the XANES experiment were followed from literature procedures.

Naked Zinc Oxide (ZnO) Nanocrystal Stripping

Ligand stripping was adapted from Doris et al.[28] DMF (500 µL) charged with BF_3-etherate (10 µL) was mixed with the ZnO nanocrystal dispersion in hexanes (500 µL, ~60 mg/mL) under nitrogen. Toluene (3.5 mL) was added to crash out the nanocrystals. The crystals were isolated by centrifugation and washed in 1:1:7 DMF:hexanes:toluene (v/v/v) twice and dispersed in DMF. The stripped ZnO nanocrystals were characterized by PXRD, EDX, TGA, and TEM, and they had an average particle size of 7±2 nm.

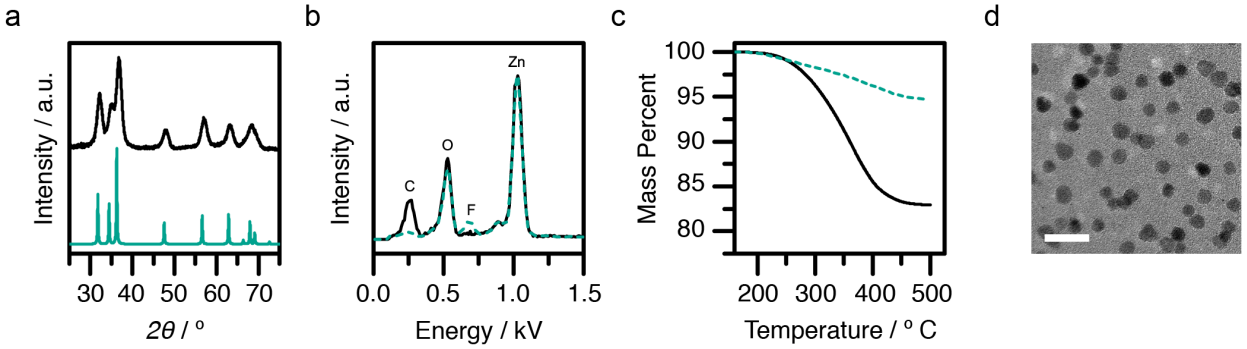

Figure 4.13 Characterization of ZnO nanocrystals. a) Baseline-subtracted PXRD pattern for naked nanocrystals (top, black) and the simulated powder pattern (green, bottom). b) EDX spectra of as-synthesized nanocrystals (black, solid) and naked nanocrystals (green, dashed) show the loss of the carbon signal from the organic ligands and the appearance of a fluorine peak from the BF_4^- counter ion after ligand stripping. Normalized to the Zn peak for clarity. c) TGA mass loss normalized to the weight after driving off solvent at 160 °C is lower for naked nanocrystals (green, dashed) than for the as-synthesized nanocrystals (black, solid), demonstrating the effective removal of organics during ligand stripping. d) TEM images of naked ZnO nanocrystals. Particles are monodisperse and 7±2 nm in diameter. Scale bar is 20 nm.

Polymer Support Fabrication

The polymer cross-linking chemistry was adapted from Du et al.[32] Typically, PIM-1 (M_n = 19.3 kg mol^{-1}, M_w = 52.1 kg mol^{-1}, M_w / M_n = 2.70, 70 mg) was dissolved in chlorobenzene (1700 μL) and chloroform (300 μL) before adding 2,6-bis(4-azidobenzylidene)cyclohexanone (17 mg). This mixture (200 μL) was passed through a 0.2 μm PTFE filter onto a 1.8 x 1.8 cm single crystal silicon wafer and spin coated. The resulting films were annealed under vacuum at 175° C for 7 h. The crosslinked films were insoluble in solutions of heated DMF.

ZnO-to-ZIF Transformation

A Biotage Initiator microwave was used for the chemical transformations. 4 mL of the relevant reaction solution was used for each transformation. All chemical transformations with 2-methylimidazole used to study ZIF-8 formation under different reaction conditions had a ligand concentration of 1.11 M and were held at 50 ˚C for 30 min. Due to solubility restrictions, all reactions with benzimidazole were in 3:1 DMF:H2O (*v*/*v*) solutions.

4.7.3 Characterization Methods

GIXD was performed at two beamlines. Data were collected at the Stanford Synchrotron Radiation Laboratory (SSRL) beamline 11-3 with a photon energy of 12.7 keV. A MAR345 2D detector was used at a sample–detector distance of 175 mm. Integration of the diffraction peak areas was performed with the software WxDiff.[33] Additional data were collected at beamline 7.3.3 of the Advanced Light Source, Lawrence Berkeley National Laboratory, using a photon energy of 10 keV, a sample–detector distance of 280 mm, and a Pilatus 2 M detector.[34] These diffraction peak areas were integrated with the software package Nika for Igor Pro.[35] The incident angle at both beamlines was fixed at 0.12° and all experiments were conducted in a He atmosphere. Diffraction patterns were scaled for clarity.

Zn K-edge XANES spectra were collected at the Advanced Light Source (ALS) beamline 10.3.2.[36] The incident angle was ~15° and the spot size ~50 × 3 μm. Scans were taken at between 4 and 20 spots on each sample, until adequate signal to noise was achieved, from 9.56 to 10.00 keV using a Canberra 7-element UltraLEGe solid-state Ge detector or Amp-Tek silicon drift diode detector and averaged together. Spectra of bulk ZnO and ZIF-8 nanocrystals were used in least-squares linear fits of each sample. Monochromator drift was accounted for by making E0 a parameter of the fit. Probe depths were estimated using the Hephaestus software package. At the 15° incident angle used, these depths correspond to a 22.5 μm thick ZIF-8 sample, assuming a density of 1.45 g cm^{-3}, and a 2.14 μm thick ZnO sample, assuming a density of 5.61 g cm^{-3}.[37] Because the measured sample thicknesses were well below this limit, no overabsorption correction was used. PCA and least-squares fits were performed on the data set using routines previously described.[38] These analyses and all other data processing were completed using software provided at the beamline.

SEM images were obtained with a Zeiss Gemini Ultra-55 analytical scanning electron microscope equipped with an in-lens detector at an accelerating voltage of 5 kV. Prior to imaging, samples were coated with a few nanometers of amorphous carbon using an Electron Microscopy Sciences 150T ES high vacuum carbon evaporator. Images were adjusted for brightness and contrast using the levels tool in Adobe Photoshop. Energy-dispersive X-ray

spectroscopy (EDX) measurements were obtained on the same microscope using the equipped EDAX detector.

PXRD patterns for the ZIF films were recorded using a Bruker D8 Advance diffractometer with Göbel-mirror monochromated Cu-Kα source operating at 40 kV and 40 mA, and those for the ZnO and bulk ZIF-8 nanocrystals were recorded on a Bruker Gadds-8 diffractometer with Cu-Kα source operating at 40 kV and 20 mA. Diffraction patterns were simulated using the Mercury 3.5.1 software package.[39]

TEM images of the nanocrystal precursors were taken on a JEOL 2100-F Field-Emission TEM at 100 k magnification with an accelerating voltage of 120 kV.

Thermogravimetric analysis (TGA) measurements were taken using a TA Instruments Q5000 IR Thermogravimetric Analyzer. Samples were held at 160 ˚C for 60 min to drive off solvent then ramped at 20 ˚C/min to 500 ˚C.

4.8 Acknowledgements

I would like to thank the many scientists who worked on this project with me: Changyi Li, Wendy Queen, Teresa Williams, Jeffrey Long, Raffaella Buonsanti, Delia Milliron, and Brett Helms. I would also like to thank Chenhui Zhu, Tim Dunn, and Chad Miller for assistance with GIXD; Matthew Marcus for assistance with XANES; Lorenzo Maserati for the ZIF-8 spectral reference sample; and Sean Doris and Andrew Wills for useful discussion. This work was supported as part of the Center for Gas Separations Relevant to Clean Energy Technologies, an Energy Frontier Research Center funded by the U.S. Department of Energy, Office of Science, Basic Energy Sciences, under Award No. SC0001015. Portions of this work, including synthesis, characterization, and chemical transformations thereof, were carried out as User Projects at the Molecular Foundry, which is supported by the Office of Science, Office of Basic Energy Sciences, of the U.S. Department of Energy under Contract No. DE-AC02-05CH11231. XANES spectroscopy and GIXD were carried out at beamlines 10.3.2 and 7.3.3, respectively, of the Advanced Light Source, which is supported by the Director, Office of Science, Office of Basic Energy Sciences, of the U.S. Department of Energy under the same contract. Additional GIXD was carried out at beamline 11-3 at the Stanford Synchrotron Radiation Lightsource, SLAC National Accelerator Laboratory, which is supported by the U.S. Department of Energy, Office of Science, Office of Basic Energy Sciences under Contract No. DE-AC02-76SF00515.

4.9 References

1. a) C. Sanchez, B. Julián, P. Belleville, M. Popall, *J. Mater. Chem.* **2005**, *15*, 3559; b) R. B. Thompson, V. V. Ginzburg, M. W. Matsen, A. C. Balazs, *Science* **2001**, *292*, 2469.
2. a) J. N. Coleman, U. Khan, W. J. Blau, Y. K. Gun'ko, *Carbon* **2006**, *44*, 1624; b) J. Bauer, S. Hengsbach, I. Tesari, R. Schwaiger, O. Kraft, *Proc. Natl. Acad. Sci. U. S. A.* **2014**, *111*, 2453; c) S. M. Liff, N. Kumar, G. H. McKinley, *Nat. Mater.* **2007**, *6*, 76.
3. a) A. S. Aricò, P. Bruce, B. Scrosati, J. M. Tarascon, W. van Schalkwijk, *Nat. Mater.* **2005**, *4*, 366; b) J. Kim, G. K. Ong, Y. Wang, G. LeBlanc, T. E. Williams, T. M. Mattox, B. A. Helms, D. J. Milliron, *Nano Lett.* **2015**, *15*, 5574.

4. a) A. C. Arsenault, H. Míguez, V. Kitaev, G. A. Ozin, I. Manners, *Adv. Mater.* **2003**, *15*, 503; b) A. C. Arsenault, D. P. Puzzo, I. Manners, G. A. Ozin, *Nat. Photonics* **2007**, *1*, 468.
5. a) A. J. Brown, N. A. Brunelli, K. Eum, F. Rashidi, J. R. Johnson, W. J. Koros, C. W. Jones, S. Nair, *Science* **2014**, *345*, 72; b) J. Yao, D. Dong, D. Li, L. He, G. Xu, H. Wang, *Chem. Commun.* **2011**, *47*, 2559.
6. W. Li, Q. Meng, X. Li, C. Zhang, Z. Fan, G. Zhang, *Chem. Commun.* **2014**, *50*, 9711.
7. B. Chen, Z. Yang, Y. Zhu, Y. Xia, *J. Mater. Chem. A* **2014**, *2*, 16811.
8. A. F. Bushell, M. P. Attfield, C. R. Mason, P. M. Budd, Y. Yampolskii, L. Starannikova, A. Rebrov, F. Bazzarelli, P. Bernardo, J. C. Jansen, M. Lanč, K. Friess, V. Shantarovich, V. Gustov, V. Isaeva, *J. Membr. Sci.* **2013**, *427*, 48.
9. a) K. S. Park, Z. Ni, A. P. Côté, J. Y. Choi, R. Huang, F. J. Uribe-Romo, H. K. Chae, M. O'Keeffe, O. M. Yaghi, *Proc. Natl. Acad. Sci. U. S. A.* **2006**, *103*, 10186; b) L. E. Kreno, K. Leong, O. K. Farha, M. Allendorf, R. P. Van Duyne, J. T. Hupp, *Chem. Rev.* **2012**, *112*, 1105; c) S. Sorribas, P. Gorgojo, C. Téllez, J. Coronas, A. G. Livingston, *J. Am. Chem. Soc.* **2013**, *135*, 15201.
10. a) X. Huang, B. Zheng, Z. Liu, C. Tan, J. Liu, B. Chen, H. Li, J. Chen, X. Zhang, Z. Fan, W. Zhang, Z. Guo, F. Huo, Y. Yang, L. H. Xie, W. Huang, H. Zhang, *ACS Nano* **2014**, *8*, 8695; b) H. T. Kwon, H. K. Jeong, *J. Am. Chem. Soc.* **2013**, *135*, 10763; c) F. Cacho-Bailo, B. Seoane, C. Téllez, J. Coronas, *J. Membr. Sci.* **2014**, *464*, 119; d) H. Bux, F. Liang, Y. Li, J. Cravillon, M. Wiebcke, J. Caro, *J. Am. Chem. Soc.* **2009**, *131*, 16000.
11. G. Lu, J. T. Hupp, *J. Am. Chem. Soc.* **2010**, *132*, 7832.
12. a) O. Shekhah, H. Wang, D. Zacher, R. A. Fischer, C. Wöll, *Angew. Chem., Int. Ed.* **2009**, *48*, 5038; b) H. K. Arslan, O. Shekhah, J. Wohlgemuth, M. Franzreb, R. A. Fischer, C. Wöll, *Adv. Funct. Mater.* **2011**, *21*, 4228; c) L. Heinke, M. Tu, S. Wannapaiboon, R. A. Fischer, C. Wöll, *Microporous Mesoporous Mater.* **2015**, *216*, 200; d) G. Lu, O. K. Farha, W. Zhang, F. Huo, J. T. Hupp, *Adv. Mater.* **2012**, *24*, 3970.
13. E. Shamsaei, Z. X. Low, X. Lin, A. Mayahi, H. Liu, X. Zhang, J. Z. Liu, H. Wang, *Chem. Commun.* **2015**, *51*, 11474.
14. a) Y. Yue, Z. A. Qiao, X. Li, A. J. Binder, E. Formo, Z. Pan, C. Tian, Z. Bi, S. Dai, *Cryst. Growth Des.* **2013**, *13*, 1002; b) I. Stassen, N. Campagnol, J. Fransaer, P. Vereecken, D. De Vos, R. Ameloot, *CrystEngComm* **2013**, *15*, 9308; c) J. Yang, Z. Xie, H. Yin, J. Wang, J. Xu, J. Wang, J. Lu, D. Yin, Y. Zhang, *Microporous Mesoporous Mater.* **2014**, *198*, 263; d) J. Li, W. Cao, Y. Mao, Y. Ying, L. Sun, X. Peng, *CrystEngComm* **2014**, *16*, 9788; e) M. Drobek, M. Bechelany, C. Vallicari, A. Abou Chaaya, C. Charmette, C. Salvador-Levehang, P. Miele, A. Julbe, *J. Membr. Sci.* **2015**, *475*, 39; f) K. Khaletskaya, S. Turner, M. Tu, S. Wannapaiboon, A. Schneemann, R. Meyer, A. Ludwig, G. Van Tendeloo, R. A. Fischer, *Adv. Funct. Mater.* **2014**, *24*, 4804; g) Y. Yue, N. Mehio, A. J. Binder, S. Dai, *CrystEngComm* **2015**, *17*, 1728.
15. S. Li, W. Zhang, Y. Zhu, Q. Zhao, F. Huo, *Cryst. Growth Des.* **2015**, *15*, 1017.
16. W. W. Zhan, Q. Kuang, J. Z. Zhou, X. J. Kong, Z. X. Xie, L. S. Zheng, *J. Am. Chem. Soc.* **2013**, *135*, 1926.
17. X. Zhang, Y. Liu, L. Kong, H. Liu, J. Qiu, W. Han, L. T. Weng, K. L. Yeung, W. Zhu, *J. Mater. Chem. A* **2013**, *1*, 10635.
18. J. Reboul, S. Furukawa, N. Horike, M. Tsotsalas, K. Hirai, H. Uehara, M. Kondo, N. Louvain, O. Sakata, S. Kitagawa, *Nat. Mater.* **2012**, *11*, 717.

19. K. Okada, R. Ricco, Y. Tokudome, M. J. Styles, A. J. Hill, M. Takahashi, P. Falcaro, *Adv. Funct. Mater.* **2014**, *24*, 1969.
20. R. Schmidt, J. H. Oh, Y. S. Sun, M. Deppisch, A. M. Krause, K. Radacki, H. Braunschweig, M. Könemann, P. Erk, Z. Bao, F. Würthner, *J. Am. Chem. Soc.* **2009**, *131*, 6215.
21. J. C. Tan, T. D. Bennett, A. K. Cheetham, *Proc. Natl. Acad. Sci. U. S. A.* **2010**, *107*, 9938.
22. J. Cravillon, C. A. Schröder, H. Bux, A. Rothkirch, J. Caro, M. Wiebcke, *CrystEngComm* **2012**, *14*, 492.
23. M. C. McCarthy, V. Varela-Guerrero, G. V. Barnett, H. K. Jeong, *Langmuir* **2010**, *26*, 14636.
24. E. L. Bustamante, J. L. Fernández, J. M. Zamaro, *J. Colloid Interface Sci.* **2014**, *424*, 37.
25. J. R. Schmink, N. E. Leadbeater, N. E. Leadbeater, *Microwave Heating as a Tool for Sustainable Chemistry*, 2010.
26. X. Zhang, Y. Liu, S. Li, L. Kong, H. Liu, Y. Li, W. Han, K. L. Yeung, W. Zhu, W. Yang, J. Qiu, *Chem. Mater.* **2014**, *26*, 1975.
27. V. I. Isaeva, M. I. Barkova, L. M. Kustov, D. A. Syrtsova, E. A. Efimova, V. V. Teplyakov, *J. Mater. Chem. A* **2015**, *3*, 7469.
28. S. E. Doris, J. J. Lynch, C. Li, A. W. Wills, J. J. Urban, B. A. Helms, *J. Am. Chem. Soc.* **2014**, *136*, 15702.
29. D. Sun, M. Wong, L. Sun, Y. Li, N. Miyatake, H.-J. Sue, *J. Sol-Gel Sci. Technol.* **2007**, *43*, 237.
30. a) P. M. Budd, E. S. Elabas, B. S. Ghanem, S. Makhseed, N. B. McKeown, K. J. Msayib, C. E. Tattershall, D. Wang, *Adv. Mater.* **2004**, *16*, 456; b) H. A. Patel, C. T. Yavuz, *Chem. Commun.* **2012**, *48*, 9989.
31. J. Cravillon, S. Münzer, S.-J. Lohmeier, A. Feldhoff, K. Huber, M. Wiebcke, *Chem. Mater.* **2009**, *21*, 1410.
32. N. Du, M. M. Dal-Cin, I. Pinnau, A. Nicalek, G. P. Robertson, M. D. Guiver, *Macromol. Rapid Commun.* **2011**, *32*, 631.
33. S. C. B. Mannsfeld, WxDiff; Stanford Synchrotron Radiation Lightsource: Menlo Park, CA, **2009**.
34. A. Hexemer, W. Bras, J. Glossinger, E. Schaible, E. Gann, R. Kirian, A. MacDowell, M. Church, B. Rude, H. Padmore, *J. Phys.: Conf. Ser.* **2010**, *247*, 012007.
35. J. Ilavsky, *J. Appl. Crystallogr.* **2012**, *45*, 324.
36. M. A. Marcus, A. A. MacDowell, R. Celestre, A. Manceau, T. Miller, H. A. Padmore, R. E. Sublett, *J. Synchrotron Radiat.* **2004**, *11*, 239.
37. a) B. Ravel, M. Newville, *J. Synchrotron Radiat.* **2005**, *12*, 537; b) S. Cao, T. D. Bennett, D. A. Keen, A. L. Goodwin, A. K. Cheetham, *Chem. Commun.* **2012**, *48*, 7805.
38. a) A. Roßberg, T. Reich, G. Bernhard, *Anal. Bioanal. Chem.* **2003**, *376*, 631; b) T. Ressler, J. Wong, J. Roos, I. L. Smith, *Environ. Sci. Technol.* **2000**, *34*, 950; c) W. B. Kim, J. S. Lee, *J. Phys. Chem. B* **2003**, *107*, 9195.
39. C. F. Macrae, I. J. Bruno, J. A. Chisholm, P. R. Edgington, P. McCabe, E. Pidcock, L. Rodriguez-Monge, R. Taylor, J. van de Streek, P. A. Wood, *J. Appl. Crystallogr.* **2008**, *41*, 466.

Chapter 5

Molecular Understanding of Polyelectrolyte Binders that Actively Regulate Ion Transport in Sulfur Cathodes

5.1 Introduction

The principles dictating microporous material design for gas separations can also inform controlled mass transport in other contexts such as active layers in electrochemical energy storage devices. These active layers typically incorporate polymer binders to aid in processing composite electrodes with well-controlled architecture and compliant mechanical integrity. Polymer binders also dictate the extent of electrode swelling with electrolyte and help mitigate cracking on drying or swelling, or on large volume changes experienced using certain electrode chemistries between their extremes in state-of-charge.[1] Often overlooked is whether a polymer binder is an active or a passive component in the composite electrode, a distinction that denotes whether or not it participates in charge or mass transport; it can also be adaptive if it can be made to switch between passive and active states, e.g., using thermal excursions or redox chemistry.[2] Whereas the chemical constitution of a polymer binder should dictate whether it is passive, active, or adaptive in the electrode, it remains a challenge to reveal the molecular basis by which these behaviors manifest. Without this information, rational design principles for polymer binders remain obscure.

In this work, we elucidate the molecular-level underpinnings that distinguish an active polymer binder designed for the Li–S battery from a ubiquitous yet passive alternative (Figure 5.1). The macromolecular structure of our polyelectrolyte binder—poly[(*N,N*-diallyl-*N,N*-dimethylammonium) bis(trifluoromethanesulfonyl)imide] (PEB-1)—allows two types of ion transport critical to the operation of a Li–S cell to be actively facilitated or regulated: facilitated transport of lithium ions throughout the sulfur cathode, which manifests as low charge-transfer resistance and fast electrode kinetics; and restricted diffusion of soluble polysulfides (Li_2S_n, where $n = 4–8$) from nitrogen-doped mesoporous carbon (N-MC) sulfur hosts into the electrolyte. As seen with the mmen-Mg_2(dobpdc)-based MMMs in chapter 3, chemisorptive sites in a polymer matrix provide channels for the selective facilitated transport of analytes. However, chemisorption can also impede diffusion if the interaction is sufficiently favorable. Both cases are demonstrated here in the case of the positively charged backbone of PEB-1. The emerging perspective from our work is that the design space for polyelectrolyte binders is superior, allowing for broad tunability of electrochemical stability (both anodic and cathodic), energetic barriers to Li^+ desolvation and transport, and adhesion.

Our success highlights the profound yet often underappreciated importance of macromolecular design and mechanistic understanding of active polymer binders in Li–S battery technology development, where the role of the binder in the cathode should be considered in stride with other cell components, including sulfur-rich polymers,[3] sulfur host materials,[4] embedded current collectors,[5,6] separators,[7] redox mediators,[8,9] electrolytes,[10] and ionically conductive surface films for long-term lithium metal protection.[9,11] If successful, this battery chemistry is well-positioned to augment the electrochemical energy storage options for transportation, aviation, and light-weight portable power[12]—and may ultimately be the most sustainable solution for these applications given the prevalence and low cost of sulfur relative to transition metals used in conventional Li-ion intercalation solids.[13] Our results are complementary to advances in Li-ion battery technology development using polyelectrolyte binders (e.g., poly(ionic liquid)s), which yielded cells with high specific capacity and excellent long-term electrochemical stability when compared to PVDF binder.[14]

Notably, we demonstrate in the context of Li–S cells that PEB-1 binders make possible their operation with high accessible areal capacity (e.g., up to 8.13 mAh cm^{-2}) and excellent rate capability (e.g., C/5–2C) using cathodes with high-areal sulfur loadings (e.g., up to 8.1 mg cm^{-2}).

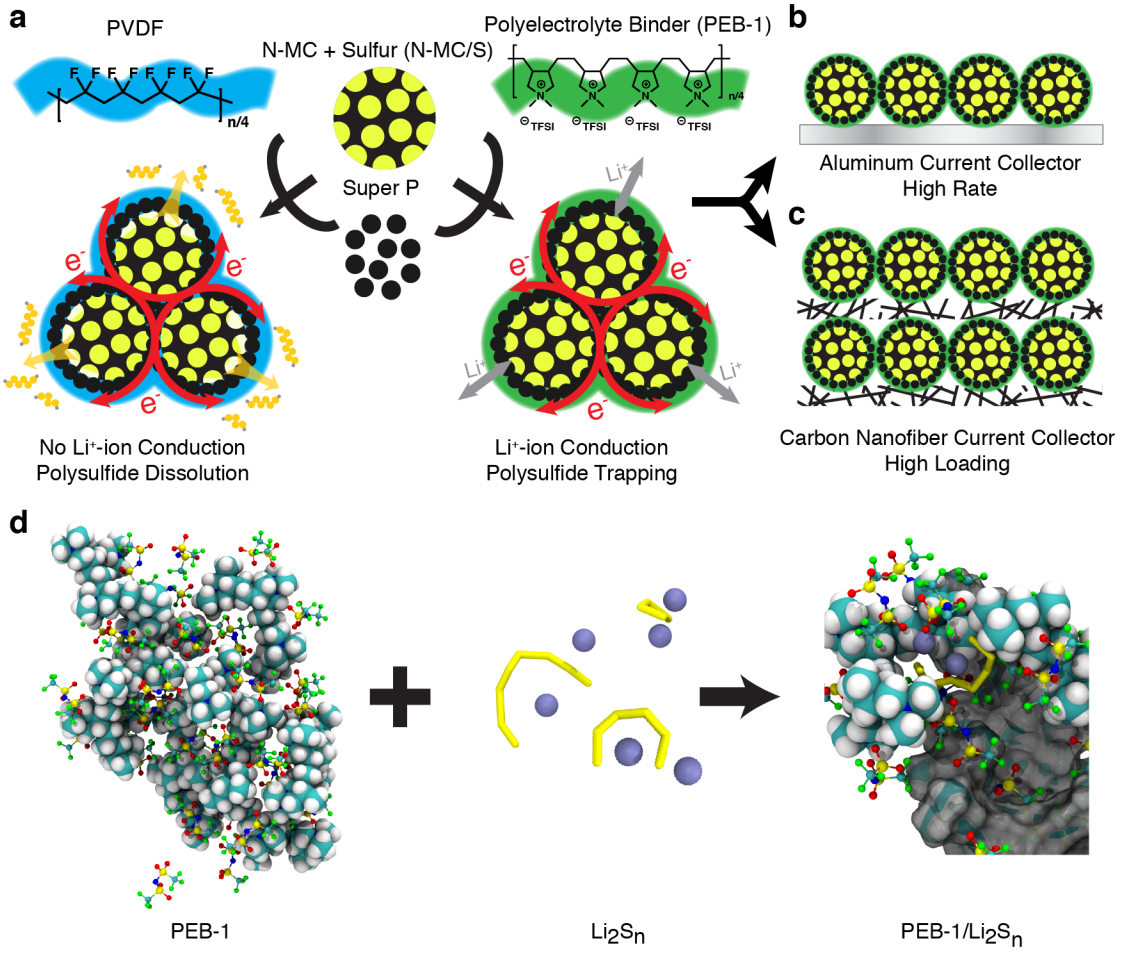

Figure 5.1 Illustration of the fabrication of sulfur electrodes with PVDF or PEB-1 binder. a) The cathode is comprised of sulfur-active materials loaded into N-doped mesoporous carbon (N-MC) hosts, 'Super P' as the conductive additive, and a polymer binder (PEB-1 or PVDF). b) A conventional sulfur cathode cast onto an aluminum current collector. c) A highly loaded sulfur cathode cast onto a carbon nanofibre current collector. d) Schematic illustrating the formation of complex ion clusters via anion metathesis, when PEB-1 encounters soluble polysulfides during Li–S cell cycling.

On the other hand, composite sulfur cathodes prepared using poly(vinylidene difluoride) (PVDF), a common but passive polymer binder, exhibit slower and rapidly degrading electrode kinetics. In turn, PVDF cells access lower capacity and experience shorter cycle life.

While facilitated Li-ion mass transport in PEB-1 was characterized as charge transport through electrochemical means (as described elsewhere[15]), understanding the restricted transport of polysulfides necessitated detailed spectroscopic characterization to elucidate the PEB-1/polysulfide interactions. In this chapter, I describe these methods and the insights they yield into polysulfide transport through the PEB-1 binder.

5.2 Designing Polyelectrolyte Binders to Regulate Polysulfide Transport

In our Li–S cells regulated transport of polysulfides is key to capacity retention, Coulombic efficiency, and long-term Li-anode stability, particularly at high-areal sulfur loadings.[16] Such regulation was also considered in the design of PEB-1, where we sought to leverage the anion metathesis between polymer-associated $TFSI^-$ anions and the anionic end-groups of lithium polysulfides that are generated during intermediate states-of-charge of the Li–S cell.

Specifically, LiS_n radical anions could bind at their anionic terminus to cationic pyrrolidinium polymer moieties; on the other hand, Li_2S_n dianionic polysulfides can bind through either a single terminus or both termini. In the case of the latter, Li_2S_n can bind to the same polymer chain twice (i.e., an intramolecular crosslink), or to two adjacent polymer chains (i.e., an intermolecular crosslink). For both, this requires the initially ring-closed Li_2S_n species to exchange its most labile lithium ion for the pyrrolidinium cation prior to ring-opening and exchange of the second lithium ion with another pyrrolidinium cation (Figure 5.1d).[17,18] Any of the binding modes described is concomitant with the generation of either one or two molecular equivalents of LiTFSI, which aids in maintaining high [LiTFSI] where polysulfides are generated, as needed for fast electrode kinetics.

5.3 Understanding Anion Metathesis in Polyelectrolyte Binders

The excellent polysulfide-binding character of PEB-1 (Figure 5.2a) was initially demonstrated by introducing PEB-1 solids to solutions of lithium polysulfides (10 mM, prepared as Li_2S_6) in a 1:1 *v*/*v* mixture 1,3-dioxolane/1,2-dimethoxyethane (DOL/DME) containing LiTFSI (1.0 M) and $LiNO_3$ (0.20 M), the electrolyte used in our Li–S cell; PEB-1 is not soluble in DOL:DME electrolyte. After 1 h, 96% of the polysulfides had been leached from solution through anion metathesis, as determined by optical spectroscopy of the filtrate (Figure 5.2c–e).[19] The PEB-1/polysulfide composite (Figure 5.2a) was isolated by filtration and dried under inert conditions before further analysis by X-Ray photoelectron spectroscopy (XPS) and X-Ray absorption spectroscopy (XAS). A similar phenomenon could be observed without LiTFSI and $LiNO_3$ in the electrolyte (Figure 5.2b), illustrating the strong absorption behavior of PEB-1, even without supporting salts.

The extent of anion metathesis was determined by XPS, taking advantage of the unique chemical signatures in the *N* 1 s spectra for pyrrolidinium and $TFSI^-$ moieties of PEB-1 (Figure 5.3a). The peak at 402.8 eV is assigned to the quaternary nitrogen atom in the pyrrolidinium ring (i.e., N_{cation}), whereas the peak with lower binding energy at 399.2 eV is assigned to the nitrogen atom in $TFSI^-$ (i.e., N_{anion}). The peak area ratio between N_{cation} and N_{anion} is ~1:1, as is expected from the chemical structure of PEB-1. However, as shown in Figure 5.3b, anion metathesis results in a near-complete loss of N_{anion} at 399.2 eV, indicating replacement of $TFSI^-$ anions with S_n^{2-} anions. These peak assignments were validated by density functional theory (DFT) calculations of the valence electron charge density around the selected atom (Figure 5.4). Here, the lower valence electron density around the excited atom leads to higher XPS-binding energy, and vice versa.

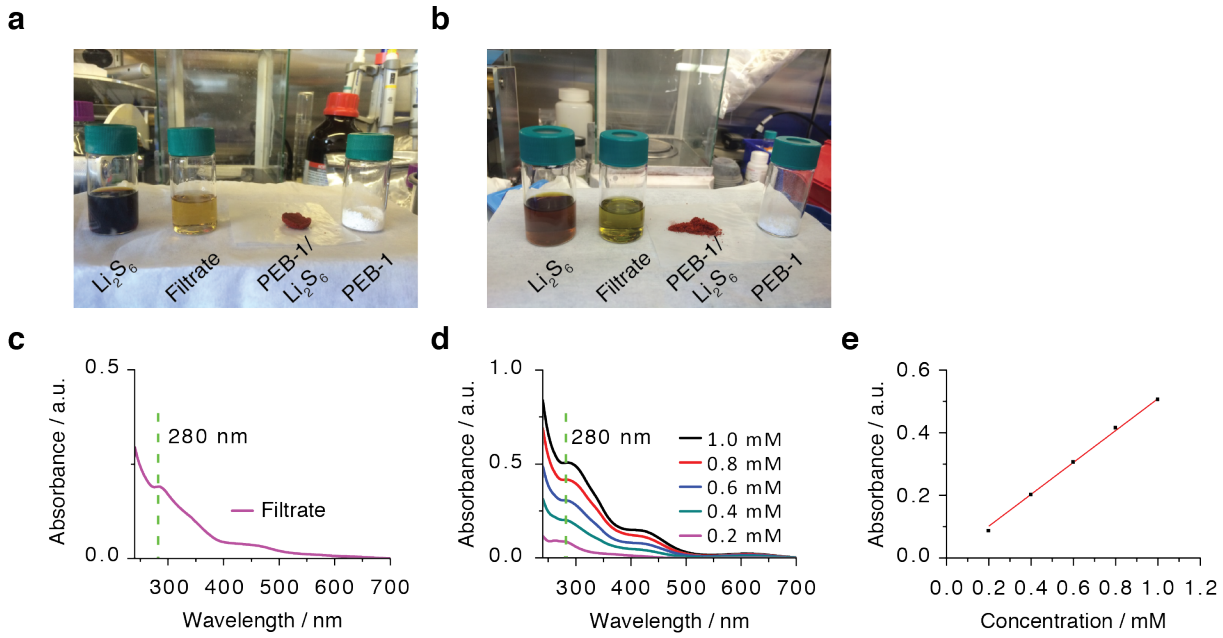

Figure 5.2 Top row: qualitative understanding of the polysulfide adsorbing character of PEB-1. a) Electrolyte composition: 1.0 M LiTFSI + 0.2 M $LiNO_3$. b) Electrolyte obviates use of both LiTFSI and $LiNO_3$. From left to right: lithium polysulfides dissolved in electrolyte (10 mM, prepared nominally as Li_2S_6), the filtrate after PEB-1 had been introduced (and isolated) to sequester polysulfides from solution, the PEB-1/S_6 composite after PEB-1 underwent anion metathesis with Li_2S_6, pristine PEB-1 powder. Bottom row: quantitative determination of residual polysulfides in electrolyte after PEB-1 introduced as a chemisorbing species. c) UV-vis spectrum of the filtrate after anion metathesis. d) UV-vis spectra of standard Li_2S_6 solutions with concentrations of 0.20, 0.40, 0.60, 0.80, and 1.00 mM. e) Calibration curve linking optical absorbance at 280 nm to Li_2S_6 concentration.

5.4 Modeling and Characterizing PEB-1/Polysulfide Binding Modes

Although lithium polysulfides in electrolyte are mixtures of LiS_n and Li_2S_n, where *n* varies by states-of charge, Li_2S_n are the most prevalent.[18] We were then interested in understanding the binding geometries available to Li_2S_n for different oligomer length *n* to interact with one or more cationic polymer chains. We accomplished this by means of semi-classical, accelerated molecular dynamics simulations. Model systems, comprising a short oligomer of PEB-1 (in this case a tetramer), along with its $TFSI^-$ counterions, and various oligomer lengths of Li_2S_n were considered, and the binding free energy determined from extensive metadynamics simulations.[20] Critically, we employed a fluctuating charge model to facilitate intermolecular charge transfer and intramolecular charge reorganization,[21] which we found necessary to accurately describe the physics in these systems. Details of our computational methodology can be found elsewhere.[15]

At equilibrium, $TFSI^-$ and Li_2S_n molecules both preferentially interact with pyrrolidinium subunits of the polymer, resulting in ion clusters. We find that the binding free energy of an isolated Li_2S_n molecule to PEB-1 increases with increasing polysulfide chain length, ranging from –48 kJ mol^{-1} for Li_2S_4 to –69 kJ mol^{-1} for Li_2S_8 (Figure 5.3e and Figure 5.5a). Generally, we find that the binding free energy of $TFSI^-$ to PEB-1 is less than the lithium polysulfides, ranging from –52 kJ mol^{-1} with no lithium polysulfides present, –30 kJ mol^{-1} with Li_2S_8 present,

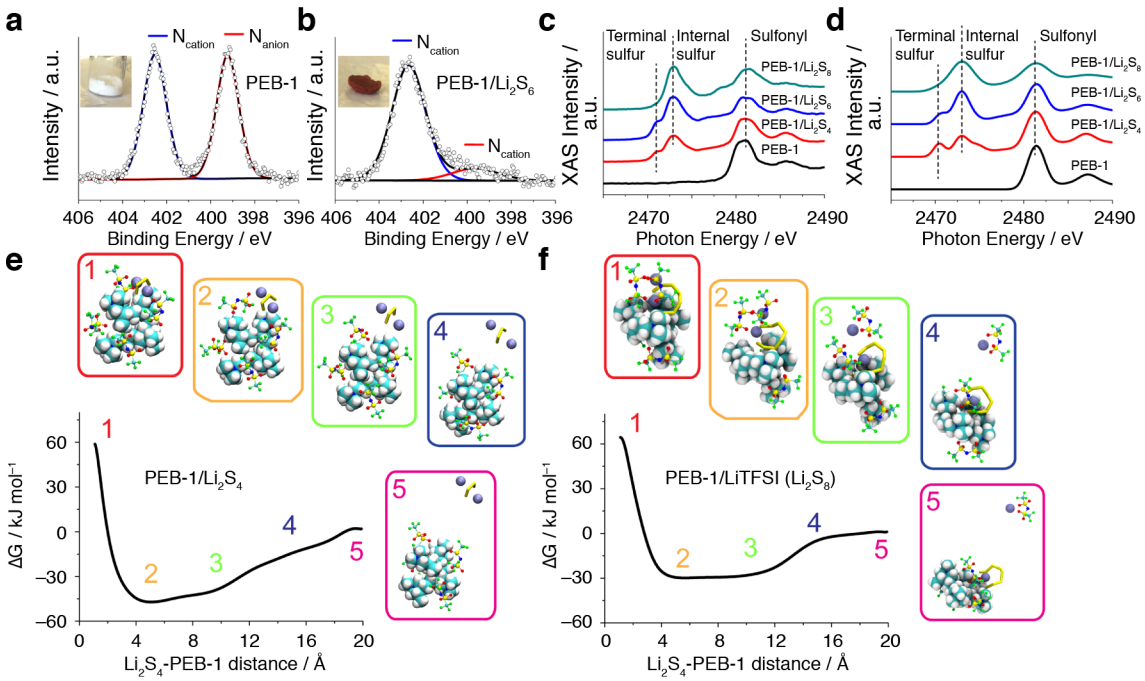

Figure 5.3 Analysis of the PEB-1/polysulfide composite. a, b) X-ray photoelectron spectroscopy (XPS) of the *N* 1 s signal. c) Sulfur K-edge X-ray absorption (XAS) spectra. d) Calculated XAS spectra. e) Free energy corresponding to the interaction of PEB-1 and $Li_2S_4$when LiTFSI is present in the ion cluster. f) Free energy corresponding to the interaction of PEB-1 and LiTFSI when Li_2S_8 is present in the ion cluster.

and –40 kJ mol^{-1} with Li_2S_4 present (Figure 5.3f and Figure 5.5b). Considering the overall equation Li_2S_n + TFSI-PEB -> LiTFSI + LiS_n-PEB, the driving force for metastasis is the ease of formation of LiTFSI. For shorter chain polysulfides, the lithium cations are tightly bound, owing to the large electrostatic interactions resulting from the more polar polysulfide molecules. Indeed, the equilibrium binding geometry is symmetric, with the lithium ions equidistant above and below the polysulfide plane.[18] The reduction in the average partial atomic charge in the larger polysulfides leads to an equilibrium binding geometry comprising a tightly bound and a more labile lithium ion in a ring-closed polysulfide. The ease of extracting the more labile polysulfide increases with increasing polysulfide chain length, thus promoting metathesis in an oligomer-selective manner. Upon anion metathesis, the nominal ring-closed LiS_n ring-opens and undergoes a second metathesis event, leading to either inter- or intramolecular crosslinks. The longer oligomers were more effective at intermolecular cross-linking in the simulations (Figure 5.1d).

I confirmed these predictions suggesting PEB-1 preferentially binds to higher order polysulfides using S K-edge XAS.[17] I collected the near edge structure spectra at the Advanced Light Source beamline 10.3.2.[22] Scans were taken from 2410 to 2525 eV with an energy resolution of 0.25 eV. All spectra were calibrated to a gypsum reference standard. Data were acquired using an Amptek silicon drift detector at five spots on each sample and averaged together to increase the signal-to-noise ratio without inducing beam damage. I performed normalization and pre-edge background subtraction using software provided at the beamline.

As noted above, the terminal atoms on the polysulfide chain are more negatively charged than the bridging sulfur atoms. Spectroscopically, this manifests as a pre-edge feature near 2471 eV in the sulfur K-edge XAS, distinct from the regular sulfur “white-line” peak near

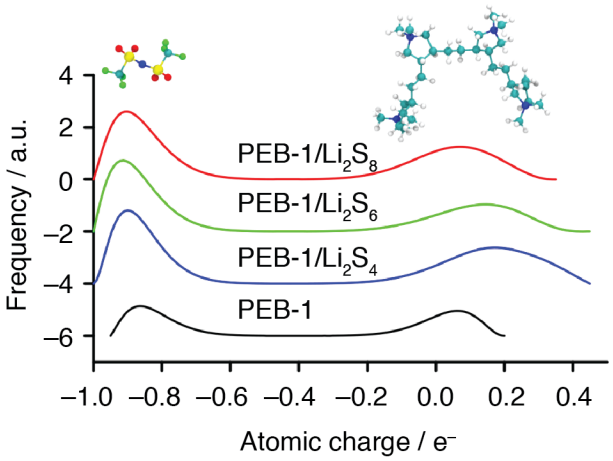

Figure 5.4 DFT calculations of the valence electron charge density of N atoms in $TFSI^-$ (left hand side) and the pyrrolidinium moieties of a tetramer model of PEB-1.

2472 eV. Further, theoretical calculations have shown that the relative intensity of this peak is a function of the ratio of the number of bridging/terminal sulfur atoms, such that Li_2S_4 has a more pronounced pre-peak than Li_2S_8. This insight has been used to fit experimental XAS data[23] to determine speciation in working Li–S cells. Alternative approaches have utilized experimentally derived standards of related ionic crystals to determine speciation.[24] PEB-1 shows two major peaks around 2481 and 2486 eV, which are contributed by the sulfonyl functional group in $TFSI^-$ anions (Figure 5.3c). For PEB-1/Li_2S_8, PEB-1/Li_2S_6, and PEB-1/Li_2S_4, we observe an additional peak and its shoulder at 2473 eV and 2471 eV, which are due to, respectively, bridging and terminal sulfur atoms in polysulfides.[25] As the oligomer length of Li_2S_n increases, the peak at 2473 eV also increases, which is due to the presence of more polysulfide in the PEB-1/Li_2S_n composite. The peak area ratio of the terminal and bridging sulfur atoms decreases as *n* increases from 4 to 6 and 8, which is in agreement the theoretical composition of S_8^{2-}, S_6^{2-}, and S_4^{2-}. The experimental XAS absorption spectra are in agreement with DFT calculations (Figure 5.3d). Of interest is the XAS spectrum of the PEB-1/Li_2S_8 complex. I would expect a significant, though reduced, pre-edge feature for the ring-closed structure, consistent with the XAS of the shorter chained polysulfides. However, in the experimental XAS spectrum I observe no evidence of a pre-edge feature, which is only recovered computationally when considering a ring-opened structure (Figure 5.6), where the terminal sulfur atoms are more covalently bonded to the pyrrolidinium nitrogen atoms that pull electron density away.

Conventional anionic (and lithiated) polyelectrolyte binders are incapable of such cross-linking with polysulfides, and thus do not actively regulate polysulfide migration; PEB-1 is unique in that regard. Ultimately, we view PEB-1's role in regulating polysulfide migration as analogous to a variety of inorganic adsorbents recently described by Cui,[26] Nazar,[27] and others[28] with the added benefits of facilitating Li-ion transport and also serving as a binder. PEB-1 may also find more practical use than other cationic binders for Li–S cells, e.g., poly(acrylamide-*co*-diallyldimethylammonium chloride), which corrodes Al current collectors.[29] By obviating the use of corrosive Cl^- counterions, PEB-1 is a preferred embodiment. It may also be the case that PEB-1 influences the electrolyte system within the electrode's pores, altering the chemistry and solvated structures of polysulfides and the working ion in the pores. This has been suggested for binders like poly(ethylene oxide),[30,31] which delays the passivation of the cathode at end of discharge rather than a trapping capacity for polysulfides.[30]

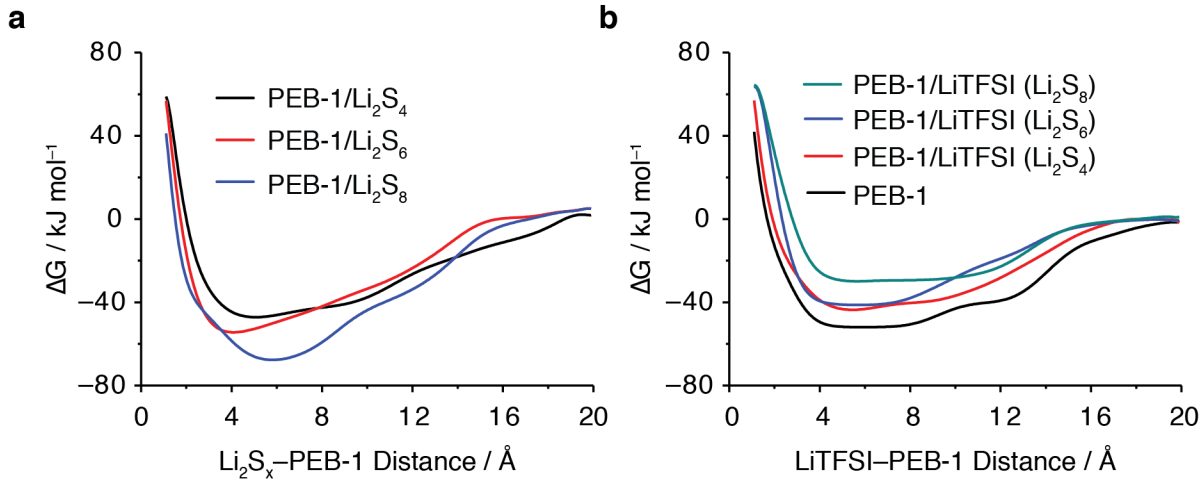

Figure 5.5 Free energy curves highlighting the selective nature of Li_2S_n and LiTFSI binding to PEB-1/S_n/LiTFSI ion clusters as it depends on oligomer length, n. a) The interaction of PEB-1 and Li_2S_n when LiTFSI is present. b) The interaction of PEB-1 and LiTFSI when Li_2S_n is present.

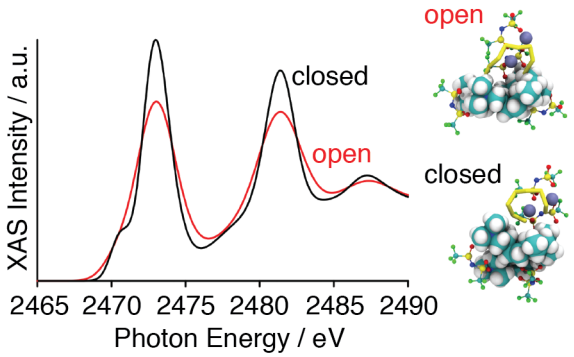

Figure 5.6 Simulated sulfur K-edge X-ray absorption near edge structure spectra of PEB-1/Li_2S_8 with closed and open polysulfide complexes, with respect to Li^+ coordination. These calculations support the assessment of features in the experimentally observed S K-edge XAS as arising from a ring-opened polysulfide configuration.

5.5 Li–S Cell Performance Gains When Active PEB-1 Binders are in Place

To confirm the positive impact of PEB-1 in Li–S cells, we assembled and tested coin cells with either PEB-1 or PVDF binder (denoted hereafter as PEB-1 or PVDF cells). In order to evaluate the long-term cycling stability, galvanostatic cycling of the Li–S cells with either PEB-1 or PVDF binder was carried out at a rate of C/5 (Figure 5.7a). After 250 cycles, a high capacity of 731.1 mAh g^{-1} was still retained for PEB-1 cells, which is owing to the polysulfide-trapping character of PEB-1. Meanwhile, PVDF cells underwent faster degradation, within 200 cycles; after ~220 cycles, abrupt failure of the PVDF cells occurred. As PVDF does not bind polysulfides strongly, more sulfur loss to the anode side can be expected with each cycle. Polysulfides react with lithium metal anode, as do the components in the electrolyte. In that PVDF cells failed fast, loss of both active sulfur and electrolyte are at fault. The evolution of polarization of the cells is evaluated by comparing the discharge–charge voltage profiles of the 1st and 200th cycles of PVDF and PEB-1 cells (Figure 5.7b,c). For PEB-1 cells, there is no

significant increase in overpotential due to the good stability and integrity of the sulfur electrodes, which contributes to fewer side reactions on the lithium metal anode as well. As a comparison, cells with PVDF binder suffer from a large increase in overpotential.

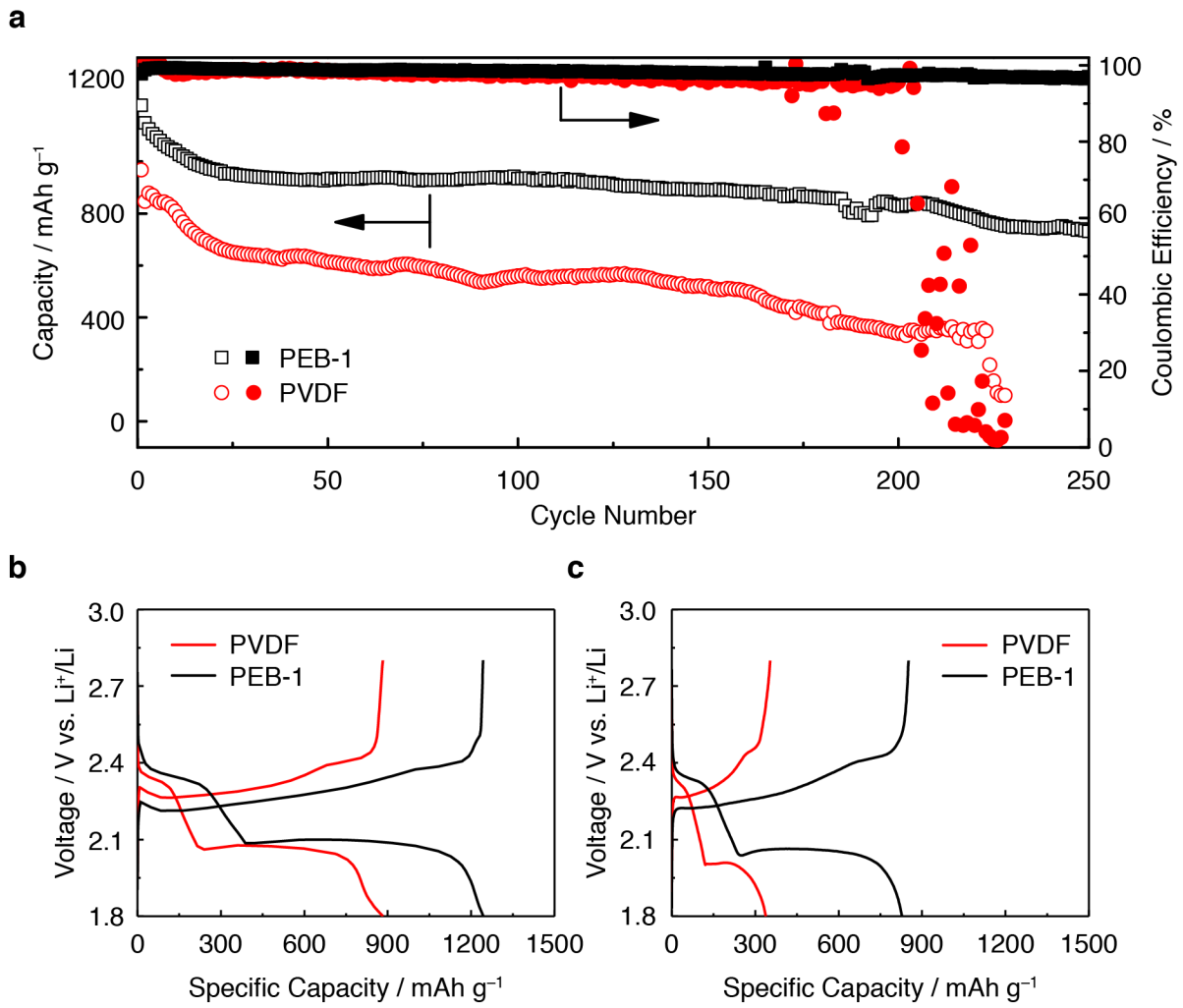

Figure 5.7 a) Cycling performance of Li–S full cells with PEB-1 or PVDF binder at a rate of C/5. The composite sulfur electrodes were cast onto an aluminum current collector. Bottom: Discharge-Charge voltage profiles of PVDF and PEB-1 cells with a sulfur loading of 1.2 mg cm^{-2} deposited onto an aluminum current collector. b) 1st and c) 200th cycles.

5.6 Conclusion

Here I have laid the groundwork for understanding, both experimentally and theoretically, the molecular basis by which polyelectrolyte binders actively exert their influence on the diffusive transport of polysulfide species encountered in the cycling of sulfur electrodes. Their role in this regard concerns restricted active material diffusion, which is critical in minimizing capacity fade at high sulfur loading. Specifically, we found that the hydrophobic and covalent character of higher order and electrolyte-soluble lithium polysulfides leads to preferential and strong electrostatic interactions with the cationic polymer backbone, which could be leveraged to prevent their diffusion from the cathode on cycling. From this bound state,

these polysulfides could either be oxidized on the charge to solid sulfur, thereby preventing further diffusion, or easily reduced on the discharge to shorter oligomers. Furthermore, on reduction, the ionic character of lithium polysulfides increases as the oligomer length decreases along the discharge. We find that the energy holding those ionic polysulfides to the polymer decreases considerably, allowing the critical concentration of Li_2S_4 to be reached and the precipitation of Li_2S_2/Li_2S to occur locally as desirable.

5.7 Experimental Details

5.7.1 Materials

Phenol (99+%), NaOH (97+%), conc. HCl (37%), poly(*N,N*-diallyl -*N,N*-dimethylammonium) chloride (PDDA-Cl, M_n = 400–500 kg mol^{-1}, 20% *w*/*w* in H_2O), Ludox HS40 silica colloid (40% *w*/*w* in H_2O), 1,3-dioxlane (DOL, 99.8%), cyanamide (99%), 1,2-dimethoxymethane (DME, 99.5%), lithium nitrate ($LiNO_3$, 99.99%), and lithium bis(trifluoromethanesulfonimide) (LiTFSI, 99.95%) were obtained from Sigma-Aldrich. Formaldehyde solution (37% *w*/*w* in H_2O), lithium metal strip (0.75 mm thick, 99.9%), and sulfur (99.5%) were obtained from Alfa Aesar. Hydrofluoric acid (48%) was obtained from Acros Organics. Ethanol (88.5–92.5% *v*/*v*) was obtained from Macron Fine chemicals. CNF (>98%) was purchased from Sigma-Aldrich.

5.7.2 Synthesis and Sample Preparation

Resol synthesis

Phenol (12.0 g, 128 mmol) was heated in a round-bottom flask at 65 °C until molten, after which aqueous NaOH (2.50 g, 20% *w*/*w* in H_2O) was added to the flask dropwise.[32] Aqueous formaldehyde (21.0 g, 37% *w*/*w* in H_2O) was then added, and the mixture aged for an additional 50 min at 65 °C. The mixture was subsequently neutralized with aqueous HCl. Water was removed from the reaction mixture *in vacuo* to obtain the resol. Finally, an equal weight of ethanol was mixed with the resol to form the resol ethanol solution (50% *w*/*w*).

N-MC and N-MC/S composite preparation

To prepare the N-MC,[33] the resol ethanol solution (1.0 g, 50% *w*/*w*) was mixed with cyanamide (0.50 g, 12 mmol) and HS40 silica colloid (3.0 ml) and sonicated for 10 min. Afterward, the transparent yellow solution was dried at 50 °C overnight under continuous stirring, thermopolymerization at 100 °C for 24 h, and carbonization of the resulting monolith at 800 °C for 2 h under Ar (heating and cooling rate = 2 °C min^{-1}). To etch away the silica template, the black monolith was ground into powder and immersed in HF (20% *w*/*w* in H_2O) for 24 h. The particulates were isolated by filtration, and the filter cake washed with copious amounts of DI water. The N-MC product was subsequently dried at 50 °C overnight prior to use. For the preparation of N-MC/S composite, N-MC was initially mixed with pure sulfur (weight ratio = 2:8) using a mortar and pestle. The melt-infusion of sulfur into N-MC was then conducted at 155 °C for 12 h.

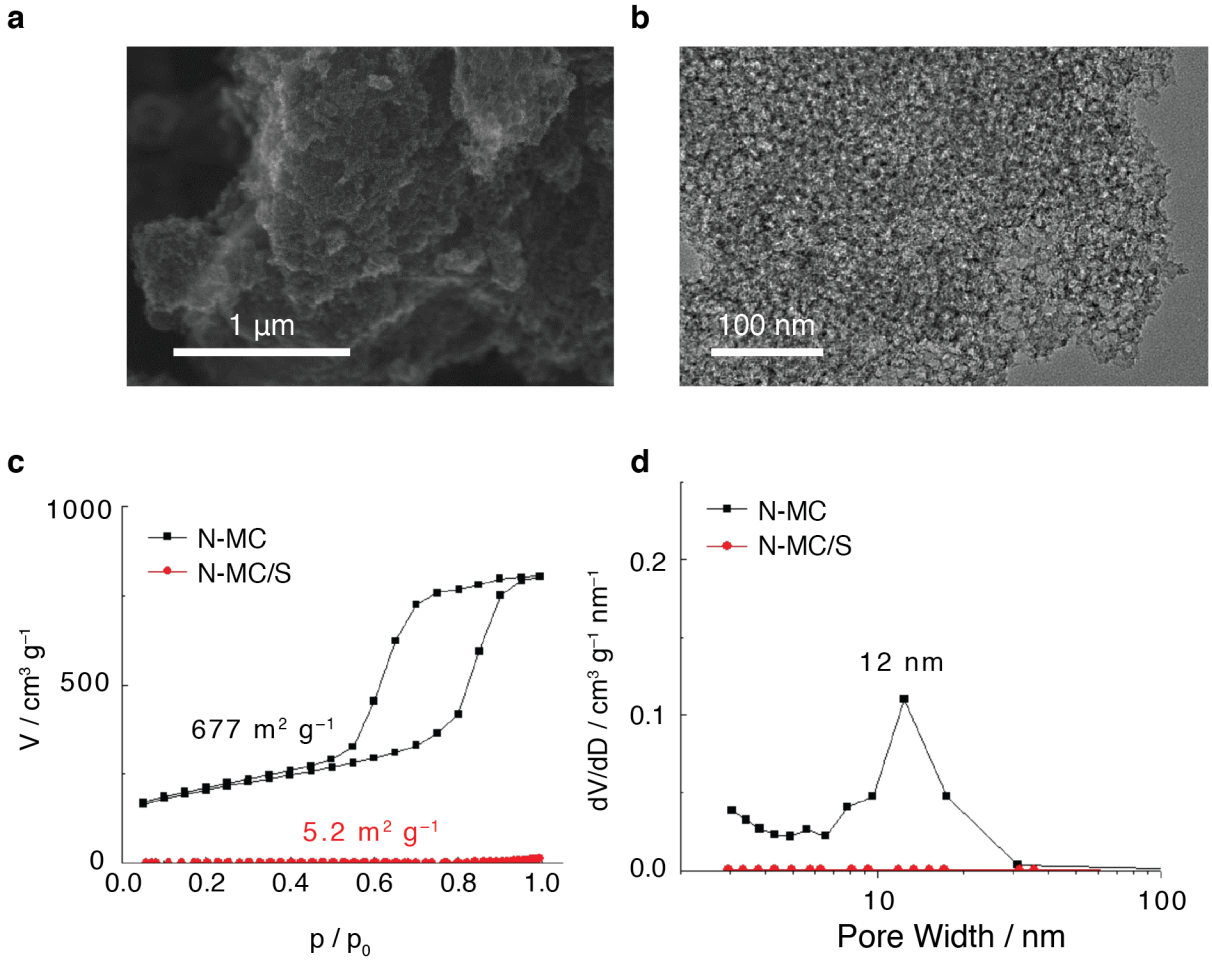

Figure 5.8 Characterization of N-Doped Mesoporous Carbon (N-MC) and N-MC/S. a) SEM of N-MC. b) TEM of N-MC. c) Nitrogen adsorption isotherms of N-MC and N-MC/S. d) BJH pore size distribution of N-MC and N-MC/S.

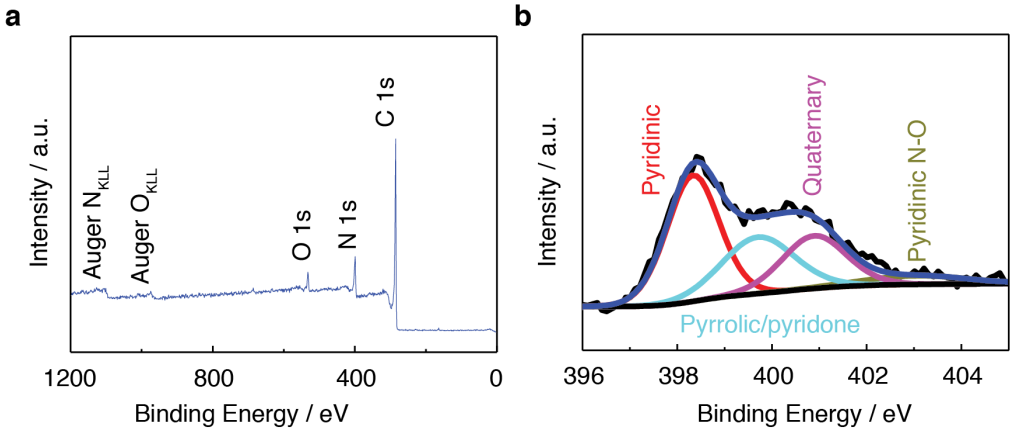

Figure 5.9 XPS analysis of N-MC hosts for sulfur active materials. a) Survey scan noting the presence of N, C, and O elements in the material. b) Analysis of the N 1s signal, noting the presence of un-oxidized and oxidized sp^2 motifs, and quaternized sp^3 motifs.

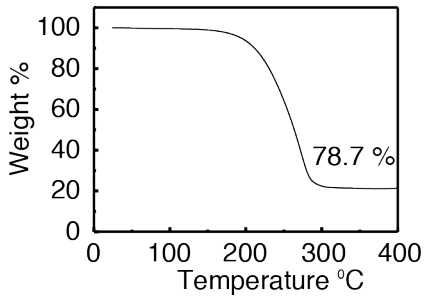

Figure 5.10 TGA analysis of N-MC/S composite.

PEB-1 synthesis

PEB-1 was synthesized by anion metathesis. Briefly, PDDA-Cl (20.0 g, 20% *w*/*w* in H_2O, 10.0 µmol) was diluted with DI water (100 mL) prior to the addition of LiTFSI (8.52 g, 29.7 mmol) in DI water (10 mL). PEB-1 was collected as a colorless solid after vacuum filtration and drying in vacuo. Analytical characterization—i.e., ^{1}H NMR, FTIR, TGA, EA: Anal. Calc'd: C, 29.56; H, 3.97; N, 6.89; O, 15.78; Found: C, 29.43; H, 3.87; N, 6.89; O, 16.15, etc.—was in agreement with a previous synthesis.[34]

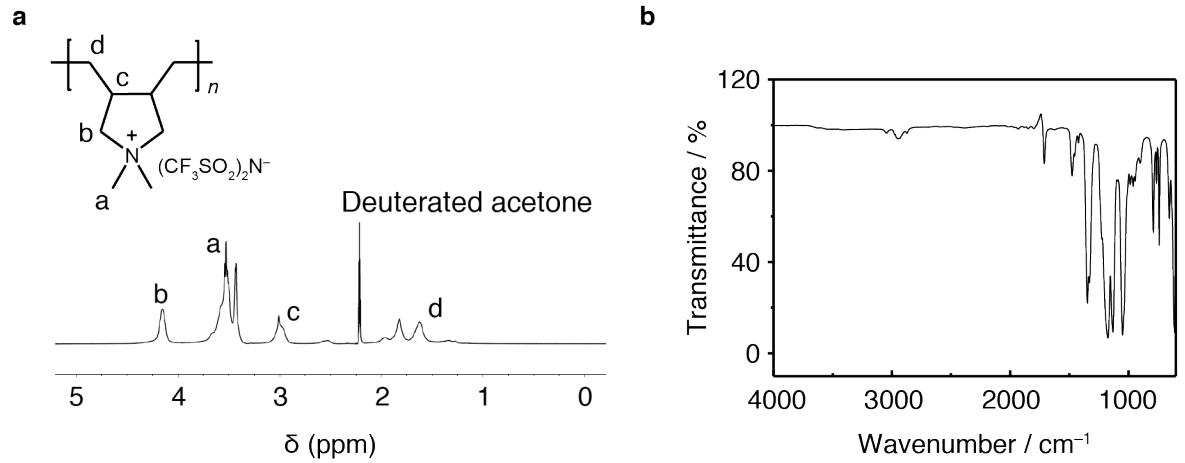

Figure 5.11 a) ^{1}H NMR and b) FTIR of PEB-1.

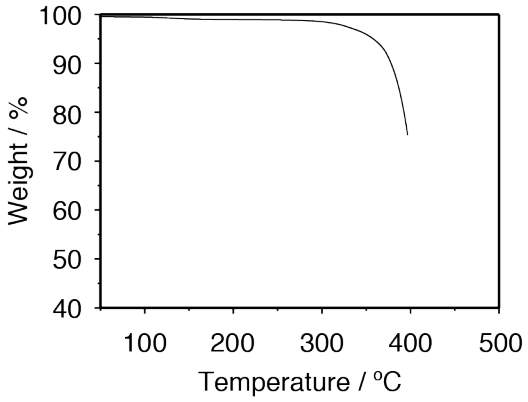

Figure 5.12 TGA of PEB-1.

Fabrication of sulfur cathodes

A thin slurry was formed by mixing N-MC/S composite, binder (PEB-1 or PVDF), and Super P in NMP in a weight ratio of 7:1:2 and stirred overnight. The well-dispersed slurry was then coated onto an aluminum foil substrate by using a doctor blade. The coated electrodes were dried overnight at 50 °C under vacuum before being cut into circular disks with a diameter of 1.2 cm. The mass loading of sulfur in the sulfur electrodes was around 1.2 mg cm^{-2}. Alternatively, a CNF current collector was prepared by a vacuum-filtration process as reported previously.[6] The CNF current collector was cut into circular disks with a diameter of 1.2 cm with mass ~ 2 mg. N-MC/S and PEB-1 mixture slurry (weight ratio 9:1) was then drop cast on the CNF current collector and dried overnight at 50 °C under vacuum. Each CNF current collector contained a sulfur mass loading of 4–5 mg cm^{-2}.

5.7.3 Characterization

SEM was carried out using a Zeiss Gemini Ultra-55 analytical Field Emission Scanning Electron Microscope. TEM was carried out using a JEOL 2100 F at an acceleration voltage of 200 kV. UV-visible-spectra were collected with a Cary 5000 UV-Vis-NIR spectrophotometer. XPS measurements were performed using a Specs PHOIBOS 150 hemispherical energy analyzer using a monochromated Al Kα X-ray source. The load-lock of the analytical UHV system is connected directly to an Ar-filled glove box, enabling the loading of samples without any exposure to ambient atmosphere. Powder samples were mounted on carbon tape supported by Si substrates. Charge neutralization was carried out using a low energy flood gun (electron energy ≤ 5 eV), with the neutralization conditions optimized based on the degree of charging present for a given sample. Survey spectra were measured using a pass energy of 40 eV at a resolution of 0.2 eV/step and a total integration time of 0.2 s/point. Core level spectra were measured using a pass energy of 20 eV at a resolution of 0.05 eV/step and a total integration time of 0.5 s/point. Deconvolution was performed using CasaXPS software with a Shirley-type background and 70–30 Gaussian-Lorentzian peak shapes. Spectra were charge referenced using the position of aliphatic carbon in the C 1 s peak at 284.8 eV. Li–S batteries were tested with CR2032-type coin cells. The sulfur cathode and lithium metal anode were separated by a single Celgard 2400 separator. The electrolyte was made of 1.0 M LiTFSI and 0.2 M $LiNO_3$ dissolved in DOL/DME (1:1 *v*/*v*). The electrolyte:sulfur ratio (E:S) was ~ 10 $ml_E\ g_S^{-1}$. Electrochemical experiments were carried out using a Biologic VMP3 potentiostat. The galvanostatic cycling tests at different C rates (1 C = 1675 mA h g^{-1}) were conducted within the voltage range of 1.8–

2.8 V. Impedance data were recorded at open circuit voltage (OCV) in the frequency range of 1 MHz to 1 Hz with an AC voltage amplitude of 10 mV. CV measurements were conducted between 1.8–2.8 V at a scan rate of 0.1 mV s^{-1}. For potentiostatic electrodeposition, cells were equilibrated at 2.3 V to transform sulfur into long-chain polysulfides before driving the Li_2S electrodeposition at constant voltage: either 2.0 V or 1.9 V.

5.8 Acknowledgements

I would like to thank all of the co-authors who made this work possible, including Longjun Li, Tod Pascal, Justin Connell, Frank Fan, Lin Ma, Yet-Ming Chiang, David Prendergast, and Brett Helms. This work was supported by the Joint Center for Energy Storage Research, an Energy Innovation Hub funded by the US Department of Energy, Office of Science, Office of Basic Energy Sciences. Portions of the work—including PEB-1 and N-MC synthesis, characterization, and some testing in Li–S cells—were carried out as a user project at the Molecular Foundry, which is supported by the Office of Science, Office of Basic Energy Sciences, of the US Department of Energy under contract no. DE-AC02-05CH11231. This research used resources of the National Energy Research Scientific Computing Center and the Advanced Light Source, DOE Office of Science User Facilities supported by the Office of Science of the US Department of Energy under that same contract. XPS measurements were completed at the Electrochemical Discovery Laboratory at Argonne National Laboratory. Teresa Williams is thanked for assistance with TEM.

5.9 References

1. a) Z. W. Seh, Q. Zhang, W. Li, G. Zheng, H. Yao, Y. Cui, *Chem. Sci.* **2013**, *4*, 3673; b) M. He, L.-X. Yuan, W.-X. Zhang, X.-L. Hu, Y.-H. Huang, *J. Phys. Chem. C* **2011**, *115*, 15703; c) M. J. Lacey, F. Jeschull, K. Edström, D. Brandell, *J. Phys. Chem. C* **2014**, *118*, 25890; d) C. Milroy, A. Manthiram, *Adv. Mater.* **2016**, *28*, 9744.
2. a) P. D. Frischmann, Y. Hwa, E. J. Cairns, B. A. Helms, *Chem. Mater.* **2016**, *28*, 7414; b) S. N. Patel, A. E. Javier, G. M. Stone, S. A. Mullin, N. P. Balsara, *ACS Nano* **2012**, *6*, 1589; c) G. Ai, Y. Dai, Y. Ye, W. Mao, Z. Wang, H. Zhao, Y. Chen, J. Zhu, Y. Fu, V. Battaglia, J. Guo, V. Srinivasan, G. Liu, *Nano Energy* **2015**, *16*, 28.
3. a) S. N. Talapaneni, T. H. Hwang, S. H. Je, O. Buyukcakir, J. W. Choi, A. Coskun, A. Coskun, *Angew. Chem. Int. Ed.* **2016**, *55*, 3106; b) S. H. Je, T. H. Hwang, S. N. Talapaneni, O. Buyukcakir, H. J. Kim, J.-S. Yu, S.-G. Woo, M. C. Jang, B. K. Son, A. Coskun, J. W. Choi, *ACS Energy Lett.* **2016**, *1*, 566; c) W. J. Chung, J. J. Griebel, E. T. Kim, H. Yoon, A. G. Simmonds, H. J. Ji, P. T. Dirlam, R. S. Glass, J. J. Wie, N. A. Nguyen, B. W. Guralnick, J. Park, A. Somogyi, P. Theato, M. E. Mackay, Y.-E. Sung, K. Char, J. Pyun, *Nat. Chem.* **2013**, *5*, 518; d) H. Kim, J. Lee, H. Ahn, O. Kim, M. J. Park, *Nat. Commun.* **2015**, *6*, 7278.
4. a) X. Ji, K. T. Lee, L. F. Nazar, *Nat. Mater.* **2009**, *8*, 500; b) J. Song, T. Xu, M. L. Gordin, P. Zhu, D. Lv, Y. B. Jiang, Y. Chen, Y. Duan, D. Wang, *Adv. Funct. Mater.* **2014**, *24*, 1243; c) Q. Pang, L. F. Nazar, *ACS Nano* **2016**, *10*, 4111; d) L. Ma, H. L. Zhuang, S. Wei, K. E. Hendrickson, M. S. Kim, G. Cohn, R. G. Hennig, L. A. Archer, *ACS Nano* **2016**, *10*, 1050.
5. a) G. Zhou, S. Pei, L. Li, D.-W. Wang, S. Wang, K. Huang, L.-C. Yin, F. Li, H.-M. Cheng, *Adv. Mater.* **2014**, *26*, 625; b) Y. Fu, Y.-S. Su, A. Manthiram, *Angew. Chem. Int.*

Ed. **2013**, *52*, 6930; c) W. Zhou, B. Guo, H. Gao, J. B. Goodenough, *Adv. Energy Mater.* **2016**, *6*, 1502059.
6. C. Zu, Y. Fu, A. Manthiram, *J. Mat. Chem. A* **2013**, *1*, 10362.
7. a) C. Li, A. L. Ward, S. E. Doris, B. A. Helms, C. Li, A. L. Ward, S. E. Doris, T. A. Pascal, D. Prendergast, B. A. Helms, C. Li, S. E. Doris, *Nano Lett.* **2015**, *15*, 5724; b) S. Bai, X. Liu, K. Zhu, S. Wu, H. Zhou, *Nature Energy* **2016**, *1*, 16094.
8. a) L. C. H. Gerber, P. D. Frischmann, F. Y. Fan, S. E. Doris, X. Qu, A. M. Scheuermann, K. Persson, Y.-M. Chiang, B. A. Helms, *Nano Lett.* **2016**, *16*, 549; b) H.-J. Peng, G. Zhang, X. Chen, Z.-W. Zhang, W.-T. Xu, J.-Q. Huang, Q. Zhang, *Angew. Chem. Int. Ed.* **2016**, *55*, 12990.
9. F. Wu, J. T. Lee, N. Nitta, H. Kim, O. Borodin, G. Yushin, *Adv. Mater.* **2015**, *27*, 101.
10. a) S. Zhang, K. Ueno, K. Dokko, M. Watanabe, *Adv. Energy Mater.* **2015**, *5*, 1500117; b) M. Cuisinier, P. E. Cabelguen, B. D. Adams, A. Garsuch, M. Balasubramanian, L. F. Nazar, *Energy Environ. Sci.* **2014**, *7*, 2697; c) L. Cheng, L. A. Curtiss, K. R. Zavadil, A. A. Gewirth, Y. Shao, K. G. Gallagher, *ACS Energy Lett.* **2016**, *1*, 503; d) L. Suo, Y.-S. Hu, H. Li, M. Armand, L. Chen, *Nat. Commun.* **2013**, *4*, 1481; e) L. Wang, Y. Wang, Y. Xia, *Energy Environ. Sci.* **2015**, *8*, 1551; f) Kolosnitsyn, V. & Karaseva, E., inventors; Oxis Energy Limited, assignee. Electrolyte compositions for batteries using sulphur or sulphur compounds. Patent US 9196929 B2, 2015.
11. a) W. Li, H. Yao, K. Yan, Z. Liang, G. Zheng, Y.-M. Chiang, Y. Cui, *Nat. Commun.* **2015**, *6*, 7436; b) Y. Lu, Z. Tu, L. A. Archer, *Nat. Mater.* **2014**, *13*, 961; c) Z. Lin, Z. Liu, W. Fu, J. Dudney Nancy, C. Liang, *Adv. Funct. Mater.* **2012**, *23*, 1064; d) J. Zheng, M. Gu, H. Chen, P. Meduri, M. H. Engelhard, J.-G. Zhang, J. Liu, J. Xiao, *J. Mater. Chem. A* **2013**, *1*, 8464.
12. a) D. Eroglu, K. R. Zavadil, K. G. Gallagher, *J. Electrochem. Soc.* **2015**, *162*, A982; b) B. D. McCloskey, *J. Phys. Chem. Lett.* **2015**, *6*, 4581.
13. a) A. Manthiram, Y. Fu, S.-H. Chung, C. Zu, Y.-S. Su, *Chem. Rev.* **2014**, *114*, 11751; b) Q. Pang, X. Liang, C. Y. Kwok, L. F. Nazar, *Nat. Energy* **2016**, *1*, 16132; c) L. Ma, K. E. Hendrickson, S. Wei, L. A. Archer, *Nano Today* **2015**, *10*, 315.
14. a) E. G. Gebresilassie, M. Armand, B. Scrosati, S. Passerini, *Angew. Chem. Int. Ed.* **2014**, *53*, 13342; b) I. Osada, V. H. de, B. Scrosati, S. Passerini, *Angew. Chem. Int. Ed.* **2016**, *55*, 500; c) J. Yuan, D. Mecerreyes, M. Antonietti, *Prog. Polym. Sci.* **2013**, *38*, 1009.
15. L. Li, T. A. Pascal, J. G. Connell, F. Y. Fan, S. M. Meckler, L. Ma, Y.-M. Chiang, D. Prendergast, B. A. Helms, *Nat. Commun.* **2017**, *8*, 2277.
16. B. M. L. Rao, J. A. Shropshire, *J. Electrochem. Soc.* **1981**, *128*, 942.
17. M. U. M. Patel, R. Demir-Cakan, M. Morcrette, J.-M. Tarascon, M. Gaberscek, R. Dominko, *ChemSusChem* **2013**, *6*, 1177.
18. T. A. Pascal, D. Prendergast, K. H. Wujcik, D. R. Wang, N. P. Balsara, *Phys. Chem. Chem. Phys.* **2017**, *19*, 1441.
19. H.-H. Perkampus, H.-C. Grinter. UV-Vis Spectroscopy and Its Applications, Springer, 1992.
20. a) L. Alessandro, L. G. Francesco, *Rep. Prog. Phys.* **2008**, *71*, 126601; b) A. K. Rappe, W. A. Goddard, *J. Phys. Chem.* **1991**, *95*, 3358.
21. a) J. Chen, T. J. Martínez, *Chem. Phys. Lett.* **2007**, *438*, 315; b) T. A. Pascal, K. H. Wujcik, J. Velasco-Velez, C. Wu, A. A. Teran, M. Kapilashrami, J. Guo, M. Salmeron, N. Balsara, D. Prendergast, J. Cabana, *J. Phys. Chem. Lett.* **2014**, *5*, 1547.

22. M. A. Marcus, A. A. MacDowell, R. Celestre, A. Manceau, T. Miller, H. A. Padmore, R. E. Sublett, *J. Synchrotron Radiat.* **2004**, *11*, 239.
23. a) K. H. Wujcik, T. A. Pascal, C. D. Pemmaraju, D. Devaux, W. C. Stolte, N. P. Balsara, D. Prendergast, *Adv. Energy Mater.* **2015**, *5*, 1500285; b) K. H. Wujcik, J. Velasco-Velez, C. H. Wu, T. Pascal, A. A. Teran, M. A. Marcus, J. Cabana, J. Guo, D. Prendergast, M. Salmeron, N. P. Balsara, *J. Electrochem. Soc.* **2014**, *161*, A1100.
24. M. Cuisinier, P.-E. Cabelguen, S. Evers, G. He, M. Kolbeck, A. Garsuch, T. Bolin, M. Balasubramanian, L. F. Nazar, *J. Phys. Chem. Lett.* **2013**, *4*, 3227.
25. T. A. Pascal, C. D. Pemmaraju, D. Prendergast, *Phys. Chem. Chem. Phys.* **2015**, *17*, 7743.
26. X. Tao, J. Wang, Z. Ying, Q. Cai, G. Zheng, Y. Gan, H. Huang, Y. Xia, C. Liang, W. Zhang, Y. Cui, *Nano Lett.* **2014**, *14*, 5288.
27. Q. Pang, D. Kundu, M. Cuisinier, L. F. Nazar, *Nat. Commun.* **2014**, *5*, 4759.
28. a) X. Wang, G. Li, J. Li, Y. Zhang, A. Wook, A. Yu, Z. Chen, *Energy Environ. Sci.* **2016**, *9*, 2533; b) P. T. Dirlam, A. G. Simmonds, C. B. Arrington, T. S. Kleine, R. S. Glass, J. Pyun, J. Park, K. Char, Y.-E. Sung, J. Pyun, K. Domanik, J. L. Schaefer, V. P. Oleshko, C. L. Soles, J. L. Schaefer, C. Kim, N. Pinna, *ACS Appl. Mater. Interfaces* **2016**, *8*, 13437.
29. S. S. Zhang, *J. Electrochem. Soc.* **2012**, *159*, A1226.
30. M. J. Lacey, F. Jeschull, K. Edstrom, D. Brandell, *Chem. Commun.* **2013**, *49*, 8531.
31. S.-E. Cheon, J.-H. Cho, K.-S. Ko, C.-W. Kwon, D.-R. Chang, H.-T. Kim, S.-W. Kim, *J. Electrochem. Soc.* **2002**, *149*, A1437.
32. Y. Meng, D. Gu, F. Zhang, Y. Shi, L. Cheng, D. Feng, Z. Wu, Z. Chen, Y. Wan, A. Stein, D. Zhao, *Chem. Mater.* **2006**, *18*, 4447.
33. L. Li, C. Liu, G. He, D. Fan, A. Manthiram, *Energy Environ. Sci.* **2015**, *8*, 3274.
34. A.-L. Pont, R. Marcilla, I. De Meatza, H. Grande, D. Mecerreyes, *J. Power Sources* **2009**, *188*, 558.

Chapter 6

Conclusion

Here I have outlined my work rationally designing microporous membrane materials to control selective mass transport. Micropore networks exist at a crucial length scale for the transport of small species such as gases. As these permeating species traverse the membrane, they must pass size-limiting apertures to diffuse between pores, often requiring fluctuations in the free-space distribution of the membrane material. Further control over mass transport can be realized by introducing chemically selective sites along the pore network, which can facilitate transport or irreversibly bind certain species. The nature of the membrane materials, which can be random, as is the case for microporous polymers, or periodic, as is seen in MOFs, must be considered in stride with the separation in question.

In this dissertation, I demonstrated methods to improve permselectivity in polymeric membranes of varying materials and architectural complexity. First, I discussed how increasing polymer backbone rigidity enhances permselectivity in single-component thermally rearranged polymer membranes. Next, I introduced a highly selective phase-change chemisorptive MOF filler, mmen-Mg_2(dobpdc), into a MMM to realize cooperative facilitated transport of CO_2. Then I showed how MOF-polymer composites can be extended to more sophisticated formats through the growth of ZIF-8 thin films on a porous polymer surface. Finally, I investigated how polymer binders with cationic backbones impede anionic polysulfide diffusion, preventing unwanted mass transport that would detrimentally relocate active material away from the sulfur cathode. The perspective that emerges from these studies is that innovative materials synthesis and processing are critical in advancing the field of membrane separations.

These studies serve as important guideposts for the future development of polymeric membranes. Backbone chemistry will always be a defining factor in a polymer or composite membrane. For gas separations, the Tröger's base TR polymers I presented demonstrate the importance the rigidity in the contortion site. Future work in this direction should focus on computational screens of candidate backbone architectures to understand how local rigidity leads to longer-length-scale pore-wall flexibility. Orthogonally, increased steric bulk along polymer chains can also enhance permeability. Macromolecular design focused on these principles is key to further polymer permselectivity.

Chemisorption is a powerful and largely underutilized tool in membrane design, especially in the case of gas separations. While physisorptive mechanisms are more common, systems that selectively, covalently, and reversibly bond a gaseous species, as seen with mmen-Mg_2(dobpdc), are more difficult to achieve. As seen in the case of PEB-1 interactions with polysulfides, the binding can be strong enough to stall transport or saturate the binding sites on time scales approaching irreversibility at relevant temperatures. Therefore, methods to tune the gas/binding site interaction are key, and here the diamine appended M_2(dobpdc) family shows great promise. Judicious choice of metal center and diamine, both synthetically accessible modifications from the mmen-Mg_2(dobpdc) system studied, change how carbamate chains form and release CO_2 along the MOF channels. In future generations of this technology, new phase-change adsorptive MOFs can also be investigated; here, rigorous analytical and MD models of transport in these systems will be needed to inform productive materials selection. As seen in PEB-1, chemical reactivity can also be directly incorporated into the organic backbone of the polymer. As design strategies to maximize diffusive selectivity and permeability through backbone rigidity and contortions mature, a focus on solubility selectivity enhancement will be one of the strongest tools available to challenge the Robeson upper bound relationships.

In the case of layered MOF-polymer films, the separation performance of each phase is decoupled, allowing for the permeability of the thick polymer support and the selectivity of the

MOF coating to be separately tuned. In my system, adhesion between the polymer and ZnO NCs or MOF was robust, but the intricacies of the interfacial interactions warrants further study. Specifically, the kinetics of gas transport across such junctions is important in the case of layered membranes and MMMs alike but is difficult to probe, as it requires metrologies sensitive to buried interfaces. The development of such techniques will be needed to design interfaces for enhanced performance.